

学位論文（要約）

Structural insights into the ligand recognition and functional
regulation of the ATP-gated P2X receptor channels

（ATP 作動性チャネル P2X 受容体における基質認識
および機能調節の構造基盤）

平成 29 年 12 月 博士（理学）申請

東京大学大学院理学系研究科

生物科学専攻

糟谷 豪

Abstract

Adenosine triphosphate (ATP), an important intracellular energy source, is also an extracellular neurotransmitter that controls cell functions via cell surface receptors. P2X receptors are trimeric cation-selective, ligand-gated ion channels that permeate a wide range of monovalent and divalent cations, by responding to extracellular ATP. Each subunit of the P2X receptors is composed of the large extracellular domain that contains the ATP and regulatory metal binding sites, the two transmembrane helices that form a non-selective cation pore, and the intracellular N- and C-termini that modulate channel gating. In vertebrates, seven subtypes of P2X receptors, named P2X1 to P2X7, are widely expressed in excitable and non-excitable cells, and are involved in diverse physiological processes, such as muscle contraction, neurotransmission, inflammatory response, pain and taste signal transduction. Accordingly, P2X receptors are associated with numerous human diseases, including chronic inflammatory pain, depression, and cancer, and have attracted great interest as potential drug targets for these diseases. The previously determined structures of the zebrafish P2X4 receptor in the apo, closed and the ATP-bound open states, reported in 2009 and 2012, and the human P2X3 receptor, reported in 2016, revealed the overall architecture of the P2X receptor family and provided structural insights into the molecular mechanisms of ATP-dependent gating cycle, as well as the recognition of agonists and antagonists in the P2X receptor family. Quite recently, the crystal structures of the panda P2X7 receptor, reported in late 2016, provided structural insights clarifying the actions of the subtype-specific non-competitive antagonists of P2X7 receptors. However, there remains a lot of questions about the molecular mechanisms of P2X receptors functions, such as ligand selectivity, gating modulation and competitive inhibition. In this thesis, by using X-ray crystallographic and other biological techniques, the following questions of P2X receptor functions are addressed.

1. Nucleotide selectivity of P2X receptors

Among nucleotide triphosphates, while P2X receptors have high affinity for ATP as an endogenous agonist, P2X receptors have weak affinity for CTP (20 to 50 of times lower affinity than for ATP) but lack affinities for GTP and UTP. This nucleotide base selectivity is important for proper function of P2X receptors but the mechanism remains elusive, due to the lack of structural information for the P2X receptor in complex with other nucleoside triphosphates, particularly the low-affinity pyrimidine agonist, CTP. In this study, the crystal structure of zebrafish P2X4 in complex with CTP was determined, and structure-based electrophysiological and spectroscopic analyses were conducted. The CTP-bound structure had a hydrogen bond, between the cytosine base and the side chain of the basic residue in the agonist binding site, which mediates the weak but significant affinity for CTP. The cytosine base is further recognized by two main chain atoms, as in the ATP-bound structure, but their bond lengths seem to be extended in the CTP-bound structure, also possibly contributing to the weaker affinity for CTP over ATP. This work provides the structural insights for the nucleotide base specificity of P2X receptors.

2. Divalent cation modulations of P2X receptors

The activation of ligand-gated ion channels, including P2X receptors, Cys-loop receptors, and ionotropic glutamate receptors, is modulated by various molecules to diversify their physiological functions. In particular, divalent cations are important regulatory factors in these ion channel superfamilies. For instance, in some P2X receptors, a Zn^{2+} ion potentiates the ATP-dependent currents, which leads to insulin secretion. However, the molecular mechanisms of the divalent cation modulation of the P2X receptors, underlying the diversity of the receptor functions, have still proved elusive. In this study, the crystal structure of an invertebrate P2X receptor from the Gulf Coast tick, *Amblyomma maculatum*, was determined in the presence of ATP and Zn^{2+} ion, and structure-based electrophysiological and computational analyses were conducted. The structure revealed two distinct metal binding sites, M1 and M2, in the extracellular region. The M1 site, located at the trimer

interface, is responsible for Zn^{2+} potentiation by facilitating the structural change of the extracellular domain for pore opening. In contrast, the M2 site, coupled with the ATP binding site, might contribute to regulation by Mg^{2+} . This work provides structural insights into the divalent cation modulations of P2X receptors.

3. Competitive inhibition of P2X receptors

Since the chronic activation of P2X receptors are associated with numerous human diseases including inflammatory and neuropathic pains, the chemical compounds inhibiting P2X receptors have attracted great interest as potential drug targets for those diseases. Therefore, the determination of P2X structures in complex with various antagonists will facilitate for drug discovery targeting P2X receptors. Intriguingly, the recent crystallographic and NMR analyses of P2X receptors revealed an unexpected discrepancy regarding the antagonistic mechanism by 2',3'-O-(2,4,6-trinitrophenyl)-ATP (TNP-ATP), one of the subtype non-selective competitive P2X antagonists. The crystal structure of the human P2X3 receptor in complex with TNP-ATP adopted the same conformation as that in the apo, closed state. In contrast, the NMR analysis of the zebrafish P2X4 receptor showed that TNP-ATP binding induces the expansion of the extracellular domain, in a similar manner to that observed with ATP-dependent activation. In this study, the crystal structure of the chicken P2X7 receptor was determined in complex with the TNP-ATP, and structure-based computational analysis was conducted. The structure reveals an expanded, incompletely activated conformation of the channel, and identified the unique recognition manner of TNP-ATP, which is distinct from that observed in the previously determined human P2X3 receptor structure. This work furnishes mechanistic insights into the TNP-ATP-dependent inhibition.

Contents

Abstract	3
Contents	6
Table of abbreviations	9
Table of amino acid abbreviations	10
Chapter 1: General introduction (P2X receptors)	11
1.1 ATP signaling and purinergic receptors	11
1.2 P2X receptors	12
1.3 Structural study of P2X receptors	13
1.4 Overview of this thesis	16
1.4.1 Previously revealed and unrevealed functions of P2X receptors	16
1.4.2 Nucleotide selectivity of P2X receptors (in Chapter 2)	17
1.4.3. Divalent cation modulations of P2X receptors (in Chapter 3)	18
1.4.4. Competitive inhibition mechanism of P2X receptors (in Chapter 4)	19
1.4.5. Thesis composition	20
Chapter 2: Structural insight into the nucleotide selectivity of P2X receptors	22
2.1 Introduction	22
2.1.1 Nucleotide selectivity of P2X receptors	22
2.1.2 Study purpose	23
2.2 Revaling nucleotide selectivity of zebrafish P2X4 (zfP2X4) receptor by electrophysiology	23
2.2.1. Material and methods	24
2.2.1.1 Plasmid construction of zfP2X4 receptor for electrophysiology	24
2.2.1.2 RNA preparation and expression of zfP2X4 receptor	24
2.2.1.3 Electrophysiological recordings of zfP2X4 receptor	25
2.2.2. Results	25
2.2.2.1 Electrophysiological recordings of zfP2X4 receptor	25
2.2.2.2 Nucleotide selectivity of zfP2X4 receptor	25
2.3 Structure determination of the zfP2X4 receptor in the presence of CTP	26
2.3.1 Material and methods	26
2.3.1.1 Plasmid construction of zfP2X4 receptor for structural determination	26
2.3.1.2 Baculovirus preparation of the crystallization construct (Δ P2X4-C)	26
2.3.1.3 Expression and purification of the Δ P2X4-C	27
2.3.1.4 Co-crystallization of the Δ P2X4-C with CTP	28
2.3.1.5 Data collection and structure determination	28
2.3.2. Results	29
2.3.2.1 Overall structure of the CTP-bound zfP2X4	29
2.3.2.2 Cytosine base recognition	31
2.4 Mutation assay of the amino acid residues at the agonist binding site by electrophysiology	34
2.4.1 Material and methods	35
2.4.1.1 Plasmid construction, RNA preparation and expression of rat P2X4 (rP2X4) receptor	35
2.4.1.2 Electrophysiological recordings of rP2X4 receptor	35
2.4.2. Results	35
2.4.2.1 Mutation assay of conserved threonine residue	35
2.4.2.2 Mutation assay of basic residue	37
2.5 Infrared difference spectroscopy upon the ATP and CTP binding	38
2.5.1 Material and methods	38
2.5.1.1 Protein preparation of zfP2X4	38
2.5.1.2 ATR-FTIR measurement	39
2.5.2. Results	39
2.5.2.1 ATP and CTP binding ability of conserved threonine residue	39
2.6 Discussion in this chapter	41
Chapter 3: Structural insight into the divalent cation modulations of P2X receptors	44
3.1 Introduction	44

3.1.1 Gating modulation of P2X receptors	44
3.1.2 Study purpose	44
3.2 Functional characterization of <i>Amblyomma maculatum</i> P2X (AmP2X) receptor.....	44
3.2.1. Material and methods	44
3.2.1.1 Fluorescence-detection size-exclusion chromatography (FSEC).....	44
3.2.1.2 Plasmid construction, RNA preparation and expression of AmP2X receptor.....	46
3.2.1.3 Electrophysiological recordings of AmP2X receptor.....	47
3.2.1.4 Confocal microscopy of AmP2X receptor	47
3.2.1.5 Radiolabeled ATP binding experiments	47
3.2.2. Results.....	48
3.2.2.1 Screening AmP2X receptor as a suitable candidate for structural study	48
3.2.2.2 Electrophysiological recordings of AmP2X receptor.....	48
3.3 Structure determination of the AmP2X receptor in the presence of ATP and Zn^{2+} ion.....	52
3.3.1. Material and methods	52
3.3.1.1 Plasmid construction of AmP2X receptor for structural determination	52
3.3.1.2 Baculovirus preparation of the crystallization construct AmP2X _{cryst}	52
3.3.1.3 Expression and purification of the AmP2X _{cryst}	52
3.3.1.4 Crystallization of the AmP2X _{cryst}	53
3.3.1.5 Data collection and structure determination	53
3.3.2. Results.....	54
3.3.2.1 Overall structure of the AmP2X _{cryst}	54
3.3.2.2 Comparison with the apo, closed and ATP-bound open zfp2X4 receptors	56
3.3.2.3 Zn^{2+} binding site	59
3.4 Mutation assay of the metal binding sites by electrophysiology	60
3.4.1. Material and methods	60
3.4.1.1 Plasmid construction, RNA preparation and expression of rP2X4 receptor	60
3.4.1.2 Electrophysiological recordings of rP2X4 receptor	60
3.4.2. Results.....	60
3.4.2.1 Mutation effects of metal binding site residues on Zn^{2+} ion.....	60
3.4.2.2 Mutation effects of metal binding site residues on Gd^{3+} ion	61
3.5 Zn^{2+} modulation mechanism revealed by molecular dynamics simulations	63
3.5.1. Material and methods	63
3.5.1.1 System construction of molecular dynamics simulation	63
3.5.2. Results.....	64
3.5.2.1 Zn^{2+} effect on the M1 site	64
3.6 Putative Mg^{2+} modulation mechanism gained by electrophysiology	67
3.6.1. Material and methods	68
3.6.1.1 Plasmid construction, RNA preparation and expression of human P2X1 receptor.....	68
3.6.1.2 Electrophysiological recordings of human P2X1 receptor.....	68
3.6.2. Results.....	69
3.6.2.1 Mg^{2+} effect on M1 site.....	69
3.7 Discussion in this chapter	70
Chapter 4: Structural insight into the competitive inhibition of P2X receptors	72
4.1 Introduction.....	72
4.1.1 Inhibitory mechanism of P2X receptors	72
4.1.2 Study purpose	73
4.2 Functional Characterization of chicken P2X7 (ckP2X7) receptor	73
4.2.1. Material and methods	73
4.2.1.1 Fluorescence-detection size-exclusion chromatography (FSEC).....	73
4.2.1.2 Electrophysiological recordings of ckP2X7 receptor	73
4.2.1.3 Fluorescence measurement.....	74
4.2.2. Results.....	75
4.2.2.1 Screening ckP2X7 receptor as a suitable candidate for structural study	75
4.2.2.2 Electrophysiological and biochemical analyses of ckP2X7 receptor	75

4.3 Structure determination of the ckP2X7 receptor in the presence of TNP-ATP	78
4.3.1. Material and methods	78
4.3.1.1 Plasmid construction of ckP2X7 receptor for structural determination	78
4.3.1.2 Baculovirus preparation of the crystallization construct ckP2X7 _{cryst}	78
4.3.1.3 Expression and purification of the ckP2X7 _{cryst}	78
4.3.1.4 Crystallization of the ckP2X7 _{cryst}	79
4.3.1.5 Data collection and structure determination	79
4.3.2. Results.....	80
4.3.2.1 Overall structure of the ckP2X7 _{cryst}	80
4.3.2.2 Comparison with the previously determined P2X receptor structures	82
4.3.2.3 Mapping of functionally important mutations	85
4.3.2.4 TNP-ATP recognition	86
4.3.2.5 Comparison with the apo, closed and ATP-bound open P2X receptor structures.....	90
4.4 Putative antagonistic mechanism revealed by molecular dynamics simulations	91
4.4.1. Material and methods	92
4.4.1.1 System construction of molecular dynamics simulation	92
4.4.2. Results.....	93
4.4.2.1 Putative antagonistic mechanism.....	93
4.5 Discussion in this chapter	94
Chapter 5: General discussion (Overviews and perspectives).....	97
5.1 Overview of this thesis	97
5.1.1 Summary of the thesis	97
5.1.2 Kink motion of transmembrane domain for gating	97
5.1.3 Investigating the kink motion of transmembrane domain in AmP2X	99
5.1.4 TRIC channel structure; an example of kink motion induced by glycine residues	100
5.2 Future perspective.....	101
5.2.1 Structural study of P2X receptor	101
5.2.2 Recent progress in the structure determination using Cryo-EM analysis.....	102
References.....	104
Original papers related to this thesis	116
Supplemental papers related to this thesis	116
Acknowledgement.....	117

Table of abbreviations

Abbreviations	Full name
ADP	adenosine diphosphate
ATP	adenosine triphosphate
AMP	adenosine monophosphate
CBB	coomassie brilliant blue
CTP	cytidine triphosphate
CMV	human cytomegalovirus
DDM	n-dodecyl- β -D-maltopyranoside
EC ₅₀	half maximal (50%) effective concentration
EDTA	(ethylenedinitrilo)tetraacetic acid
EGFP	Enhanced green fluorescent protein
EGTA	(ethyleneglycol)tetraacetic acid
Endo H	Endoglycosidase H
GFP	Green fluorescent protein
GnTI	N-acetylglucosaminyl-transferase I-negative
GPCR	G protein-coupled receptor
GTP	Guanosine triphosphate
HEK293T cell	Human embryonic kidney 293 T cell
HEK293S cell	Human embryonic kidney 293 S cell
HEPES	4-(2-Hydroxyethyl) piperazine-1-ethanesulfonic acid
IPTG	Isopropyl β -D-1-thiogalactopyranoside
K_d	a dissociation constant
LB	Luria-Bertani
MCS	multi cloning site
MES	2-(N-morpholino)ethanesulfonic acid
MD	molecular dynamics
NCBI	National Center for Biotechnology Information
NMR	nuclear magnetic resonance
PDB	Protein Data Bank
PEG	Polyethylene glycol
P1	Purinergic 1 receptor
P2X	Purinergic 2X receptor

P2Y	Purinergic 2Y receptor
POPC	1-palmitoyl-2-oleoyl-phosphatidylcholine
RMSD	root mean square deviation
SDS-PAGE	sodium laurylsulfate-polyacrylamide gel electrophoresis
SEC	size exclusion chromatography
Sf9	<i>Spodoptera frugiperda</i> 9
SNP	single nucleotide polymorphism
TALON	TALON [®] metal affinity resin
TEV	tobacco etch virus
TEVC	Two electrode voltage clamp
TM	transmembrane
TNF- α	Tumor Necrosis Factor- α
TNP-ATP	2',3'-O-(2,4,6-trinitrophenyl)-ATP
Tris	tris(hydroxymethyl)aminomethane
UTP	uridine triphosphate
X-Gal	5-Bromo-4-Chloro-3-Indolyl- β -D-Galactoside

Table of Amino Acid abbreviations

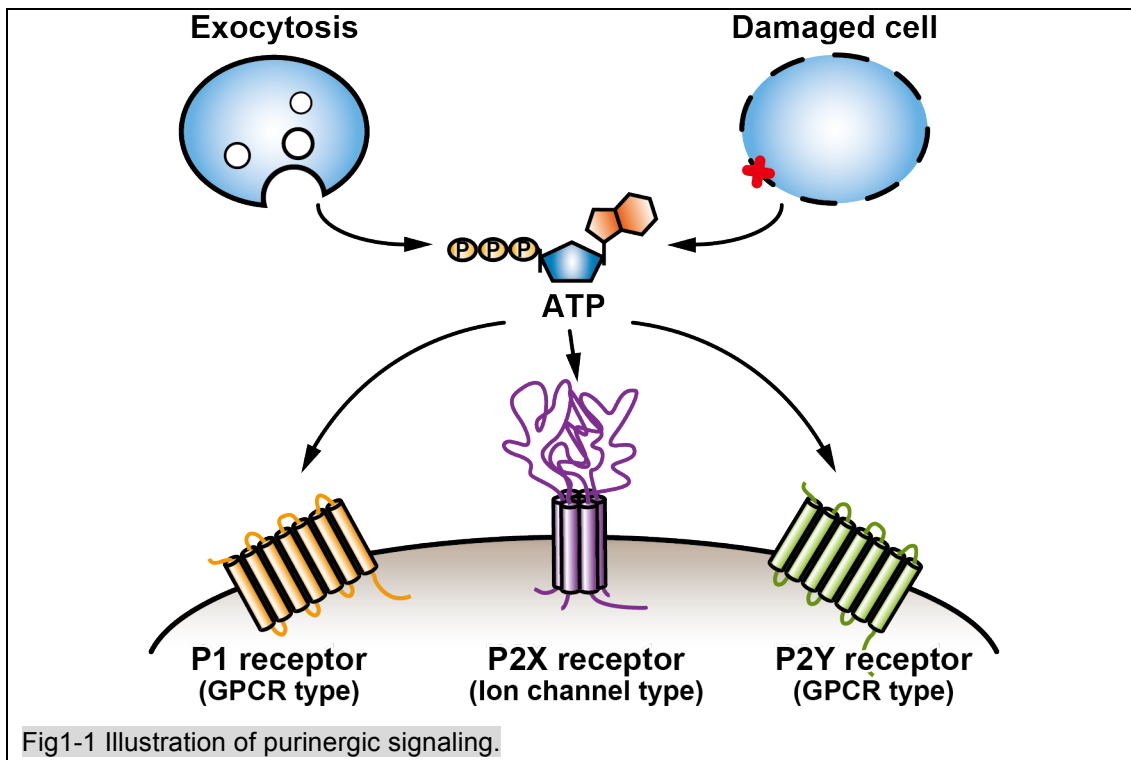
1 letter	3 letter	Full name	1 letter	3 letter	Full name
A	Ala	Alanine	M	Met	Methionine
C	Cys	Cysteine	N	Asn	Asparagine
D	Asp	Aspartic acid	P	Pro	Proline
E	Glu	Glutamic acid	Q	Gln	Glutamine
F	Phe	Phenylalanine	R	Arg	Arginine
G	Gly	Glycine	S	Ser	Serine
H	His	Histidine	T	Thr	Threonine
I	Ile	Isoleucine	V	Val	Valine
K	Lys	Lysine	W	Trp	Tryptophan
L	Leu	leucine	Y	Tyr	Tyrosine

Chapter 1: General introduction (P2X receptors)

1.1 ATP signaling and purinergic receptors

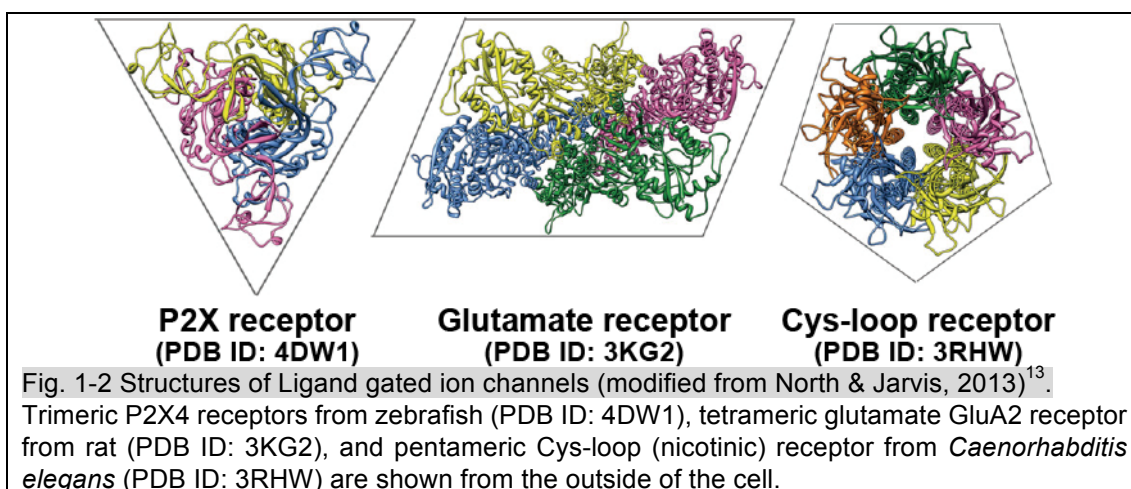
Adenosine triphosphate (ATP) has long been known as an important compound for living organisms since it plays a crucial role as an intracellular energy source by releasing a large amount of energy upon hydrolysis, or as a memory storage component by consisting of DNA and RNA. However, ATP plays another role for an extracellular “neurotransmitter” that controls cell functions via cell surface receptors. This notion that ATP can activate the nerves emerged around the 1970, when some researchers detected that the adenosine efflux occurs by stimulating non-adrenergic inhibitory fibers of the toad or guinea-pig stomach^{1,2}. Subsequent researches confirmed that ATP is indeed a physiologically essential factor in the eukaryotic signal transduction system, and various types of cells have abilities to release and receive ATP. To date, this neurotransmitter pathway using purine and pyrimidine compounds are called “Purinergic signaling” and the receptors detecting the purinergic signaling are called “Purinergic receptors”, which was named by Dr. Geoffrey Burnstock^{3,4}.

After emerging the concept of “Purinergic receptors”, the molecular identification of these receptors was extensively conducted. First, in 1978, based on the affinity for nucleotide-like compounds such as ATP, ADP, AMP, and adenosine⁵, the purinergic receptor family was divided into two classes: P1 receptors and P2 receptors. P1 receptors show higher affinity for adenosine than for other compounds while P2 receptors show higher affinity for ATP than for other compounds. The cloning of these receptor genes in 1990s further proceeded the understanding of P2 receptor entities and classification into two subgroups: P2X receptors⁶⁻⁸ and P2Y receptors⁹. To date, P1 receptor and P2Y receptor families are classified to G-protein coupled receptors (GPCRs) while P2X receptor family is classified to ligand-gated ion channels (**Fig. 1-1**).



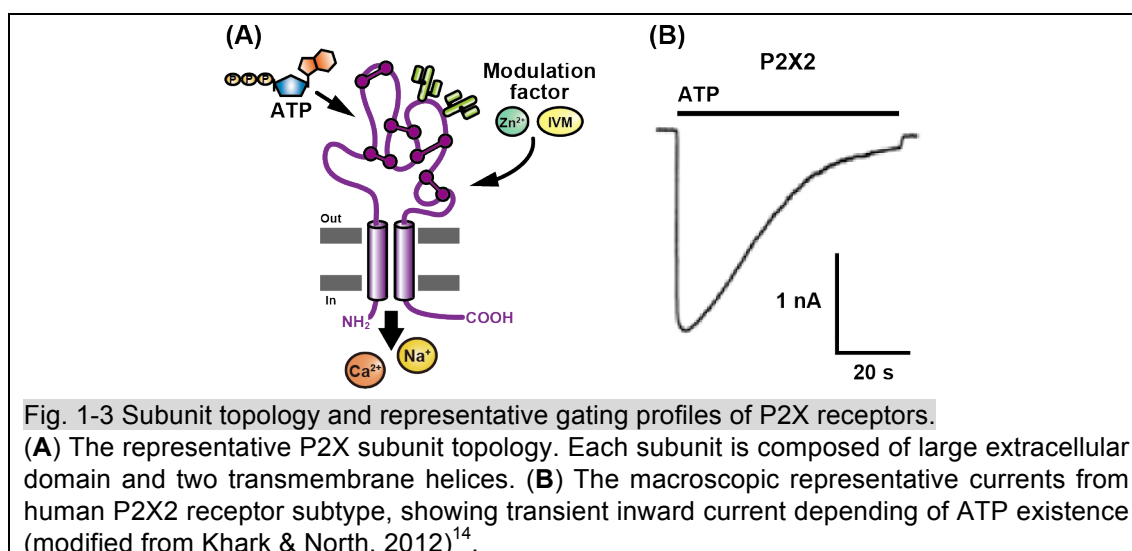
1.2 P2X receptors

P2X receptors belong to ligand-gated ion channel superfamily. Based on the structural topology, this family is composed of three classes of receptors; P2X receptors, Ionotropic glutamate receptors and Cys-loop receptors. The activation of ligand-gated ion channels are controlled by endogenous small ligands including amino acids, metabolites and ions, and are modulated by various molecules such as metal ions and sugars (**Fig. 1-2**)¹⁰⁻¹².

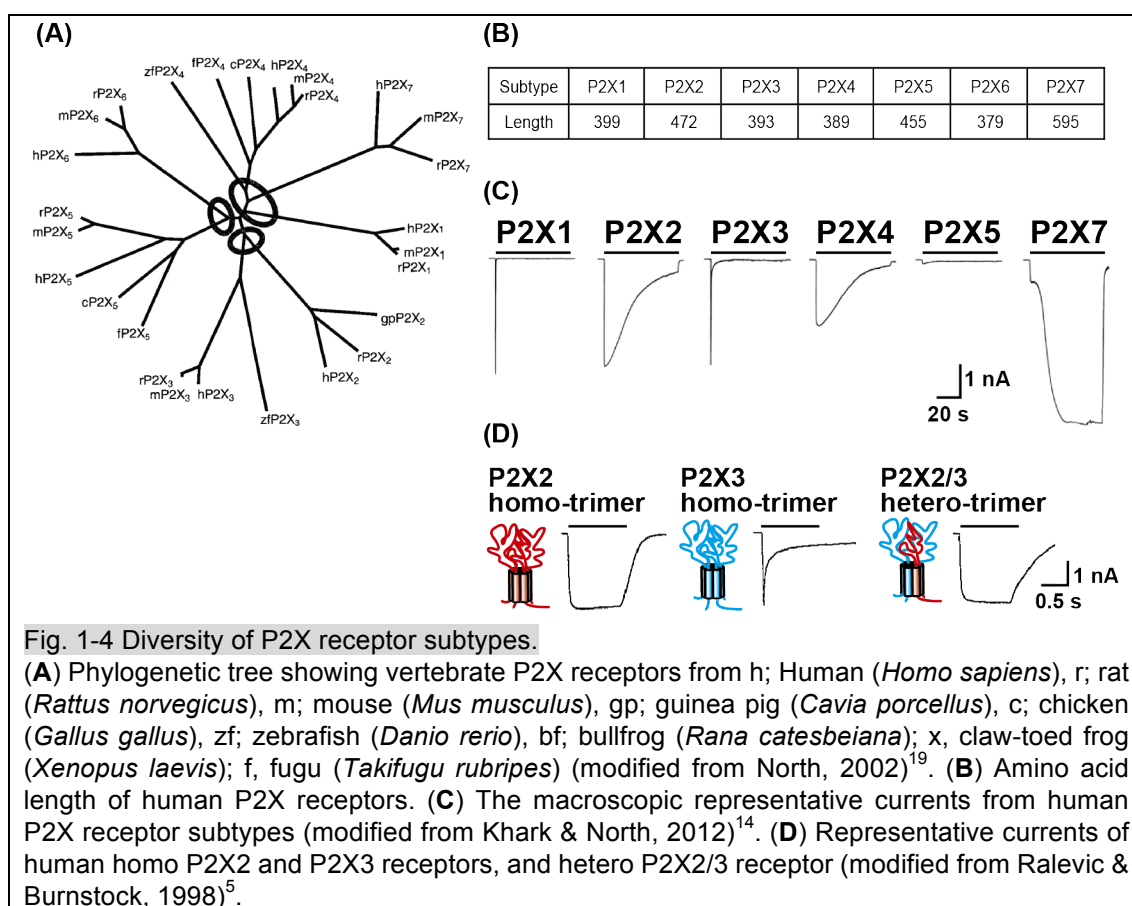


Each subunit of the P2X receptors is composed of the large extracellular domain that contains the

ATP and regulatory metal binding sites, the two transmembrane helices that form a non-selective cation pore, and the intracellular N- and C-termini that modulate channel gating (**Fig. 1-3A**). Gating cycle of P2X receptors are defined four phases: Closed, Open, Desensitization and Deactivation phases. P2X receptors are not activated when ATP is not existed (Closed phase). ATP binding to P2X receptor induces the movement for pore opening, leading to pass transient inward current (Open phase). After activation, the current attenuation is occurred while ATP still remains to bind to P2X receptors (Desensitization phase). Then, ATP removed from receptors with recovering from desensitization phase (Closed phase).



In vertebrates, based on the differences of amino acid sequence, affinities for various ligands, and pattern of current responses, P2X receptors are classified into seven subtypes, named P2X1 to P2X7 (**Fig. 1-4A**). Moreover, some invertebrate species also have P2X receptors similar to their vertebrate counterparts^{14–18}. In humans, the P2X6 has the shortest amino acid sequence (379aa) while the P2X7 has the longest amino acid sequence (595aa) among the family (**Fig. 1-4B**)¹⁰. Most P2X receptor subtypes form homo-trimeric or hetero-trimeric channel pore, except that P2X6 forms only hetero-trimeric channel. The P2X1 and P2X3 receptors are fast-desensitizing while P2X2, P2X4, and P2X7 receptors are slowly-desensitizing (**Fig. 1-4C,D**).

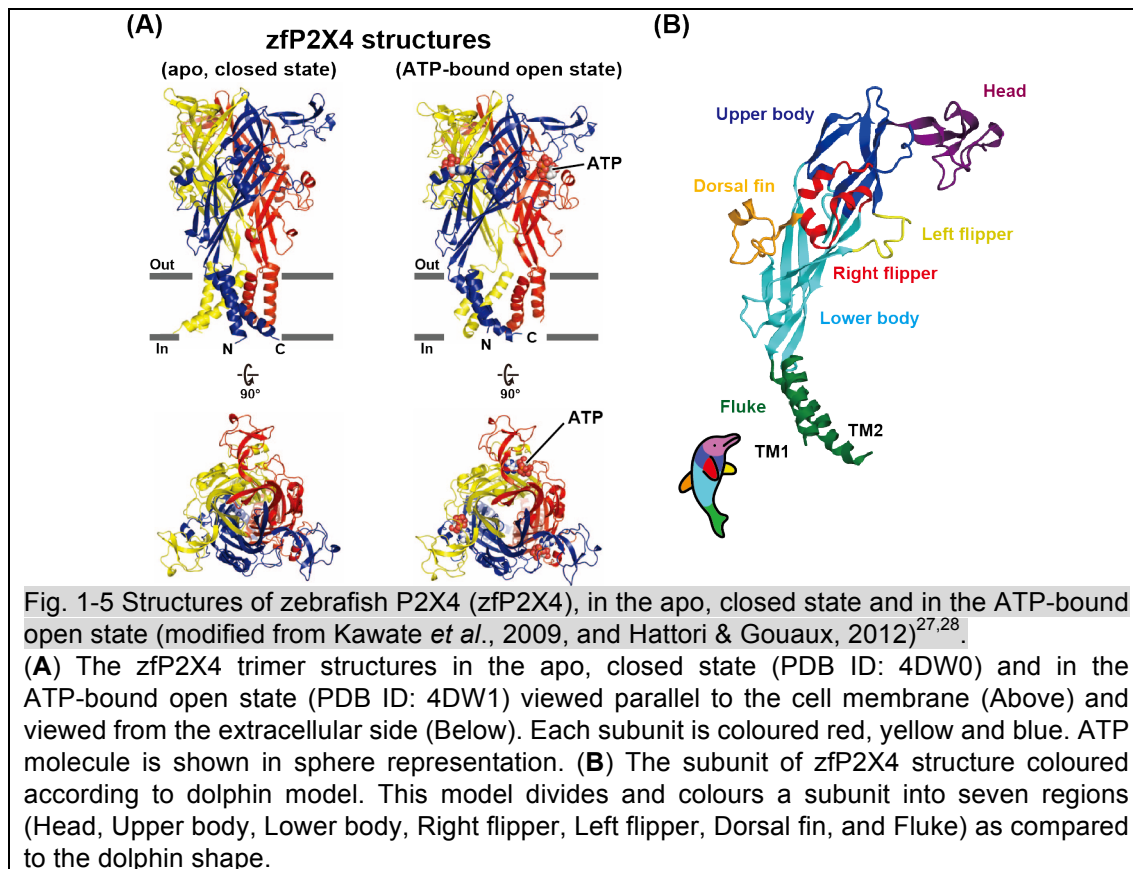


P2X receptors are widely expressed in excitable and non-excitable cells, and are involved in diverse physiological processes, such as muscle contraction, neurotransmission, inflammatory response, pain and taste signal transduction. Accordingly, P2X receptors are associated with numerous human diseases, including chronic inflammatory pain, depression, and cancer^{13,20–22}, and clinical trials of chemical compounds targeting some P2X subtypes have been conducted for P2X receptor-associated diseases^{22,23}.

1.3 Structural study of P2X receptors

P2X receptors are membrane proteins exclusively found in eukaryote. In the views of X-ray crystallographic analysis, compared to water-soluble proteins and prokaryotic membrane proteins, eukaryotic membrane proteins are more difficult to express, purify and crystallize, as they show small expression level, tend to aggregate or dissociate in the presence of detergents commonly used for previous structural studies, and are attached with post-translational modifications such as

glycosylation and prenylation. However, recent progresses of biochemical and biophysical strategies including protein expression and quality evaluation methods have gradually increased the number of reports for eukaryotic membrane protein determinations^{24–26}. Owing to these progresses, in 2009, the first crystal structure of the P2X receptor from zebrafish P2X4 (zfP2X4; the “zf” refers to zebrafish) was determined in the apo, closed state (**Fig. 1-5A, left**)²⁷. Subsequently, in 2012, the crystal structure of zfP2X4 was determined in the ATP-bound open state (**Fig. 1-5A, right**)²⁸. Together with the subsequent structure-based electrophysiological and computational analyses, these results provided the structural framework for trimer formation, ATP recognition, and ATP-dependent activation in the P2X receptor family^{29–33}. The zfP2X4 structures adopts a chalice-like trimeric architecture, and each subunit of zfP2X4 consists of a large extracellular domain and two transmembrane helices resembling the shape of a dolphin, which was deduced from previous biochemical experiments (**Fig. 1-5B**)²⁷.



In addition to the zfP2X4 crystal structures, quite recently, another crystal structures from two P2X receptor subtypes were determined. In 2016, crystal structures of human P2X3 (hP2X3; the “h” refers to human) were proposed in the three different states (the apo, closed, ATP-bound desensitized, and ATP-bound open states) and in the two competitive antagonist bound closed states (A-317491 and TNP-ATP)³⁴. These results provided the molecular mechanisms of ATP-dependent gating cycle, as well as the recognition of agonists and antagonists in the P2X receptor family. Then, in late 2016, the crystal structures of the panda P2X7 (pdP2X7; the “pd” refers to panda) were proposed in the apo, closed state and in the five different non-competitive antagonists bound closed states (JNJ47965567, A740003, A804598, AZ10606120 and GW791343)³⁵. These results provided structural insights clarifying the actions of the subtype-specific non-competitive antagonists of P2X7 receptors (**Fig. 1-6**).

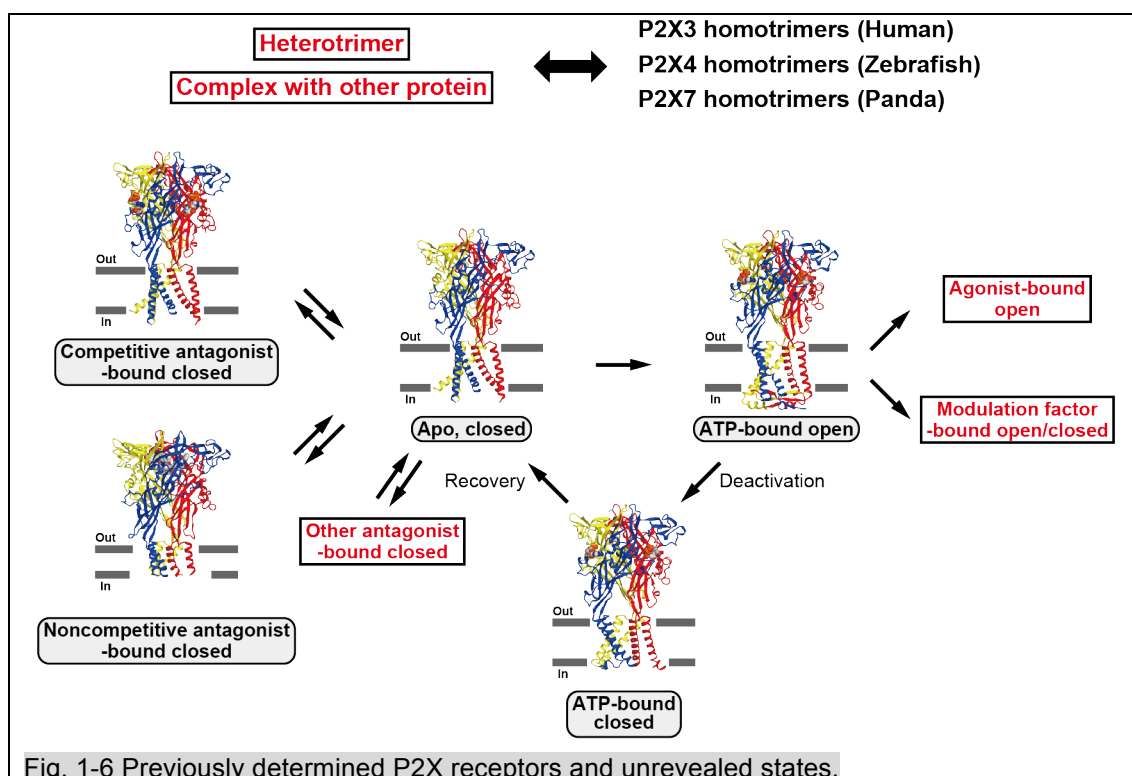


Fig. 1-6 Previously determined P2X receptors and unrevealed states.

1.4 Overview of this thesis

1.4.1 Previously revealed and unrevealed aspects of P2X receptors

The previously determined crystal structures of P2X receptors and subsequent structure-based functional analyses illustrated the important mechanisms of P2X receptors including trimer formation, ATP recognition, and ATP-dependent activation, as well as competitive and non-competitive antagonist actions in the P2X receptor family (**Fig. 1-6**)^{27–29,31,33–35}. However, there remain a lot of questions about the molecular mechanisms of P2X receptors functions, such as oligomerization, ligand selectivity, gating modulation and competitive inhibition. In this thesis, by using X-ray crystallographic and other biological techniques, the following questions of P2X receptor functions are focused and addressed.

1.4.2 Nucleotide selectivity of P2X receptors (in Chapter 2)

Among nucleotide triphosphates, while P2X receptors have high affinity for ATP as an endogenous agonist, P2X receptors have weak affinity for CTP, but lack affinities for GTP and UTP (**Fig. 1-7**)^{36–38}. Although some P2X receptor structures were presented in complex with ATP^{28,34}, the mechanism of the nucleotide base specificity of P2X receptors remains elusive, due to the lack of structural information for the P2X receptor in complex with other nucleoside triphosphates.

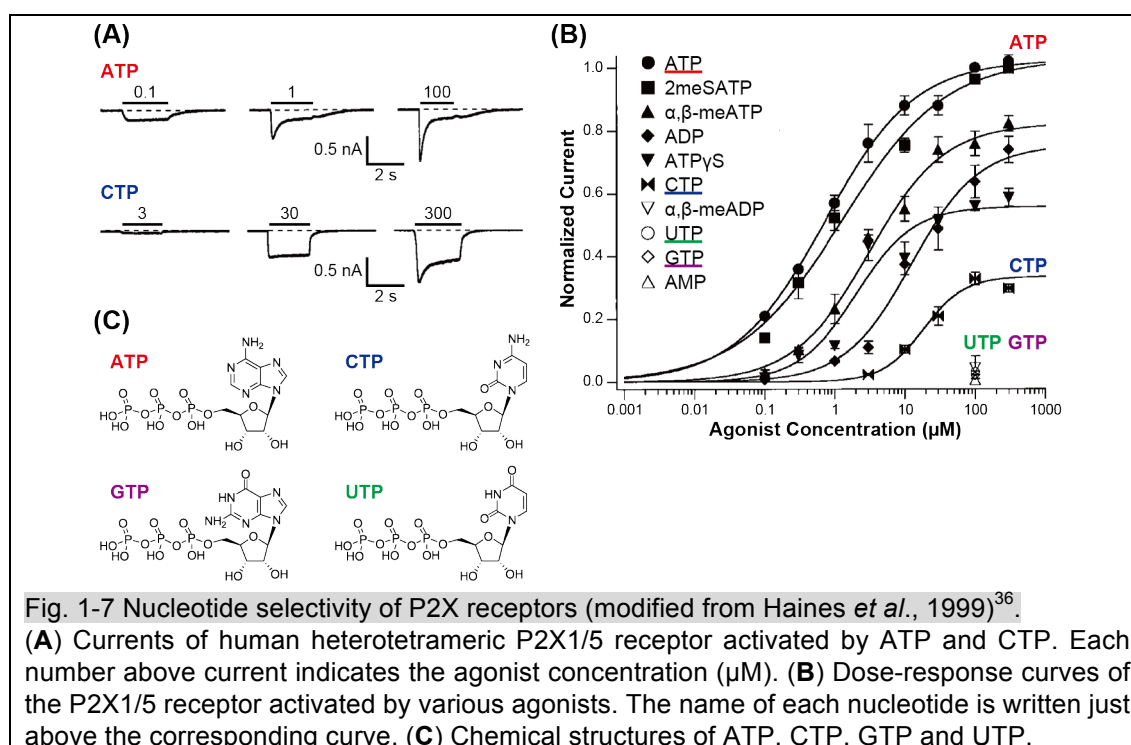
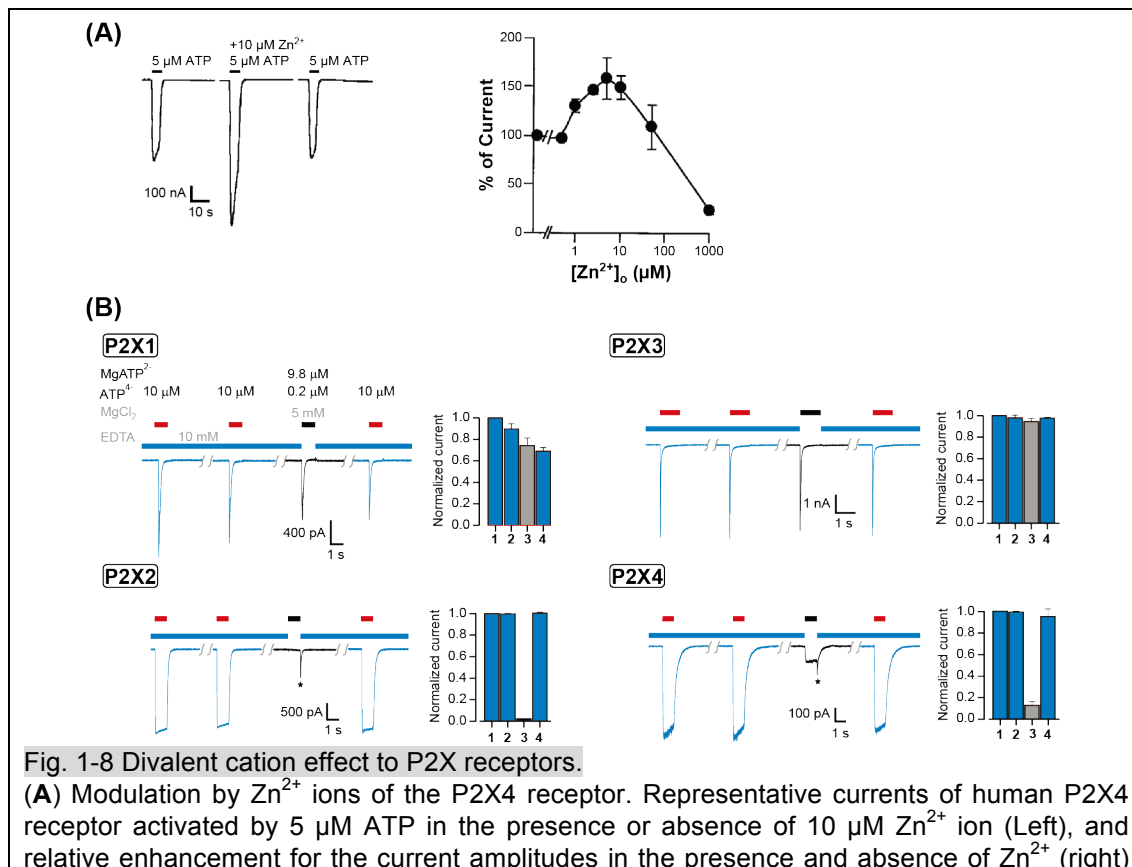


Fig. 1-7 Nucleotide selectivity of P2X receptors (modified from Haines *et al.*, 1999)³⁶.

(A) Currents of human heterotetrameric P2X_{1/5} receptor activated by ATP and CTP. Each number above current indicates the agonist concentration (μM). **(B)** Dose-response curves of the P2X_{1/5} receptor activated by various agonists. The name of each nucleotide is written just above the corresponding curve. **(C)** Chemical structures of ATP, CTP, GTP and UTP.

1.4.3. Divalent cation modulations of P2X receptors (in Chapter 3)

The activation of P2X receptors is modulated by divalent cations such as Zn^{2+} and Mg^{2+} to diversify their physiological functions³⁸⁻⁴¹. For instance, in some P2X receptors such as P2X4 subtype, a Zn^{2+} ion potentiates the ATP-dependent currents, which leads to insulin secretion (**Fig. 1-8A**). Moreover, a Mg^{2+} ion binds to ATP to form MgATP^{2-} , and action of MgATP^{2-} and Mg^{2+} -free ATP to P2X receptors differs among subtypes of P2X receptors. While the fast-desensitizing P2X receptors, such as P2X1 and P2X3, can be activated by both MgATP^{2-} and Mg^{2+} -free ATP with similar efficacies, the slowly desensitizing P2X receptors, such as P2X2 and P2X4, can be activated by Mg^{2+} -free ATP, but MgATP^{2-} exhibits only low efficacy with these receptors (**Fig. 1-8B**). However, the molecular mechanisms of the divalent cation modulation of the P2X receptors have still proved elusive, due to the lack of structural information for the P2X receptor in complex with divalent cations.



are presented (modified from Garcia-Guzman *et al.*, 1999)⁴². **(B)** MgATP²⁻ and Mg²⁺-free ATP effect to the P2X receptors. Representative currents of P2X receptors (P2X1, P2X2, P2X3 and P2X4) activated by 10 μ M ATP in the absence and presence of Mg²⁺, and summary of normalized currents in response to each ATP application are presented. The experiment was performed under the existence of 10 mM EDTA to reduce the other divalent cation effects than Mg²⁺ (modified from Li *et al.*, 2013)⁴¹.

1.4.4. Competitive inhibition mechanism of P2X receptors (in Chapter 4)

The previously determined crystal structures of P2X receptors and subsequent structure-based functional analyses proposed the ATP-dependent activation mechanism^{27,28,30,32,34,35}, in which ATP binding initiates the movement of the some extracellular domain, such as head and dorsal fin domains, toward the ATP binding pocket, which further induces movement of other domains for pore opening (Head and dorsal fin domain correspond to the domain of “Dolphin model”) (**Figs. 1-5B and 1-9A**). Intriguingly, the recent crystallographic and NMR analyses of P2X receptors revealed an unexpected discrepancy regarding the antagonistic mechanism by 2',3'-O-(2,4,6-trinitrophenyl)-ATP (TNP-ATP), one of the subtype non-selective competitive P2X antagonists (**Fig. 1-9B**). The crystal structure of the human P2X3 receptor in complex with TNP-ATP adopted the same conformation as that in the apo, closed state (**Fig. 1-9C,D**)³⁴. In contrast, the NMR analysis of the zebrafish P2X4 receptor showed that TNP-ATP binding induces the expansion of the extracellular domain, in a similar manner to that observed with ATP-dependent activation (**Fig. 1-9E,F**)⁴³. Therefore, further structural analysis revealing the binding and action modes of TNP-ATP to P2X receptors are needed.

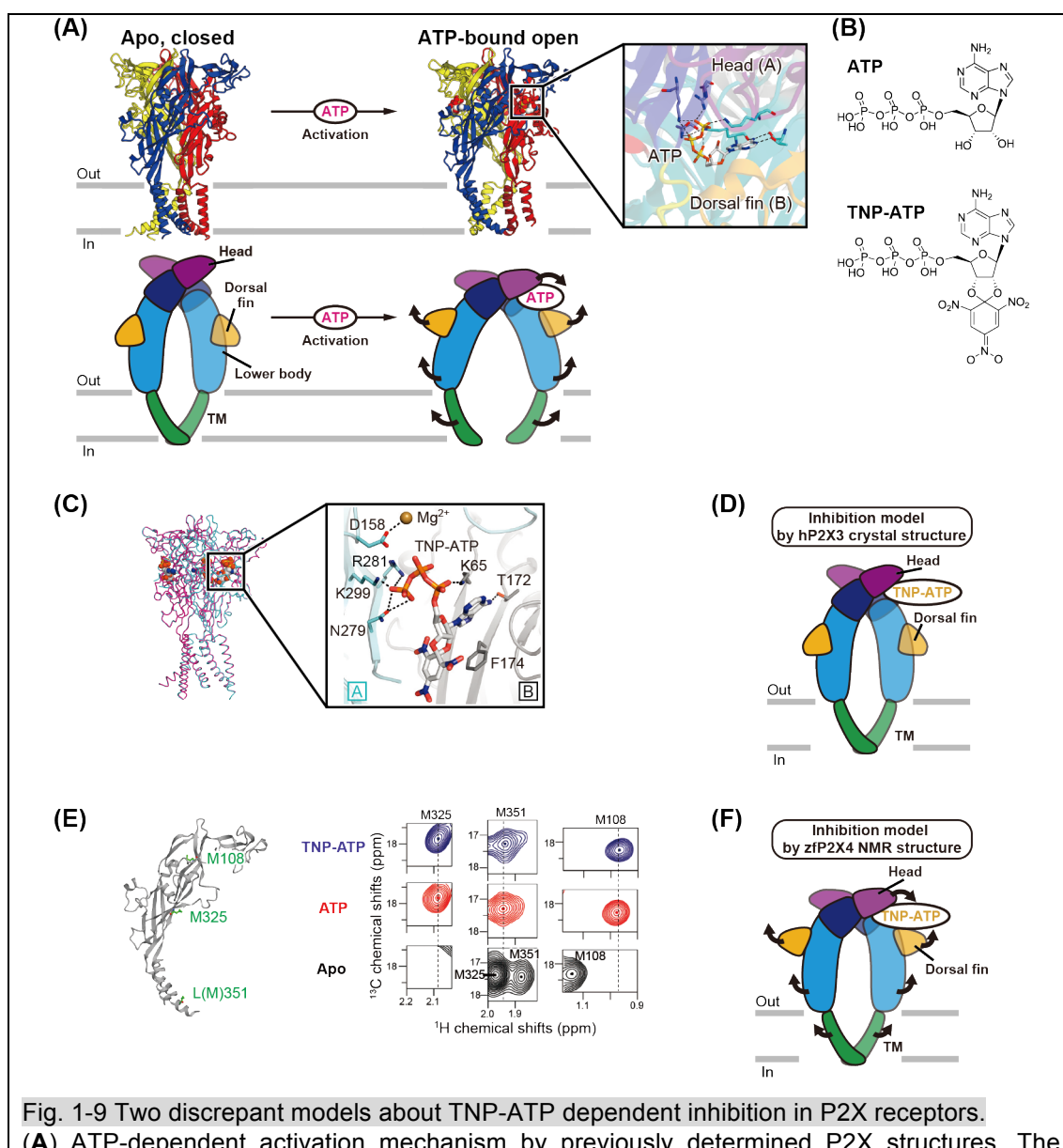


Fig. 1-9 Two discrepant models about TNP-ATP dependent inhibition in P2X receptors.

(A) ATP-dependent activation mechanism by previously determined P2X structures. The structures of apo, closed and ATP-bound open zP2X4 receptors (PDB ID: 4DW0 and 4DW1), and cartoon models corresponding to these states are proposed. **(B)** Chemical structures of ATP and TNP-ATP. **(C)** The superimposition of the apo, closed hP2X3 (cyan, PDB ID: 5SVJ) and TNP-ATP-bound hP2X3 (pink, PDB ID: 5SVQ) structures for structural comparison. The RMSD value is 0.22 Å for 954 Cα atoms between trimers. The enlarged view of TNP-ATP binding site is proposed (modified from Mansoor *et al.*, 2016)³⁴. **(D)** TNP-ATP dependent inhibition site model based on the hP2X3 crystal structure, indicating that TNP-ATP binds to the ATP binding sites but do not induce any conformational change. **(E)** Distribution of the methionine substituted residues mapped onto the ATP-bound zP2X4 structure (PDB ID: 4DW1), and the resonances from methionine residues of TNP-ATP bound state (purple), ATP bound state (red) and Apo state (black) from zP2X4 protein reconstituted in nanodiscs (modified from Minato *et al.*, 2016)⁴³. **(F)** TNP-ATP dependent inhibition model based on the zP2X4 NMR structure, indicating that TNP-ATP binds to the ATP binding sites and induces conformational change similar to ATP.

1.4.5. Thesis composition

Overall, This thesis is composed of five chapters including Introduction (Chapter 1), three results mentioned above (Chapters 2-4) and Overall discussion (Chapter 5). The Figures are inserted at the cited place, and the references are collected at the bottom of the thesis.

Chapter 2: Structural insight into the nucleotide selectivity of P2X receptors

2.1 Introduction

2.1.1 Nucleotide selectivity of P2X receptors

To illustrate the selectivity for various ligands, including agonists, antagonists and modulators, are remained one of the most important questions for the mechanisms of P2X receptors. The previous reports revealed that P2X receptors show affinities for various nucleotide-like compounds that function as agonists or antagonists, which leads to the drug discovery targeting P2X receptors^{13,44}. Among nucleotide triphosphates (ATP, CTP, GTP and UTP) other than ATP, while P2X receptors lack affinities for GTP and UTP, some P2X receptors have weak but significant affinity for CTP (20 to 50 of times lower affinity than for ATP) (**Fig. 1-7**)³⁶⁻³⁸. The previously-determined ATP-bound zebrafish P2X4 structure, and the superimposition of other nucleoside triphosphates onto its ATP binding site, suggested a possible model for the nucleotide base specificity of P2X receptors²⁸. According to this model, a conserved threonine residue within the agonist binding site forms a hydrogen bond with the adenine ring of ATP, but not with the cytosine ring of CTP, and the difference in the number of hydrogen bonds between each nucleotide base and P2X receptors (three for ATP, two for CTP, one for GTP and UTP) is responsible for the stronger affinity for ATP over the other nucleotide triphosphates (**Fig. 2-1**)²⁸. However, the mechanism of the nucleotide base specificity of P2X receptors remains elusive, due to the lack of structural information for the P2X receptor in complex with other nucleoside triphosphates, particularly the low-affinity pyrimidine agonist, CTP. In addition, the mechanism of the pyrimidine base recognition by P2X receptors is quite interesting from the viewpoint of structure-based drug design, because some pyrimidine derivatives act as P2X antagonists^{13,44}.

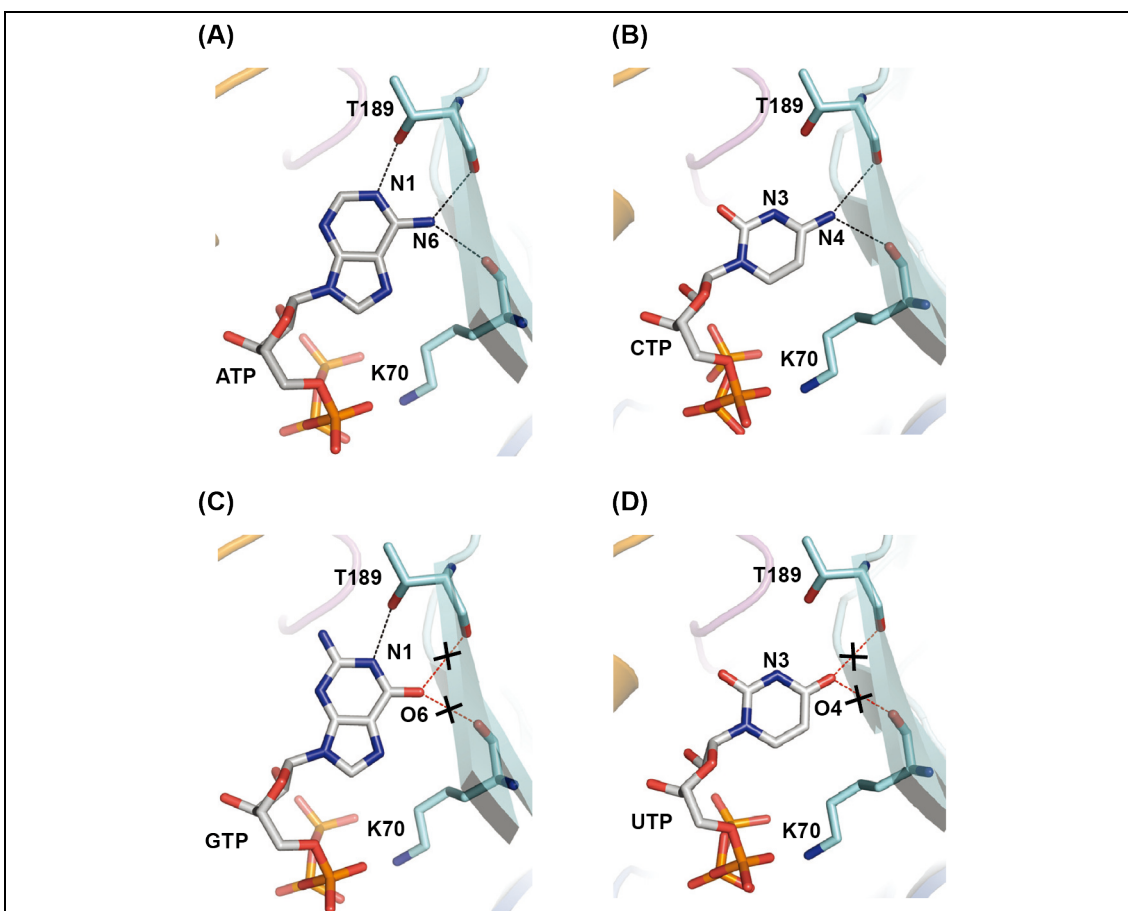


Fig. 2-1 Model for nucleotide base specificity of P2X receptor (modified from Hattori Hattori & Gouaux, 2012)²⁸.

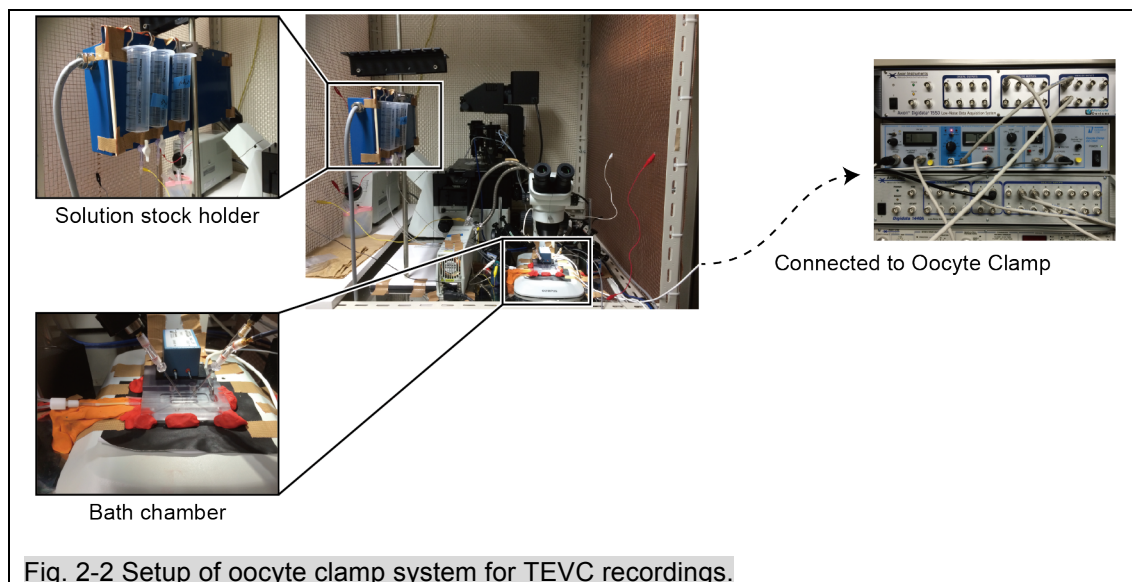
(A-D) Close-up view of the ATP binding site in the ATP-bound open zfP2X4 structure (A). Nucleoside triphosphates and residues involved in ATP binding are labeled and shown in stick representation. Nucleoside triphosphates and residues involved in ATP binding are labeled and shown in stick representation. Superimposition of CTP (B), GTP (C) and UTP (D) onto the ATP at the ATP binding site. Black dashed lines indicate possible hydrogen bonding interactions. Red dashed lines with black crosses indicate non-complementary hydrogen bonding partners despite reasonable distances for hydrogen bonding.

2.1.2 Study purpose

In this study, the crystal structure of zebrafish P2X4 receptor in complex with CTP was determined. Furthermore, structure-based electrophysiological and spectroscopic analyses were conducted to reveal the mechanism underlying the nucleotide base specificity of P2X receptors.

2.2 Revealing nucleotide selectivity of zebrafish P2X4 (zfP2X4) receptor by electrophysiology

First, to assess the nucleotide base specificity of zebrafish P2X4 (zfP2X4), the Two Electrode Voltage Clamp (TEVC) recording of *Xenopus* oocytes system was constructed and performed with the guidance of Associated Prof. Yuichiro Fujiwara (Osaka University) (Fig. 2-2).



2.2.1 Material and methods

2.2.1.1 Plasmid construction of zfP2X4 receptor for electrophysiology

The zfP2X4 gene codes 389 amino acid length protein (NCBI accession number: NP_705939). The full-length gene of the zfP2X4 WT was artificially synthesized (Genscript Co.), and subcloned into pGEMHE vector between the *EcoRI/XbaI* site with the Kozac sequence (5'-GCCACCC-3') just before the start codon ATG. The pGEMHE vector contained 5' and 3' untranslated regions of the β -globin gene from *Xenopus laevis* to enhance protein expression level⁴⁵.

2.2.1.2 RNA preparation and expression of zfP2X4 receptor

Using plasmid DNA prepared in 2.2.1.1 and a mMessage mMachine® T7 ULTRA kit (Ambion Co.), the zfP2X4 WT RNA was synthesized. *Xenopus laevis* oocytes were kindly provided by Prof. Kazushige Touhara (The University of Tokyo), and the synthesized RNA was injected for 100 ng into the oocytes. The oocytes were incubated at 18 °C in ND96 Barth's solution, containing 88 mM NaCl, 1 mM KCl, 2.4 mM NaHCO₃, 10 mM HEPES, 0.33 mM Ca(NO₃)₂, 0.41 mM CaCl₂, and 0.82

mM MgSO₄, pH 7.4, supplemented with 50 µg/ml gentamicin, and were used for recording after 2-3 days.

2.2.1.3 Electrophysiological recordings of zfp2X4 receptor

Oocytes expressing zfp2X4 WT were fixed at the 725II bath clamp headstage (WARNER Co.), and then held at -70 mV with a bath-clamp amplifier (OC-725C, Warner Co.). Recording solutions contained 100 mM NaCl, 5 mM HEPES, 2 mM MgCl₂, pH 7.3, and nucleoside triphosphates (ATP, CTP, GTP, and UTP), which were freshly prepared each day. Macroscopic currents were recorded and analyzed using the pClamp 10 software (Molecular Devices Co.)^{46,47}.

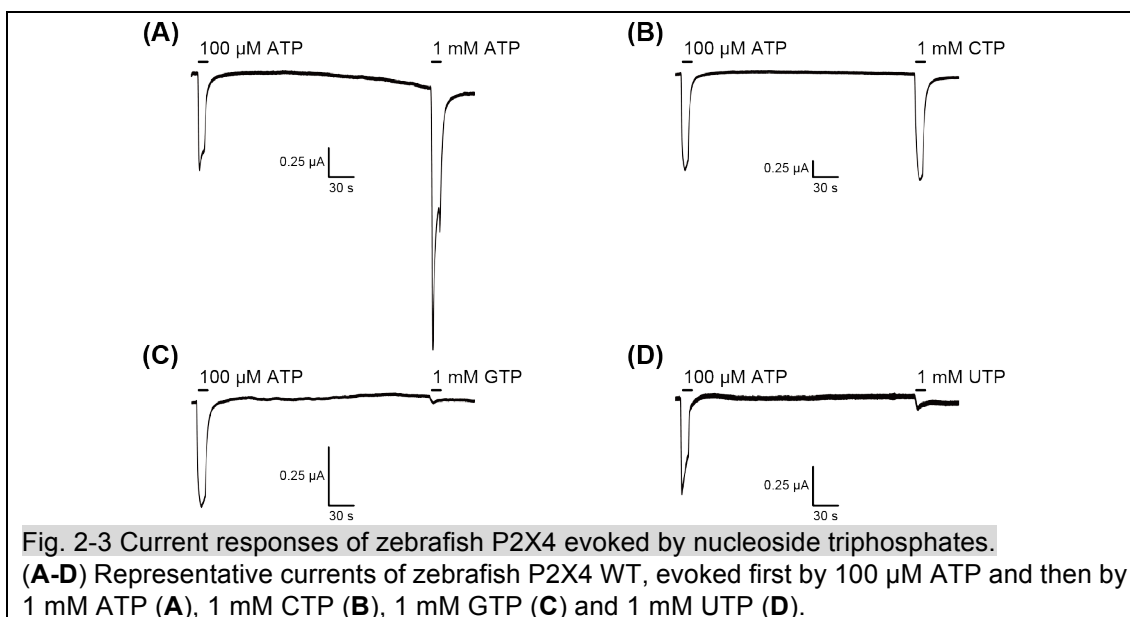
2.2.2 Results

2.2.2.1 Electrophysiological recordings of zfp2X4 receptor

Following the methods in 2.2.1, the TEVC recordings of *Xenopus* oocytes expressing zfp2X4 WT were performed. As shown previously⁴⁸, the initial “priming” application with a low concentration of ATP increases P2X receptors sensitivity to second or more applications of ligands, which is useful for evaluating the affinity of ligands. Therefore, the zfp2X4-associated currents were evoked by the application of high concentrations (1 mM) of nucleoside triphosphates (ATP, CTP, GTP and UTP), following the prior application of 100 µM ATP. The specific ATP- and CTP-evoked currents (**Fig. 2-3A,B**) were detected while no GTP- and UTP- evoked currents were detected (**Fig. 2-3C,D**).

2.2.2.2 Nucleotide selectivity of zfp2X4 receptor

The results from 2.2.2 showed that the zfp2X4 is activated by ATP and CTP but not by GTP and UTP, consistent with the previous electrophysiological analyses of P2X receptors^{36–39,42,49–51}.



2.3 Structure determination of the zfP2X4 receptor in the presence of CTP by X-ray crystallography

To investigate the CTP recognition mechanism, the zfP2X4 was crystallized in the presence of CTP.

2.3.1 Material and methods

2.3.1.1 Plasmid construction of zfP2X4 receptor for structural determination

The previous reports providing the ATP-bound zfP2X4 structure found out the zfP2X4 construct that yields the ATP-bound crystals diffracting to 2.8 Å resolution²⁸. Therefore, the same construct of zfP2X4, termed Δ P2X4-C was used for this study. The Δ P2X4-C construct lacks the regions encoding 27 N-terminal and 24 C-terminal residues, which were predicted to be structurally disordered, and includes the mutations of Asn78 and Asn187 to exclude putative glycosylation sites (Δ N27/ Δ C24/N78K/N187R). The Δ P2X4-C construct was subcloned into pFastBac modified vector (Thermo Fisher Scientific Co.) with N-terminal His8-EGFP tag fusion, and a thrombin cleavage site between the Δ P2X4-C and EGFP.

2.3.1.2 Baculovirus preparation of the crystallization construct (Δ P2X4-C)

The baculovirus was prepared following the Bac-to-Bac system protocol (Invitrogen). The plasmid containing the EGFP-tagged $\Delta P2X4$ -C was transformed into *E. coli* DH10BacTM (Life technologies Co.). The transformed *E. coli* was streaked on the LB selection agar media containing 50 μ g/ml Kanamycin, 7 μ g/ml Gentamycin, 10 μ g/ml Tetracycline, 100 μ g/ml X-gal and 0.2 mM IPTG. After 2 days incubation at 37°C, the white colony was selected and inoculated in the LB selection media containing 50 μ g/ml Kanamycin, 7 μ g/ml Gentamycin and 10 μ g/ml Tetracycline, O/N. The bacmid DNA was isolated by isopropanol precipitation method, and transfected into insect Sf9 cells (ATCC® CRL-1711TM) by using Fugene® HD Transfection Reagent (Promega Co.). After 4 days incubation at 27°C, the supernatant was collected and stored as P1 virus stock. Then, 0.1% (v/v) P1 virus was added to the Sf9 cells (1.0×10^6 cells/ml, 1L), and incubated 4 days. The supernatant was collected by centrifugation ($5,000 \times g$, 10 min, 4°C) and stored as P2 virus stock at 4°C.

2.3.1.3 Expression and purification of the $\Delta P2X4$ -C

The $\Delta P2X4$ -C construct was expressed by adding 10% P2 virus stock to Sf9 cells (3.0×10^6 cells/ml, 1L), and by incubating at 27°C in 1 day and following at 20°C in 2 days. Cells were collected by centrifugation ($5000 \times g$, 10 min, 4 °C) and broken by sonication in buffer containing 50 mM Tris, pH 8.0, 150 mM NaCl supplemented with 5.2 μ g/ml aprotinin, 2 μ g/ml leupeptin, and 1.4 μ g/ml pepstatinA (all from Calbiochem Co.). Cell debris was removed by centrifugation ($10,000 \times g$, 10 min, 4 °C). Membrane was collected by ultracentrifugation ($138,000 \times g$, 1 h, 4 °C). The membrane fraction was solubilized for 1 h at 4 °C in a buffer (50 mM Tris, pH 8.0, 150 mM NaCl, 15% glycerol, 2% n-dodecyl- β -D-maltoside (DDM) (Calbiochem)). Insoluble materials were removed by ultracentrifugation ($138,000 \times g$, 1 h, 4°C), and the supernatant was incubated with Talon metal affinity resin (Clontech Co.), washed with 20 mM imidazole and eluted with 250 mM imidazole. After Thrombin protease digestion, the fraction was purified by size-exclusion chromatography on a Superdex 200 Increase 10/300 GL column (GE Healthcare Co.), equilibrated with SEC buffer (20 mM HEPES, pH 7.0, 80 mM NaCl, 20 mM KCl, 15% glycerol, 0.05% DDM)

(**Fig. 2-4A**). Peak fractions were pooled, concentrated to 2 mg/ml, using a centrifugal filter unit (Merck Millipore Co., 50 kDa molecular weight cutoff).

2.3.1.4 Co-crystallization of the Δ P2X4-C with CTP

The crystallization of the Δ P2X4-C with CTP was performed by using cross-seeding method. First, to obtain Δ P2X4-C crystals for nuclei, the ATP-bound Δ P2X4-C crystals were grown at 4°C in 3-4 days by the vapor diffusion method, by mixing protein and 1 mM ATP, then further mixing 1:1, 2:1, or 1:2 (v/v) ratios of ATP-added protein and reservoir solutions (20-26% PEG 2000, 300 mM $\text{Mg}(\text{NO}_3)_2$, and 100 mM Tris, pH 8.0). Then, the “1st-generation” CTP-bound Δ P2X4-C crystals were grown under the same conditions by mixing protein and 3 mM CTP, then further mixing CTP-added protein and reservoir solutions using the “ATP-bound Δ P2X4-C crystals” as nuclei for the cross-seeding method. The “2nd-generation” CTP-bound Δ P2X4-C crystals were grown under the same conditions, by the cross-seeding method using the “1st-generation” CTP-bound Δ P2X4-C crystals as nuclei (**Fig. 2-4B**). The “2nd-generation” CTP-bound Δ P2X4-C crystals were harvested and cryoprotected, in a solution (25% PEG 2000, 300 mM $\text{Mg}(\text{NO}_3)_3$, 100 mM Tris, pH 8.0, 25% glycerol, 0.05% DDM and 3 mM CTP). Crystals were flash-frozen in liquid nitrogen for X-ray diffraction experiments.

50 kDa molecular weight cutoff).

2.3.1.5 Data collection and structure determination

X-ray diffraction data were collected at 100 K on the SPring-8 beamline BL41XU (Hyogo, Japan) (**Fig. 2-4C**). Diffraction data were processed using HKL2000 (HKL Research Inc.). The structure of CTP-bound Δ P2X4-C was obtained by molecular replacement with Phaser⁵², using the ATP-bound Δ P2X4-C structure (PDB ID: 4DW1) as the template. The determined structure was further refined by using the programs PHENIX⁵³ and COOT⁵⁴. Crystallographic data and refinement statistics are presented in the figure (**Fig. 2-4D**). The coordinate of the CTP-bound Δ P2X4-C structure was deposited on Protein Data Bank (PDB) under the accession code 5WZY.

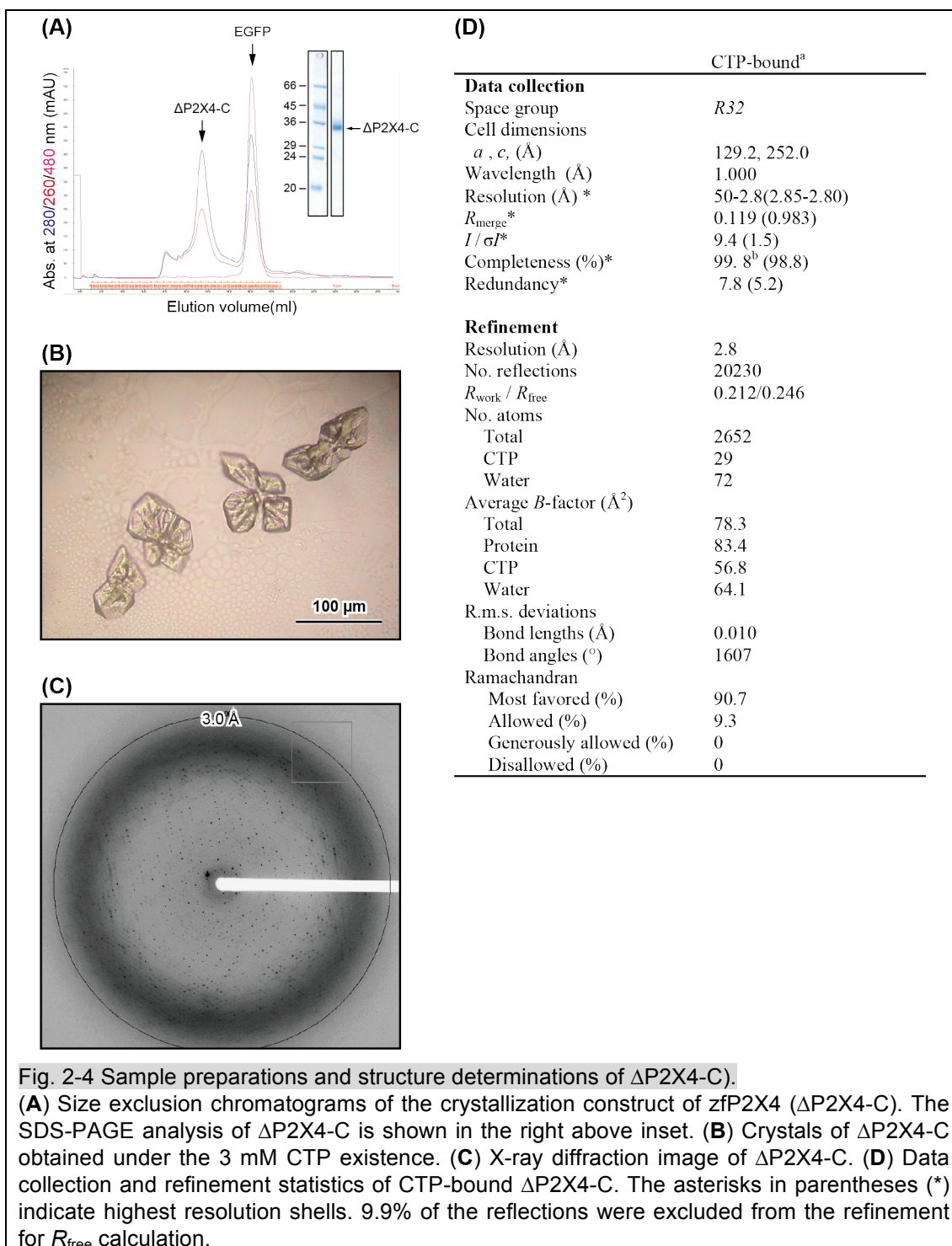


Fig. 2-4 Sample preparations and structure determinations of Δ P2X4-C).

(A) Size exclusion chromatograms of the crystallization construct of zfpP2X4 (Δ P2X4-C). The SDS-PAGE analysis of Δ P2X4-C is shown in the right above inset. **(B)** Crystals of Δ P2X4-C obtained under the 3 mM CTP existence. **(C)** X-ray diffraction image of Δ P2X4-C. **(D)** Data collection and refinement statistics of CTP-bound Δ P2X4-C. The asterisks in parentheses (*) indicate highest resolution shells. 9.9% of the reflections were excluded from the refinement for R_{free} calculation.

2.3.2 Results

2.3.2.1 Overall structure of the CTP-bound zfpP2X4

To investigate the CTP recognition mechanism, the zebrafish P2X4 construct (Δ P2X4-C) in the presence of 3 mM CTP was crystallized. Then X-ray diffraction data were collected to 2.8 Å

resolution, successfully led to determine the structure (**Fig. 2-5**). The subunit of CTP-bound structure (**Fig. 2-5A,B**) is quite consistent with that of the previously determined ATP-bound structure (**Fig. 2-5D,E**), with root mean square deviation (RMSD) values below 0.4 Å for 324 Cα atoms (**Fig. 2-5H**), indicating that CTP can trigger the conformational changes similar to those by ATP²⁸. The overall structure forms a chalice-like shape assembled into a homotrimeric architecture, with a large extracellular domain and a small transmembrane domain, that is consistent with the previously determined P2X structures^{27,28,34,35}. Each subunit has two transmembrane helices and resembles the shape of a dolphin²⁷ (**Fig. 2-5G**). At the agonist binding site, a strong residual electron density for the nucleoside triphosphate was observed (**Fig. 2-5C**). The shape of the electron density for the base group was smaller than that in the ATP-bound structure, and could be readily assigned as the cytosine of the CTP molecule (**Fig. 2-5C,F**).

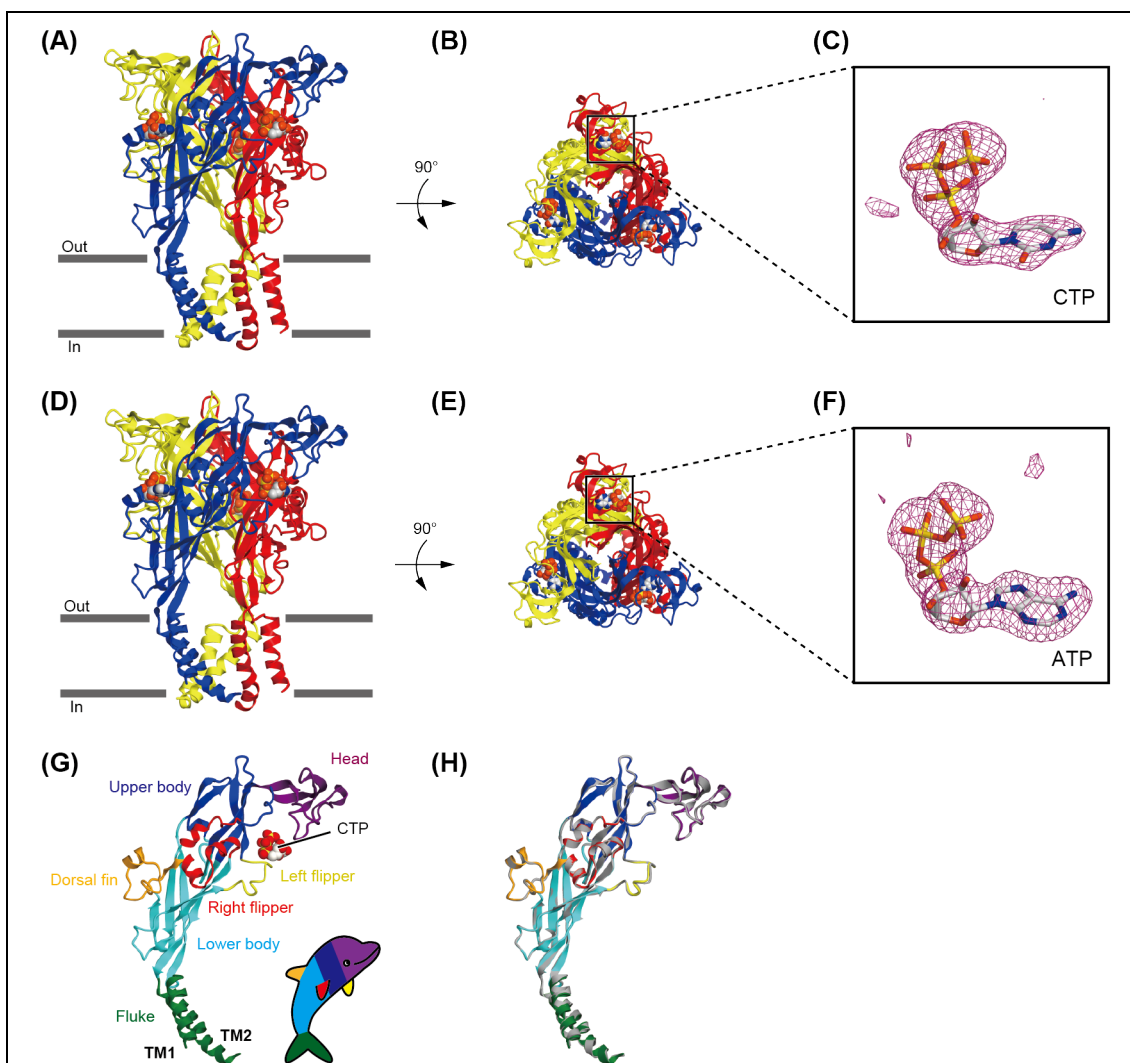


Fig. 2-5 Overall comparisons of the CTP-bound and ATP-bound $\Delta P2X4-C$ structures. (A,B) The CTP-bound $\Delta P2X4-C$ structure viewed parallel to the membrane (A) and from the extracellular side (B). (C) The omit $F_o - F_c$ map contoured at 4σ , showing the electron density of CTP. (D,E) The ATP-bound $\Delta P2X4-C$ structure viewed parallel to the membrane (D) and from the extracellular side (E). (F) The omit $F_o - F_c$ map contoured at 4σ , showing the electron density of ATP. (G) The CTP-bound $\Delta P2X4-C$ subunit, colored according to the dolphin-like model²⁷. (H) Superimposition of the CTP-bound (colored) and the ATP-bound $P2X4-C$ (grey) structures, using the $C\alpha$ atoms of the protomers.

2.3.2.2 Cytosine base recognition

In the CTP-bound structure, the phosphate groups of CTP adopt a bent conformation and are directly recognized by the side chains of N296, R298, K316 from one subunit, and K70 and K72 from the adjacent subunit (Fig. 2-6A,B), consistent with the ATP-bound structure (Fig. 2-6C,D). However, the cytosine base of CTP is recognized by the receptor in a different manner from ATP (Fig. 2-6). While the side chain of the conserved threonine, T189, forms a hydrogen bond with the

adenine ring in the ATP-bound structure (**Fig. 2-6C,D**), there is no equivalent hydrogen bond between the cytosine ring and the side chain of T189 in the CTP-bound structure (**Fig. 2-6A,B**). Instead, we identified another hydrogen bond between the cytosine base and the receptor. The O atom of the cytosine interacts with the side chain of R143 (**Fig. 2-6A,B**), which had not been predicted in the previous superimposed model based on the ATP-bound structure²⁸. Furthermore, the NH₂ atom of cytosine is recognized by the main chain carbonyl oxygen atoms of K70 and T189 (**Fig. 2-6A,B**), as similarly observed in the ATP-bound structure (**Fig. 2-6C,D**), but their bond lengths seem to be 0.4–0.5 Å longer in the CTP-bound structure (**Fig. 2-6B,D**). Although it is difficult to conclude whether these bonds are really extended or not at this resolution of 2.8 Å, it should be noted that the residues constituting the agonist binding site are well ordered with lower B-factors and clear electron density in both the ATP-bound and CTP-bound structures (**Fig. 2-7A-D**). Overall, the structural comparison between the CTP-bound and ATP-bound structures suggested that both CTP and ATP form three hydrogen bonds between their nucleotide bases and the receptor, but employ different residues (**Fig. 2-6**). This result totally differs from the previously proposed model by superposing CTP onto ATP in the ATP-bound structure, in which the cytosine ring of CTP was predicted to form only two hydrogen bonds with the receptor²⁸.

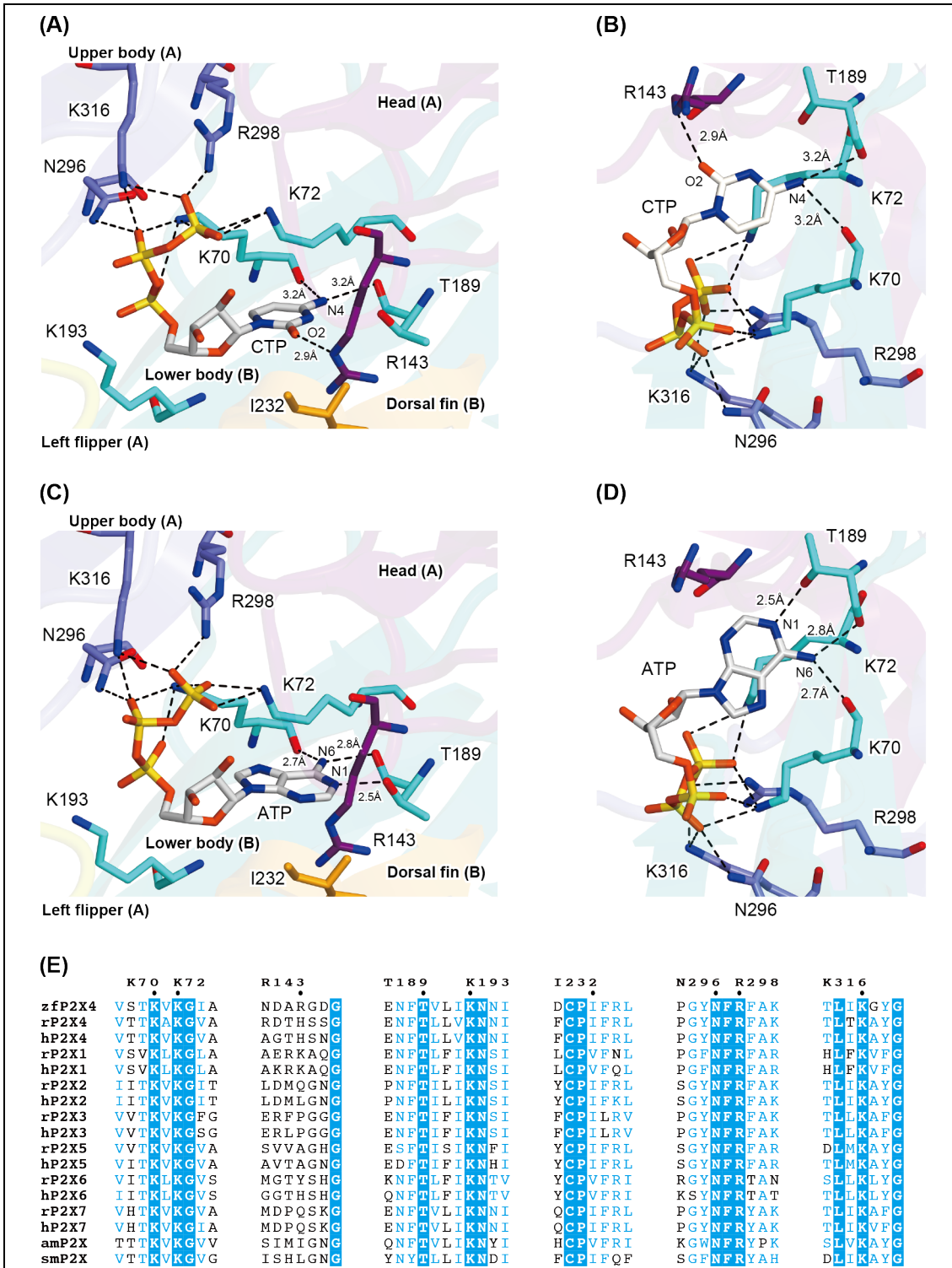
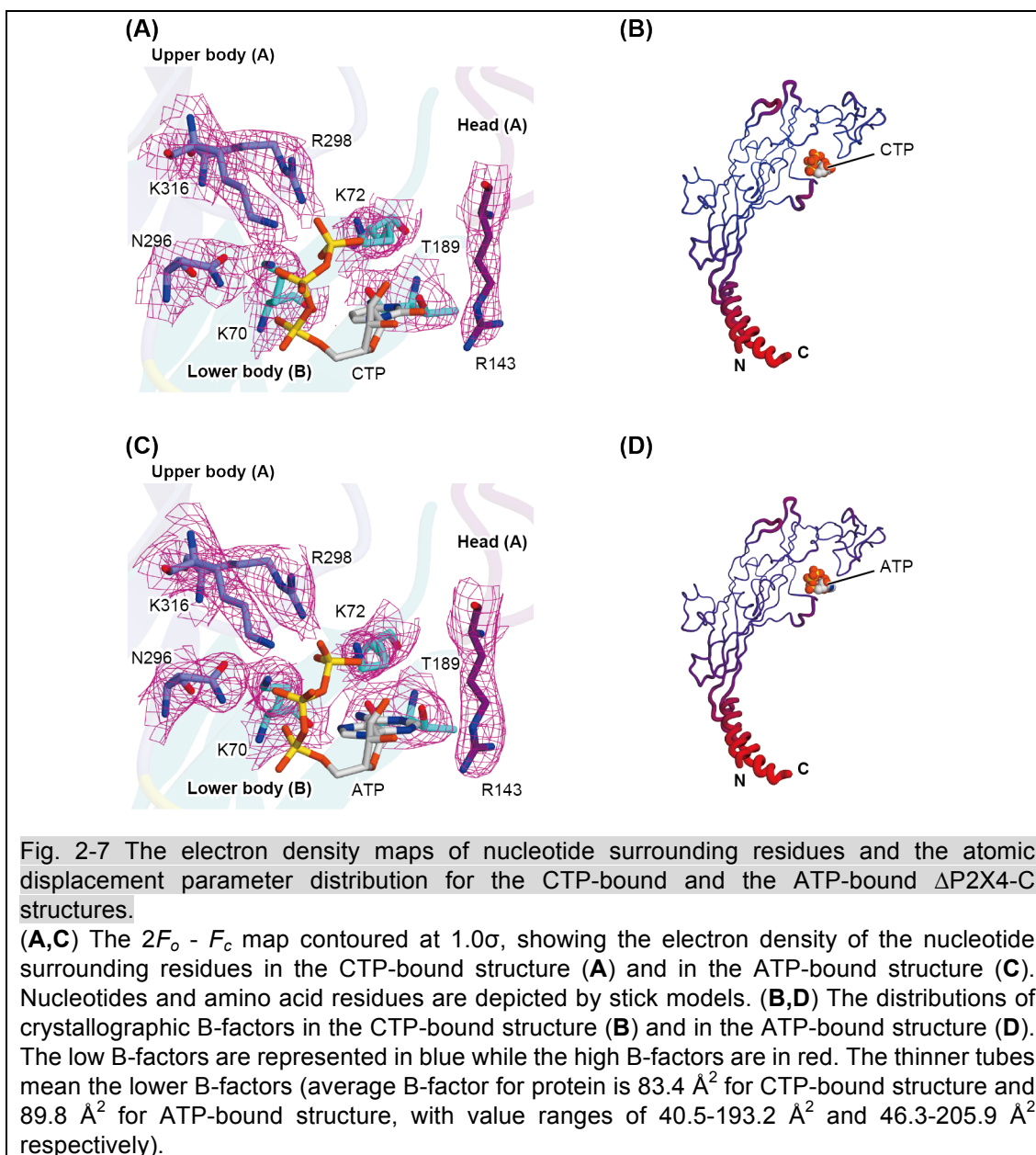


Fig. 2-6 Close-up views of the CTP and ATP binding sites.

(A-D) Close-up views of the CTP binding site in the CTP-bound Δ P2X4-C structure (A,B), and the ATP binding site in the ATP-bound Δ P2X4-C structure (C,D). Side chains of amino acid residues and nucleoside triphosphates are depicted by stick models. The molecule is colored according to the previously proposed dolphin-like model. Each dotted black line and number indicates a hydrogen bond and its length (<3.3 Å) respectively. (E) Sequence alignment around agonist binding site of P2X receptors. Amino acid sequences were aligned using Clustal Omega and are shown using ESPrnt3. For the sequence alignment, zebrafish P2X4

(zfP2X4, NCBI accession number: 12656589) and the following P2X receptors were used: human (hP2X1, 4505545; hP2X2, 25092719; hP2X3, 28416925; hP2X4, 116242696; hP2X5, 209572778; hP2X6, 6469324; and hP2X7, 29294631), rat (rP2X1, 1352689; rP2X2, 18093098; rP2X3, 1030065; rP2X4, 1161345; rP2X5, 1279659; rP2X6, 1279661; and rP2X7, 1322005), Gulf Coast tick (amP2X, GI: 346469461), and blood fluke (smP2X, 51988420).



2.4 Mutation assay of the amino acid residues at the agonist binding site by electrophysiology

To further investigate the functional roles of the residues involved in the base recognition, T189 and R143, the electrophysiological analysis with the rat P2X4 (rP2X4) was performed, since

Xenopus oocytes expressing zP2X4 mutants had the low potency of ATP³³ and electrophysiological properties of rP2X4 including nucleotide selectivity have been well established^{33,55–57}.

2.4.1 Material and methods

2.4.1.1 Plasmid construction, RNA preparation and expression of rat P2X4 (rP2X4) receptor

The rat P2X4 (rP2X4) gene codes 388 amino acid length protein (NCBI accession number: NP_113782.1). The full-length gene of the rP2X4 WT was artificially synthesized (Genscript Co.), and subcloned into pGEMHE vector in a similar manner of zP2X4 as described in the section 2.2.1.1. The rP2X4 mutants were generated by the QuickChange method. The RNAs from rP2X4 WT and mutants were synthesized in a similar manner of zP2X4 as described in the section 2.2.1.2. The synthesized RNA was injected for 20 ng into the oocytes. The oocytes were incubated at 18 °C in ND96 Barth's solution supplemented with 50 µg/ml gentamicin, and were used for recording after 2-3 days.

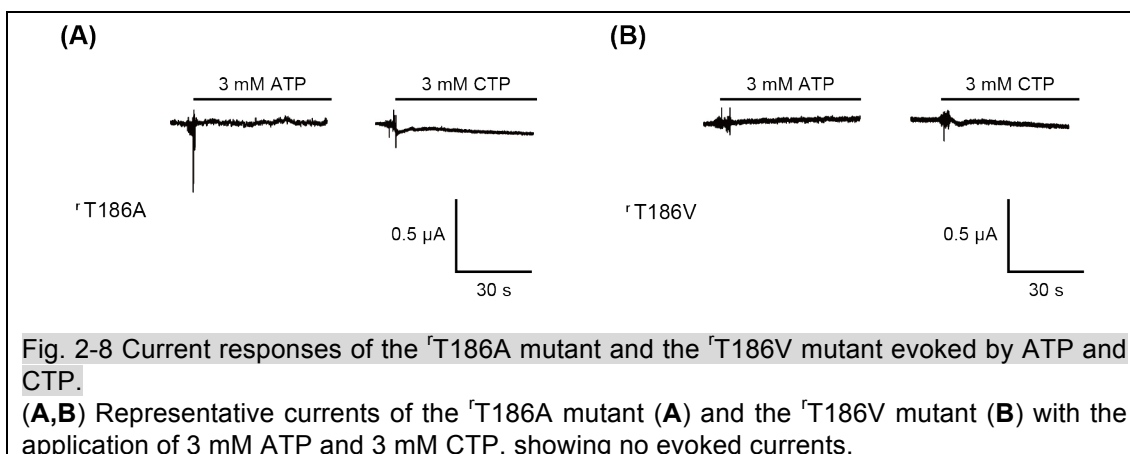
2.4.1.2 Electrophysiological recordings of rP2X4 receptor

Electrophysiological recordings of rP2X4 WT and mutants were performed using similar method for zP2X4 as described in the section 2.2.1.3.

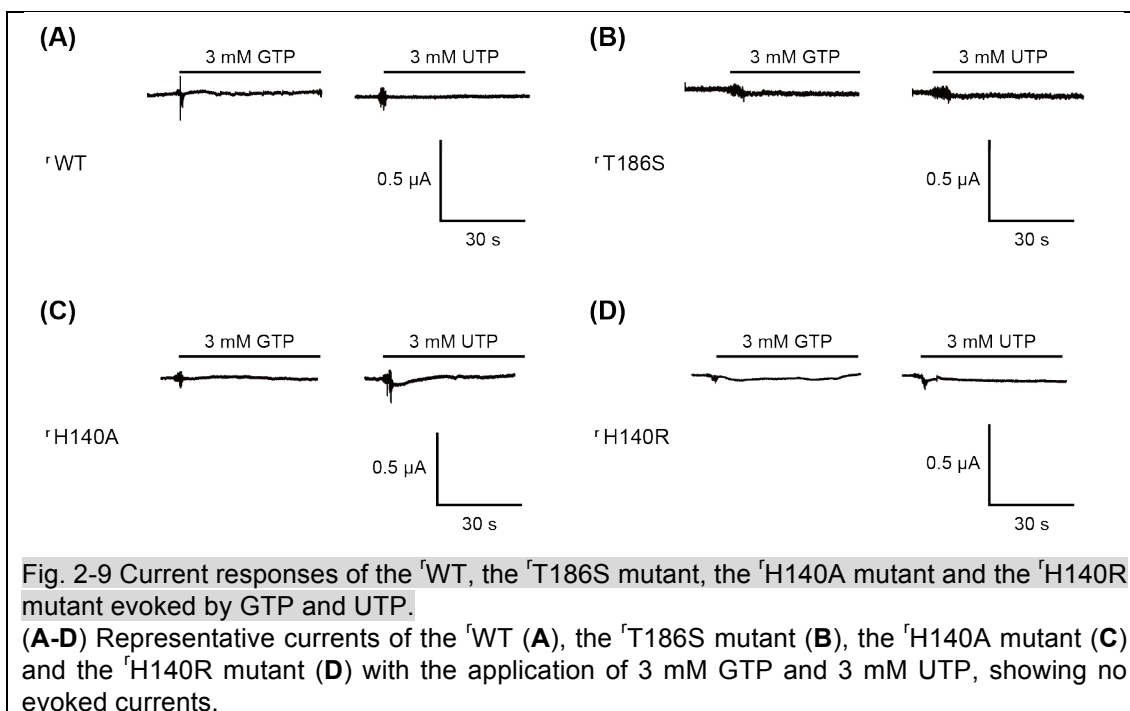
2.4.2 Results

2.4.2.1 Mutation assay of conserved threonine residue

First, to assess the functional role of T189 in zP2X4, three mutants of rat P2X4 at the equivalent residue of the zP2X4 was created (^rT186A, ^rT186V and ^rT186S; the superscript “r” means rat P2X4). While ATP- and CTP-evoked currents were detected from oocytes expressing the ^rWT and the ^rT186S mutant, no ATP- and CTP-evoked currents were detected from oocytes expressing the ^rT186A and ^rT186V mutants (**Fig. 2-8**), indicating the hydrophilic environment provided by the side chain of amino acid residue at this position might be important for the channel activity.



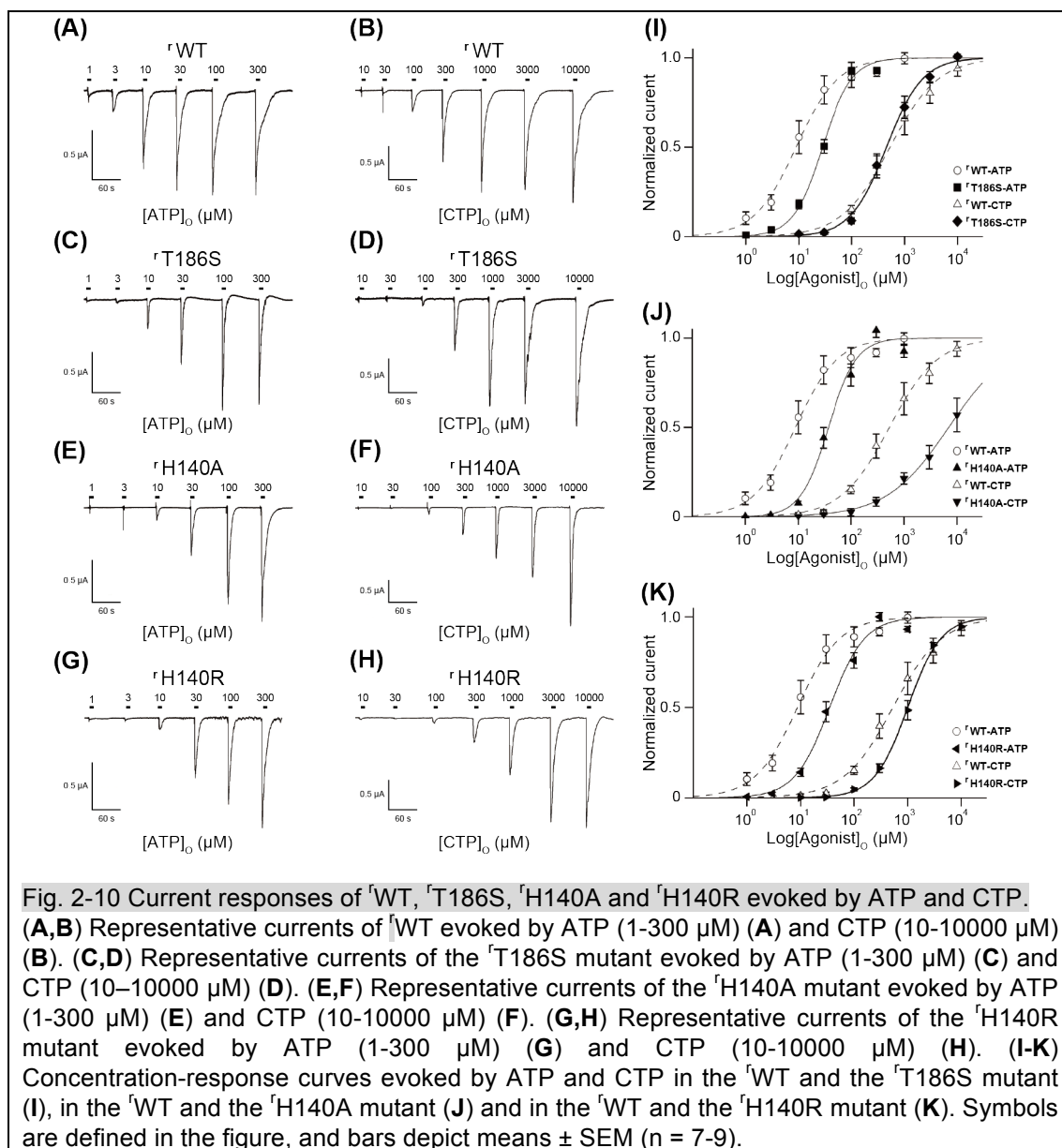
Therefore, the ^rWT and the ^rT186S mutant were further examined. The dose-response relationships to ATP and CTP in the ^rWT and the ^rT186S mutant were analyzed, since no GTP- and UTP-evoked currents were detected from the ^rWT and the ^rT186S mutant (**Fig. 2-9A,B**).



The ^rT186S mutant exhibited reduced ATP affinity ($EC_{50} = 29.9 \pm 3.1 \mu M$, $n = 9$) (**Fig. 2-10C,I**) as compared with ^rWT ($EC_{50} = 16.2 \pm 5.4 \mu M$, $n = 9$) (**Fig. 2-10A,I**), whereas the ^rT186S mutant exhibited similar CTP affinity ($EC_{50} = 557 \pm 120 \mu M$, $n = 9$) (**Fig. 2-10D,I**) as compared with ^rWT ($EC_{50} = 564 \pm 170 \mu M$, $n = 9$) (**Fig. 2-10B,I**). These results are consistent with the ATP-bound and CTP-bound structures in which the side chain of ^rT186 forms a hydrogen bond with the adenine ring, but not with the cytosine ring (**Fig. 2-6**).

2.4.2.2 Mutation assay of basic residue

Next, the functional role of R143 in zfp2X4 was assessed, as its side chain forms a hydrogen bond with the cytosine ring in the CTP-bound structure (**Fig. 2-6A,B**). This arginine residue is substituted with a similar basic residue, histidine (^tH140), in rat P2X4 (**Fig. 2-6E**). Since the side chain of arginine is also suggested to interact with the O atom of the cytosine, the corresponding mutants (^tH140A and ^tH140R) of ^tH140 were created and tested. The dose-response relationships to ATP and CTP in the ^tWT and the ^tH140 mutants were analyzed, while no GTP- and UTP-evoked currents were detected from the rWT and the ^tH140 mutants (**Fig. 2-9A,C,D**). The ^tH140A mutant exhibited about 2.5-fold reduced ATP affinity ($EC_{50} = 42.8 \pm 6.3 \mu\text{M}$, $n = 8$) (**Fig. 2-10E,J**) and 14-fold reduced CTP affinity ($EC_{50} = 7990 \pm 1500 \mu\text{M}$, $n = 7$) (**Fig. 2-10F,J**) as compared with ^tWT while the ^tH140R mutant exhibited about 2-fold reduced both ATP affinity ($EC_{50} = 39.4 \pm 5.0 \mu\text{M}$, $n = 10$) (**Fig. 2-10G,K**) and CTP affinity ($EC_{50} = 1100 \pm 140 \mu\text{M}$, $n = 9$) (**Fig. 2-10H,K**) as compared with ^tWT. The large decrease in the CTP affinity of the ^tH140A mutant suggested that the hydrogen bond between the basic residue and the cytosine is also conserved in rat P2X4, and is responsible for the affinity for CTP. ^tH140 is similarly conserved among the P2X1 and P2X4 receptors, primarily as a basic amino residue (**Fig. 2-6E**). Furthermore, P2X3 receptors possess a conserved basic residue as the neighbor of ^tH140 (**Fig. 2-6E**). Consistently, CTP functions as a weak affinity agonist for P2X1 (ref. 51), P2X3 (ref. 38) and P2X4 (refs. 39 and 42).



2.5 Infrared difference spectroscopy upon the ATP and CTP binding

To further investigate the nucleotide binding specificity of zfp2X4, ligand-binding induced difference Attenuated total reflectance (ATR)-Fourier-transform infrared (FTIR) spectroscopy was applied and conducted on the WT and conserved threonine mutants (T189S and T189V) of $\Delta\text{P2X4-C}$.

2.5.1 Material and methods

2.5.1.1 Protein preparation of zfp2X4

The plasmids encoding mutants (^{zf}T189A and ^{zf}T189V) of crystallization construct Δ P2X4-C ^{zf}WT were generated by the QuickChange method. These zfp2X4 constructs were expressed in Sf9 cells and purified in a similar manner described in the section 2.3.1.3.

2.5.1.2 ATR-FTIR measurement

Each zfp2X4 protein was reconstituted into liposome at a protein:lipid (POPC) ratio of 1:100 (mol/mol) in the presence of the recording buffer (150 mM NaCl, 20 mM HEPES, pH 7.0)^{58,59}. After exchanging the buffer to 2 mM NaHPO₄, 10 mM NaCl, pH 7.5, the reconstituted liposomes containing ~6 μ g of the purified zfp2X4 protein were placed on a diamond ATR crystal (Smith Detection, DurasamplIR II, nine effective internal reflections with an incident angle of 45°). After drying in a gentle stream of N₂, the sample was filled with the recording buffer. Before obtaining the spectrum, the sample was washed with the recording buffer at a flow rate of 1 ml/min for ~1 h. ATR-FTIR spectra of the samples were recorded at 25°C and 2 cm⁻¹ resolution using a VERTEX 70 spectrometer (Bruker Optics) equipped with a liquid-nitrogen-cooled MCT detector. A spectrum of the sample in the recording buffer was recorded, and the recording buffer was then switched to the recording buffer supplemented with 10 μ M ATP or CTP, and after washing for 15 min to reach equilibrium, the spectrum of the sample in the presence of the nucleotides was recorded. For each spectrum, 768 interferograms were collected. The obtained difference spectra were normalized based on the absolute absorbance of the amide I band at 1653 cm⁻¹, which well correlates with the quantities of the proteins on the ATR crystals. The absolute absorption spectra of the zfp2X4 proteins immersed in the recording buffer were obtained by subtracting the buffer contribution. After measurement of the absorption spectra before and after the buffer exchange, the difference spectra were calculated by subtracting the two spectra and then correcting for changes due to membrane swelling and non-specific distortions associated with addition of the ligands.

2.5.2 Results

2.5.2.1 ATP and CTP binding ability of conserved threonine residue

The infrared spectra upon binding of ATP or CTP to the z^f WT and conserved threonine mutants (z^f T189S and z^f T189V) of z^f P2X4 were analyzed and compared each other (**Fig. 2-11**).

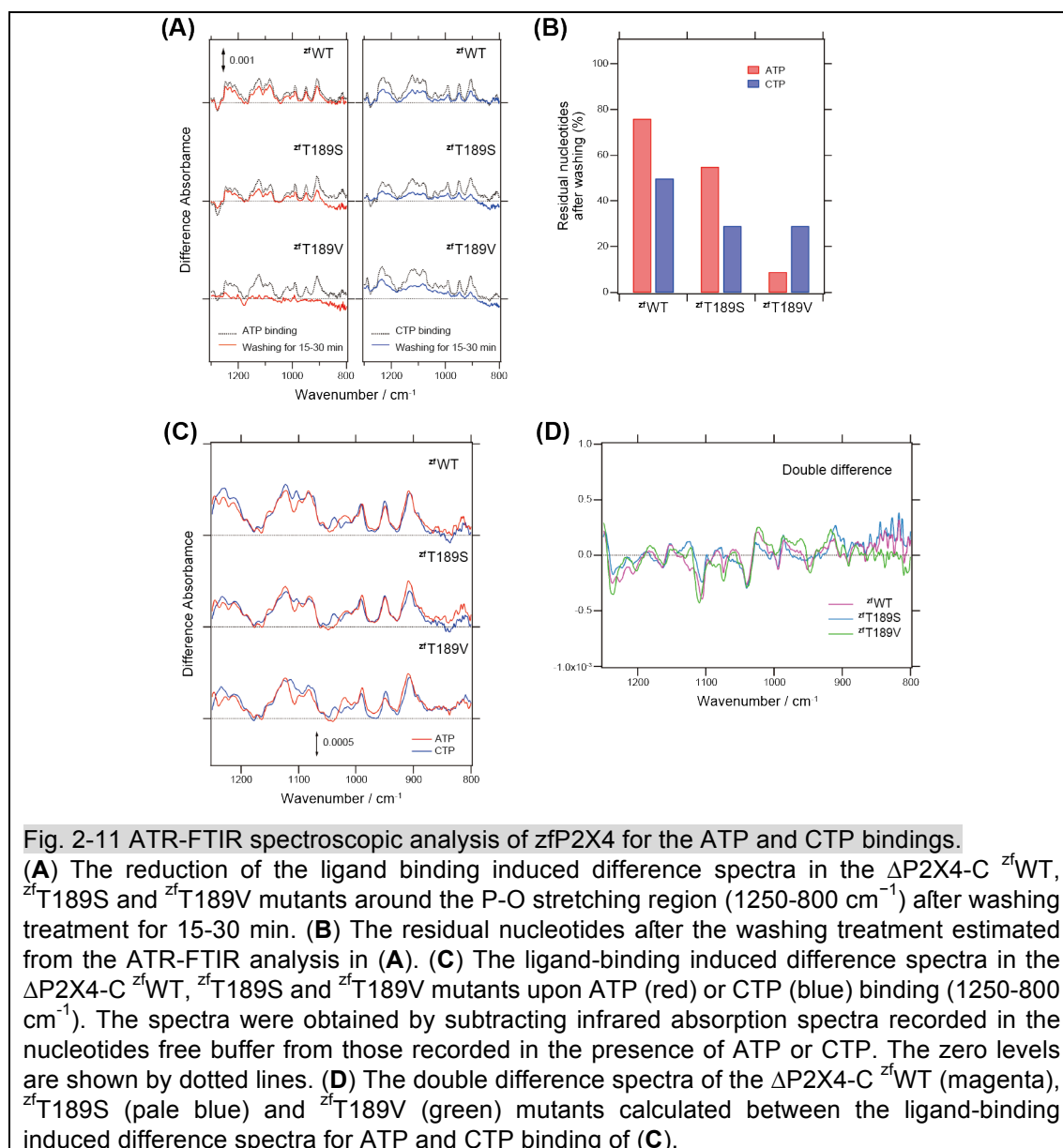


Fig. 2-11 ATR-FTIR spectroscopic analysis of z^f P2X4 for the ATP and CTP bindings.

(A) The reduction of the ligand binding induced difference spectra in the Δ P2X4-C z^f WT, z^f T189S and z^f T189V mutants around the P-O stretching region (1250-800 cm⁻¹) after washing treatment for 15-30 min. **(B)** The residual nucleotides after the washing treatment estimated from the ATR-FTIR analysis in **(A)**. **(C)** The ligand-binding induced difference spectra in the Δ P2X4-C z^f WT, z^f T189S and z^f T189V mutants upon ATP (red) or CTP (blue) binding (1250-800 cm⁻¹). The spectra were obtained by subtracting infrared absorption spectra recorded in the nucleotides free buffer from those recorded in the presence of ATP or CTP. The zero levels are shown by dotted lines. **(D)** The double difference spectra of the Δ P2X4-C z^f WT (magenta), z^f T189S (pale blue) and z^f T189V (green) mutants calculated between the ligand-binding induced difference spectra for ATP and CTP binding of **(C)**.

The positive side corresponds to the nucleotide-bound state and the negative side to the unbound state, respectively. Several positive bands observed in the 1250-850-cm⁻¹ region would be assigned to the P-O stretching modes of a triphosphates group in ATP or CTP as shown in the previous study for small G-protein RAS with GTP⁶⁰. The P-O stretching bands of ATP and CTP are very similar to each other among the z^f WT and conserved threonine mutants (z^f T189S and z^f T189V) (**Fig. 2-11C**). The small spectral changes are confirmed in the double difference spectra calculated from the ATP

and CTP binding-induced spectra as well (**Fig. 2-11D**). Therefore, the triphosphate groups of ATP and CTP are similarly accommodated in the agonist binding site of P2X receptors, which is consistent with the crystal structures (**Fig. 2-6**). Moreover, the spectra in the P-O stretching region are similar among the WT and conserved threonine mutants (^{zf}T189S and ^{zf}T189V), which suggest that the agonist binding site of the triphosphate group is not perturbed by these mutations. Together with the results from the electrophysiological analysis (**Fig. 2-8**), these results might indicate that the ligand binding to P2X receptors is not sufficient for the channel gating. The nucleotide binding affinity of zfP2X4 was analyzed by reduction of the band intensity after washing treatment (**Fig. 2-11A,B**). The reduction of the P-O stretching bands between 1250-800 cm⁻¹ was monitored for ATP (**Fig. 2-11A**). After 15–30 min washing, the residual ATP binding to the ^{zf}WT, ^{zf}T189S, and ^{zf}T189V are ~80%, ~60%, and 10%, respectively (**Fig. 2-11B**), and the values for CTP in the ^{zf}WT, ^{zf}T189S and ^{zf}T189V are ~50%, ~30%, and ~30%, respectively (**Fig. 2-11B**). Therefore, the data showed that the mutation at ^{zf}T189 had more severe effect on the ATP binding than CTP binding, consistent with the ATP-bound and CTP-bound structures (**Fig. 2-6B,D**).

2.6 Discussion in this chapter

In this chapter, the crystal structure of zebrafish P2X4 in complex with CTP, a low-affinity pyrimidine agonist, was determined. Based on the structural information, the electrophysiological and ATR-FTIR spectroscopic analyses were further conducted. The previously determined ATP-bound structure indicated the functional importance of the conserved threonine for the nucleotide base specificity of the P2X receptors, and suggested that the difference in the number of hydrogen bonds between each nucleotide base and the P2X receptors (three for ATP, two for CTP) is responsible for the weaker affinity for CTP over ATP²⁸. These structural and functional analyses not only verified the functional significance of the conserved threonine at the binding site, but also identified a hydrogen bond between the cytosine base and the basic residue in the agonist binding site, which

contributes to CTP binding to the receptor. Accordingly, unlike the previously proposed model, the cytosine base of CTP would be also able to form three hydrogen bonds with the receptor, but possibly with two longer hydrogen bond lengths at the NH₂ site of CTP (**Fig. 2-12A,B**). Therefore, the longer hydrogen bond lengths, rather than the difference in the number of hydrogen bonds, might be mainly responsible for the weaker affinity for CTP over ATP. Furthermore, the CTP-bound structure also facilitated a reevaluation of the superimposed models of other nucleotide triphosphates onto the agonist binding site (**Fig. 2-12C,D**). In the new superimposed models, both GTP and UTP can form only one hydrogen bond between their base rings and the receptor, due to the almost reciprocal hydrogen bonding groups of their base rings, as compared to those of ATP and CTP, respectively (**Fig. 2-12C,D**), confirming the explanation for the inability of GTP and UTP to activate P2X receptors. Overall, our work has revised the previously proposed model for the nucleotide base specificity of P2X receptors, and thus provides new structural insights into the mechanism underlying the nucleotide base specificity. Intriguingly, according to the recent electrophysiological analysis, P2X receptors can be activated by nucleotides other than ATP, such as CTP, at a physiological concentration following an exposure to low concentrations of ATP²¹. Thus, our work might draw more attention to the possible physiological roles of CTP in P2X receptor functions.

Furthermore, P2X receptors have attracted great interest as potential drug targets, and the recent structures of the human P2X₃ receptor in complex with the competitive antagonists³⁴ and the panda P2X₇ receptor in complex with the non-competitive antagonists³⁵. In this report, we revealed the mechanism of pyrimidine base recognition by P2X receptors. Intriguingly, some pyrimidine derivative compounds, such as RO-3, work as P2X antagonists¹³, and pyrimidine derivatives targeting P2X receptors may also interact with the receptors in a similar manner. Accordingly, our work might contribute to the further development of pyrimidine derivative antagonists targeting P2X receptors.

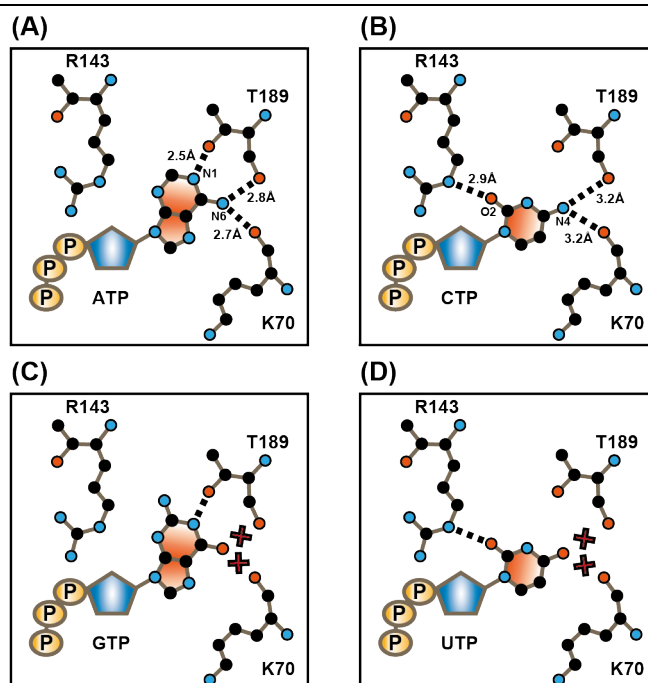


Fig. 2-12 Model for the nucleotide base specificity of P2X receptors.

(A-D) Schematic representations of the interactions between zfp2X4 and ATP (A), CTP (B), GTP (C) or UTP (D). Residues involved in nucleotide base recognition and each nucleoside triphosphate are depicted by stick models. Black dashed lines and numbers indicate hydrogen bond interactions, and red crosses indicate non-complementary hydrogen bond partners, despite reasonable hydrogen bonding distances.

Chapter 3: Structural insight into the divalent cation modulations of P2X receptors

3.1 Introduction

3.1.1 Gating modulation of P2X receptors

Although P2X receptor activation is initiated by ligands exemplified by endogenous ATP, the activation of P2X receptors are further modulated by small molecules or ions³⁸⁻⁴¹. Among these modulators, divalent cations such as Zn^{2+} and Mg^{2+} are important for P2X receptors (**Fig. 1-8**). However, the molecular mechanisms of the divalent cation modulation of the P2X receptors have still proved elusive, due to the lack of structural information for the P2X receptor in complex with divalent cations.

3.1.2 Study purpose

In this study, to reveal the mechanism underlying the divalent cation modulation of P2X receptors, the crystal structure of an invertebrate P2X receptor from the Gulf Coast tick, *Amblyomma maculatum*, was determined in the presence of ATP and divalent cation, Zn^{2+} ion. Furthermore structure-based electrophysiological and computational analyses were conducted.

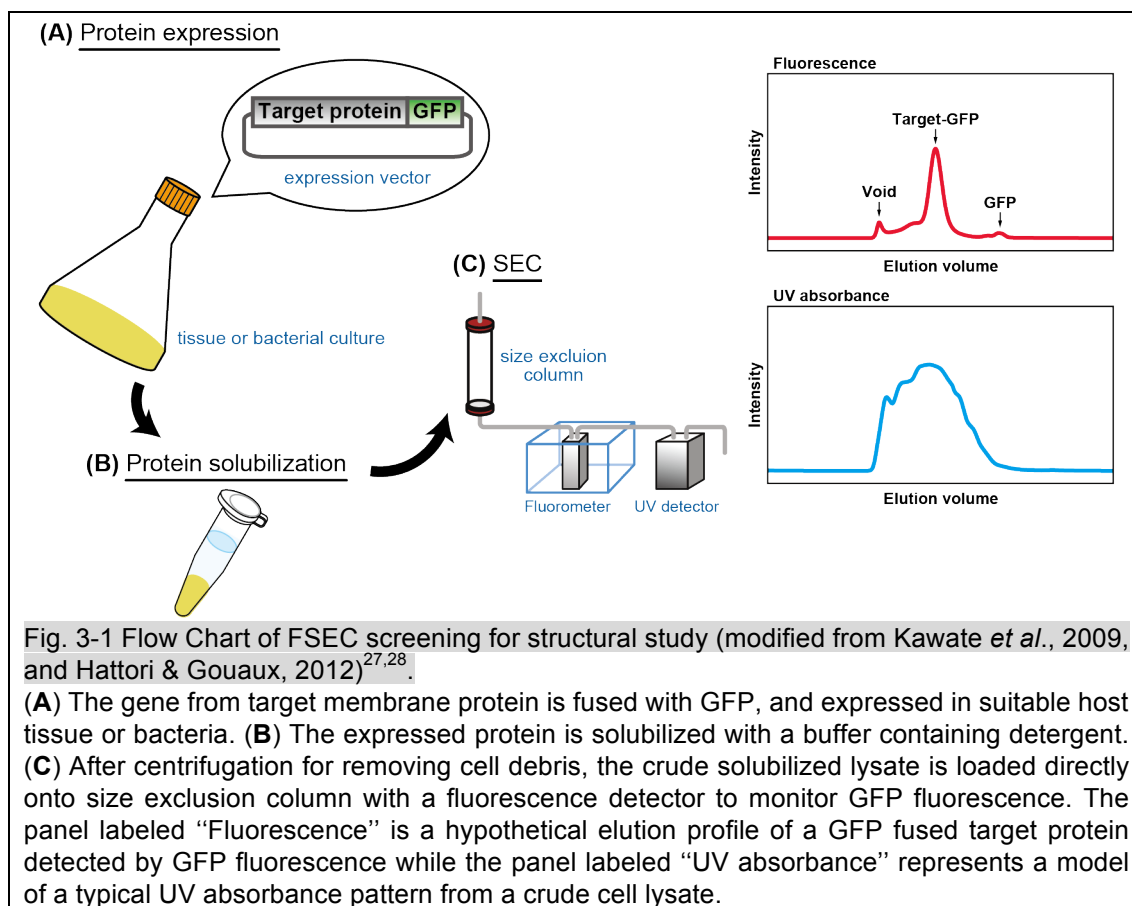
3.2 Functional characterization of *Amblyomma maculatum* P2X (AmP2X) receptor

First, to find out the good candidate of P2X receptors from various species for structural determination, screenings based on the Fluorescence-detection size-exclusion chromatography (FSEC)⁶¹ and FSEC-based thermostability assay (FSEC-TS)²⁵, as well as electrophysiological and biochemical analyses were performed.

3.2.1 Material and methods

3.2.1.1 Fluorescence-detection size-exclusion chromatography (FSEC)

The various genes of P2X receptor orthologs were artificially synthesized (Genscript Co.), and subcloned into pEG BacMam vector, as an N-terminal EGFP fusion with an octa-histidine affinity tag (8xHis-EGFP), and was expressed in HEK293S GnTI⁻ (N-acetylglucosaminyl-transferase I-negative) cells (ATCC, cat. no. CRL-3022)⁶². pEG BacMam, a vector optimized for use in screening assays as well as large-scale and heterologous expressions of target membrane protein, is designed for baculovirus transduction of mammalian cells by inserting a human cytomegalovirus (CMV) promoter just before the multiple cloning site (MCS) onto pFastBac vector (Invitrogen) used in the Bac-to-Bac system. The cells expressing each P2X receptor ortholog was further collected, solubilized and screened by FSEC. In this method, the target membrane protein is cloned into the expression vector with N-terminally or C-terminally fusion of EGFP. Then, the EGFP-fused target membrane protein is expressed in a various host including human and insect cells as well as *Escherichia coli*, solubilized in detergent, and loaded onto a size exclusion column connected with a fluorescence detector to monitor EGFP fluorescence. Then, the peaks from size exclusion chromatogram is evaluated whether the target membrane protein is suitable for structural study by several factors including membrane localization, expression level, the approximate molecular mass, and the degree of monodispersity (**Fig. 3-1**).



As a result of FSEC and FSEC-TS analyses, N-terminally EGFP-fused P2X receptor from the Gulf Coast tick, *Amblyomma maculatum* (AmP2X; NCBI accession number: 346469461), showed a sharp, symmetrical profile, comparable to that of the zFP2X4 receptor with its known crystal structures^{27,28}, indicating that AmP2X is a promising target for structural analysis (**Fig. 3-2A**). The crystallization construct termed AmP2X_{cryst} was further designed by using FSEC method together with previous ΔP2X4-C construct²⁸, as described in the latter section 3.2.2.1.

3.2.1.2 Plasmid construction, RNA preparation and expression of AmP2X receptor

The AmP2X gene codes 383 amino acid length protein. The genes of the AmP2X WT and AmP2X_{cryst} were subcloned into pGEMHE vector in a similar manner of zFP2X4 as described in the section 2.2.1.1. Each RNA from AmP2X WT and AmP2X_{cryst} was synthesized in a similar manner of zFP2X4 as described in the section 2.2.1.2. The synthesized RNA was injected for into *Xenopus*

oocytes. The oocytes were incubated at 18 °C in ND96 Barth's solution supplemented with 50 µg/ml gentamicin, and were used for recording after 4-7 days.

3.2.1.3 Electrophysiological recordings of AmP2X receptor

Electrophysiological recordings of AmP2X WT and AmP2X_{cryst} were performed using same method for zP2X4 described in the section 2.2.1.3. A small amount of divalent cation was needed to suppress the endogenous currents of the oocytes, and 0.5 mM MgCl₂ was sufficient in this experiment. Oocytes were held at -70 mV with a bath-clamp amplifier (OC-725C, Warner) with the direct current gain booster turned on, and the macroscopic currents were recorded and analyzed using pClamp 10 software (Molecular Devices)⁴⁶.

3.2.1.4 Confocal microscopy of AmP2X receptor

The bath solution and setup were the same as that used for the TEVC recordings described in the section 3.2.1.2. The hemagglutinin-tagged, EGFP-fused AmP2X WT and EGFP-fused AmP2X_{cryst} were injected in oocytes in a similar manner as described in the section 3.2.1.2. At 3-4 days after injection, the oocytes were imaged using an FV300 confocal microscope (Olympus) equipped with a320/0.5 numerical aperture objective under TEVC. Images were collected every 30 s for 25 min using the Fluoview software (Olympus). Fluorescence intensity was calculated for each image and plotted against time.

3.2.1.5 Radiolabeled ATP Binding Experiments

The EGFP-fused AmP2X_{cryst} construct was expressed, purified and concentrated as described in the later section, “3.3 Structure determination of the AmP2X receptor in the presence of ATP and Zn²⁺ ion”. The protein samples were dialyzed overnight at 4°C to remove impurities in a dialysis buffer (20 mM HEPES, pH 7.0, 100 mM NaCl, 5% glycerol, and 1 mM DDM), and stored at -80°C before use. Based on the previous ΔP2X4-C experiment²⁸, ATP binding experiments were performed in a 250 µl solution scale by mixing 0.00667 mg/ml EGFP-fused AmP2X_{cryst} protein and various concentration (10-30000 nM) of Hot ATP mix solution, in which radiolabeled ³H-labeled ATP

(Perkin Elmer) was diluted with ATP (Sigma-Aldrich) in a ratio of 1:25. Protein samples were incubated at 4°C overnight and then spotted onto 0.22 μ M nitrocellulose membranes (Millipore) pre-equilibrated with the dialysis buffer. The membranes were washed three times with 1 ml of the dialysis buffer, subsequently transferred to scintillation vials containing 6 ml of Ultima Gold scintillation cocktail (Perkin Elmer) and counted after overnight incubation. Nonspecific binding of protein onto nitrocellulose membranes was estimated by reactions carried out in the presence and absence of 10 mM ATP. The entire experiment was performed in triplicate. Data were fit to a sigmoidal dose-response equation.

3.2.2 Results

3.2.2.1 Screening AmP2X receptor as a suitable candidate for structural study by FSEC

Following the methods in 3.2.1.1, the FSEC screening of various P2X orthologs were performed, and an N-terminally EGFP-fused P2X receptor from the invertebrate Gulf Coast tick, *Amblyomma maculatum*, showed a sharp, symmetrical profile, comparable to that of the zfpP2X4 receptor with its known crystal structures^{27,28}, indicating that AmP2X is a promising target for structural analysis (**Fig. 3-2A**). The crystallization construct of AmP2X, termed AmP2X_{cryst} was further designed by using FSEC method together with previous Δ P2X4-C construct²⁸. The AmP2X_{cryst} construct (Δ N23/ Δ C7/N171Q/C374L) lacks the regions encoding 23 N-terminal and 7 C-terminal residues and includes the two mutations of Asn171 and Cys374. The Asn171 mutation was inserted to exclude putative glycosylation sites, and Cys374 mutation was inserted to remove the free cysteine residue to avoid non-specific disulfide formation. The AmP2X_{cryst} construct also showed a sharp, symmetrical profile similar to the AmP2X WT (**Fig. 3-2A**).

3.2.2.2 Electrophysiological recordings of AmP2X receptor

Following the methods in 3.2.1.3, the TEVC recordings of *Xenopus* oocytes expressing AmP2X WT and AmP2X_{cryst} were performed. The ATP-dependent currents from AmP2X WT were observed revealing that AmP2X functions as an ATP-gated cation channel with fast inactivation, or in other

words, desensitization (**Fig. 3-2B**), while the amino acid sequence of AmP2X is most closely related to that of the slowly desensitizing P2X4 receptor among the mammalian P2X receptors (~40% sequence identity) (**Fig. 3-3**). In addition, a huge current decline occurred in the AmP2X-current amplitude, in response to the second and subsequent ATP applications, even after a 10 min interval (**Fig. 3-2B**). This result shows the strong channel rundown in the AmP2X receptor. Channel rundown has been reported for other P2X receptors, such as P2X1, P2X3, P2X5, and some mutant P2X receptors, as well as for other ligand-gated ion channels^{49,63-66}. It is typically caused by slow recovery from inactivation or channel internalization, as observed in other P2X receptors⁶⁴⁻⁶⁷.

To further investigate this channel property of AmP2X, the simultaneous fluorescent imaging and electrical recordings of *Xenopus* oocytes expressing GFP-fused AmP2X receptors were performed (**Fig. 3-2C**). The results showed that AmP2X WT was expressed at the cell surface and repetitive ATP applications did not induce the internalization of AmP2X (**Fig. 3-2C**), indicating that fast inactivation and slow recovery from inactivation caused the strong channel rundown of AmP2X. In contrast, although AmP2X_{cryst} construct still exhibited ATP binding activity and cell surface expression (**Fig. 3-2E,F**), it did not show ATP dependent gating activity (**Fig. 3-2D**).

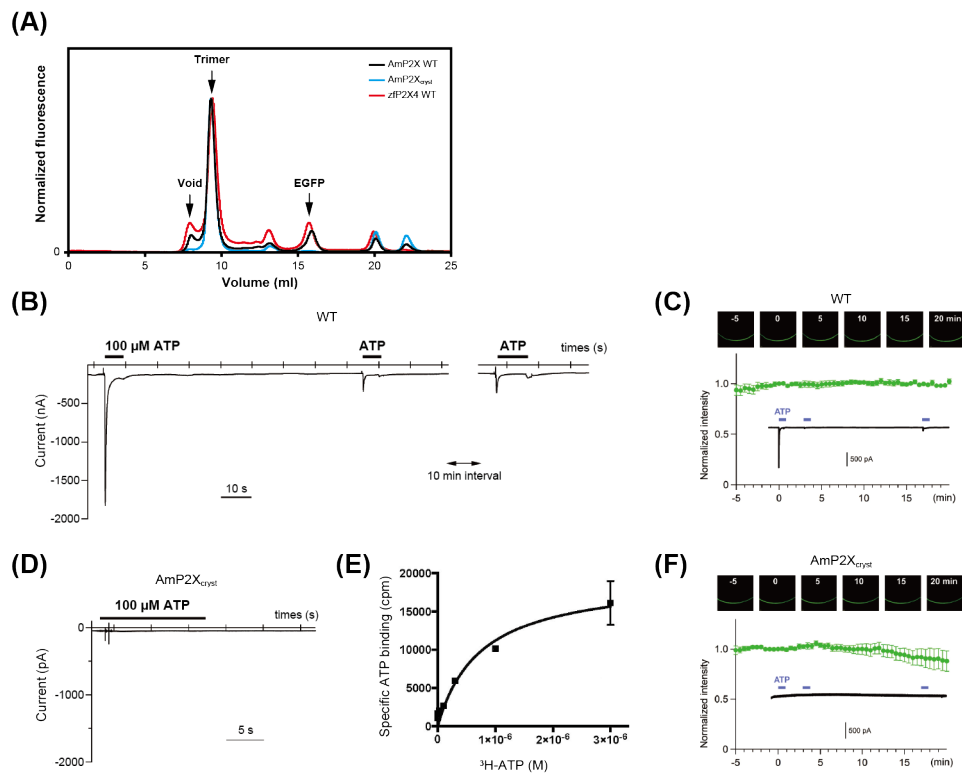


Fig. 3-2 Functional properties of AmP2X and crystallization construct AmP2X_{cryst}.
(A) FSEC profiles on a Superdex 200 10/300 GL column for the EGFP-fused AmP2X WT (black), the EGFP-fused AmP2X_{cryst} (blue), and the EGFP-fused zP2X4 WT (red), expressed in HEK293T cells. The arrows indicate the estimated elution positions of the void volume, the EGFP-fused P2X (trimer), and the free EGFP. **(B)** Representative currents of the AmP2X WT evoked by 100 μM ATP. **(C,F)** The simultaneous imaging and recording of oocytes expressing GFP-tagged AmP2X WT and AmP2X_{cryst}. The timing of the initial ATP (100 μM) application was defined as 0 min. Representative confocal image transitions after the ATP applications are shown. Representative current traces and normalized fluorescence intensities are also shown. Bars depict mean ± S.E.M. (n = 4, respectively). The channel constructs analyzed were WT **(C)** and AmP2X_{cryst} **(F)**. **(D)** Representative current traces of AmP2X_{cryst} with the application of 100 μM ATP, showing no evoked current. **(E)** Measurement of the ATP binding ability of the EGFP-fused AmP2X_{cryst} by a ³H-ATP binding assay. Error bars indicate ±SEM for triplicate samples. The calculated K_d for ³H-ATP binding is 0.745 ± 0.238 μM.

Secondary structure elements from the AmP2X_{cryst} are depicted in cartoon representations and are labeled. Green and cyan triangles indicate the M1 and M2 sites respectively. For the sequence alignment, Gulf Coast tick (amP2X, NCBI accession number: 346469461) and the following vertebrate and invertebrate P2X receptors were used: zebrafish (zfP2X1, 190338175; zfP2X2, 190338247; zfP2X3, 7542524; zfP2X4, 12656589; zfP2X5, 21667664; and zfP2X7, 33520712), human (hP2X1, 4505545; hP2X2, 25092719; hP2X3, 28416925; hP2X4, 116242696; hP2X5, 209572778; hP2X6, 6469324; and hP2X7, 29294631), rat (rP2X1, 1352689; rP2X2, 18093098; rP2X3, 1030065; rP2X4, 1161345; rP2X5, 1279659; rP2X6, 1279661; and rP2X7, 1322005), chicken (ckP2X1, 45383135; ckP2X3, 118091425; ckP2X4, 5918082; ckP2X5, 82217039; and ckP2X7, 513210055), African clawed frog (xpP2X4, 12007266; and xpP2X7, 147899256), sea slug (apP2X, 39578339), freshwater snail (bgP2X, 908479552), soil-dwelling amoeba (ddP2X, 66824047), great pond snail (lsP2X, 410446110), marine green alga (otP2X, 308806021), and blood fluke (smP2X, 51988420). (B) The dendrogram was constructed with TreeView using ClustalW and is shown using MEGA. Invertebrate P2X are colored red. M1 in parentheses (M1) indicates each invertebrate P2X receptor with an M1 site. For the phylogenetic tree, the same vertebrate and invertebrate P2X receptors were used as in (A).

3.3 Structure determination of the AmP2X receptor in the presence of ATP and Zn²⁺ ion

Based on the functional characterization of the invertebrate AmP2X, which indeed functions as ATP-gated cation channel similar to vertebrate P2X receptors, the crystallization of the AmP2X_{cryst} was performed.

3.3.1 Material and methods

3.3.1.1 Plasmid construction of AmP2X receptor for structural determination

As described in the section 3.2.2.1, the AmP2X_{cryst} construct, was subcloned into pEG BacMam vector with an N-terminal EGFP fusion with an octa-histidine affinity (8xHis-EGFP) tag, and following a tobacco etch virus (TEV) cleavage site.

3.3.1.2 Baculovirus preparation of the crystallization construct AmP2X_{cryst}

The baculovirus was prepared following the Bac-to-Bac system protocol (Invitrogen), as described in the section 2.3.1.2.

3.3.1.3 Expression and purification of the AmP2X_{cryst}

The AmP2X_{cryst} construct was expressed by adding 10% P2 virus stock and 10 mM sodium butyrate to HEK293S GnTI⁻ cells (3.0 x 10⁶ cells/ml, 1L), and by incubating at 37°C in 16-18 hr and

following at 30°C in 2 days. Cell collection and disruption, as well as membrane isolation were performed as described in the section 2.3.1.3. The membrane fraction was solubilized for 1 h at 4°C in a buffer (50 mM Tris, pH 8.0, 150 mM NaCl, 5% glycerol, 40 mM DDM (Calbiochem)). The detergent-soluble fraction was incubated with Talon metal affinity resin (Clontech), washed with 20 mM imidazole and eluted with 250 mM imidazole. After TEV protease digestion and Endo H treatment, to remove the 8xHis-EGFP tag and part of the N glycans, the protein was isolated by size-exclusion chromatography on a Superdex 200 10/300 GL column (GE Healthcare) in size-exclusion chromatography buffer (20 mM HEPES, pH 7.0, 100 mM NaCl, 5 mM n-decyl- β -D-maltopyranoside (DM) (Anatrace)) (**Fig. 3-4A**). The peak fractions of the protein were collected and concentrated to 2 mg/ml using a centrifugal filter device (Millipore, 50 kDa molecular weight cut off)

3.3.1.4 Crystallization of the Amp2X_{cryst}

Before crystallization, 1 mM ATP was added to the protein solutions and incubated at 4°C 1 hr. The crystals were grown at 4°C with mixtures of 1:1 or 2:1 (v/v) ratios of protein and reservoir solutions by the vapor diffusion method. The crystals of Amp2X_{cryst} appeared in the reservoir solutions (8-11% (w/v) PEG 8000, 50 mM Zinc acetate, and 0.05 M MES, pH 6.0) (**Fig. 3-4B**). The crystals were harvested and cryoprotected, in a solution (10% PEG 8000, 50 mM Zinc acetate, and 0.05 M MES, pH 6.0, 25% glycerol, 0.5 mM DDM and 1 mM ATP). Crystals were flash-frozen in liquid nitrogen for X-ray diffraction experiments.

3.3.1.5 Data collection and structure determination

The X-ray diffraction data were collected at 100K on the SPring-8 beamline BL41XU. Diffraction data were processed using HKL2000 (HKL Research Inc.) (**Fig. 3-4C**). The structure of Amp2X_{cryst} was obtained by molecular replacement with Phaser⁵², using the ATP-bound Δ P2X4-C structure (PDB ID: 4DW1) as the template. The determined structure was further refined by using the programs PHENIX⁵³ and COOT⁵⁴. Crystallographic data and refinement statistics are presented in

the figure (Fig. 3-4D). The coordinate of the ATP-bound $\text{AmP2X}_{\text{cryst}}$ structure was deposited on Protein Data Bank (PDB) under the accession code 5F1C.

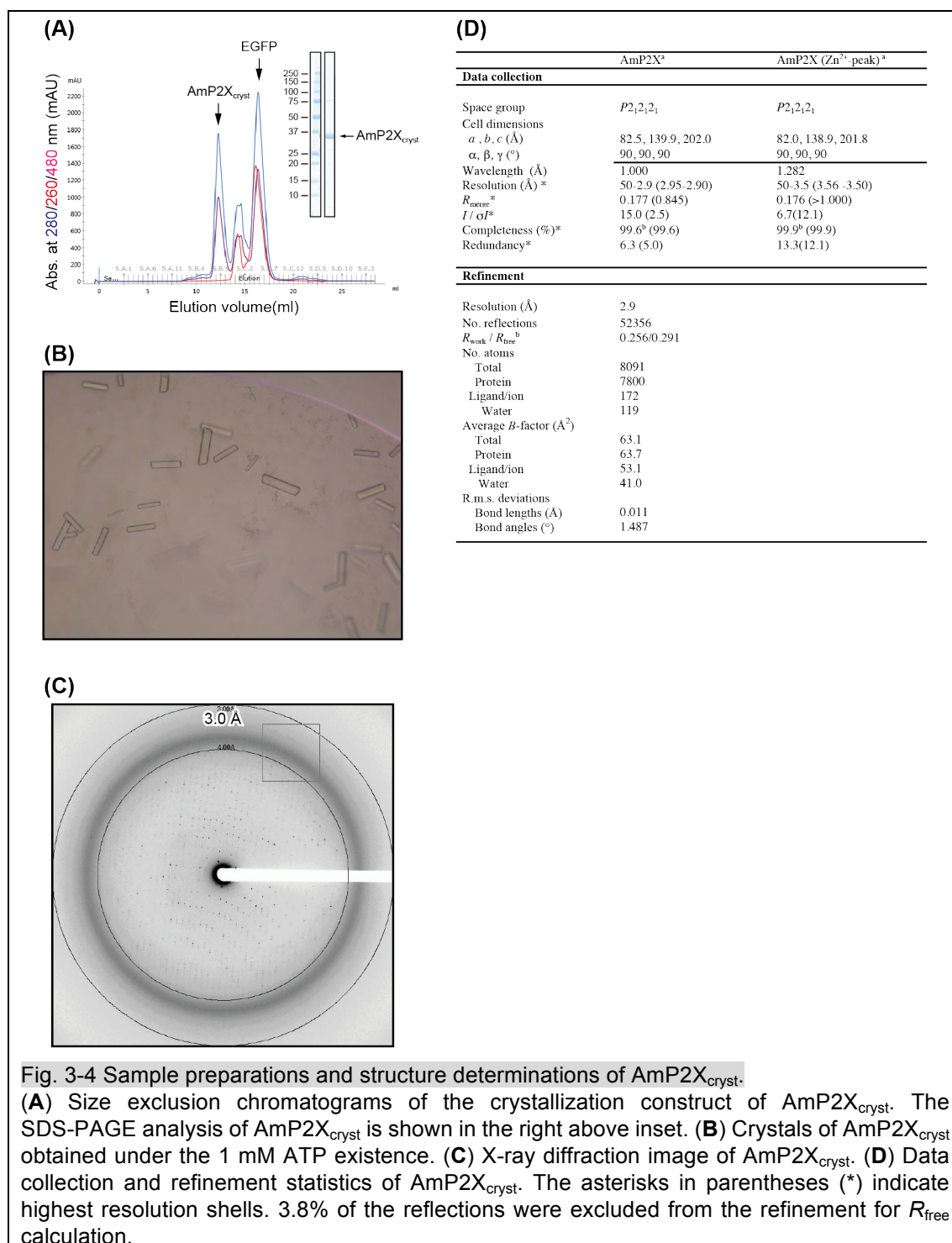


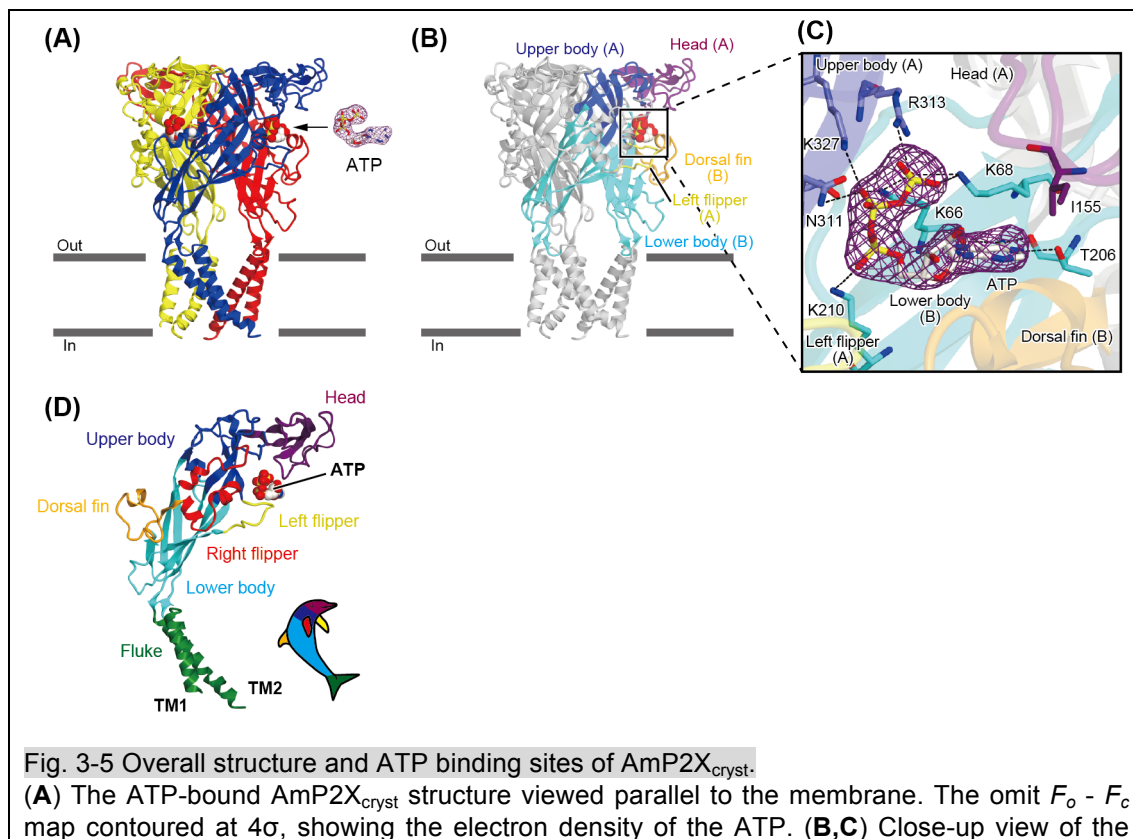
Fig. 3-4 Sample preparations and structure determinations of $\text{AmP2X}_{\text{cryst}}$.

(A) Size exclusion chromatograms of the crystallization construct of $\text{AmP2X}_{\text{cryst}}$. The SDS-PAGE analysis of $\text{AmP2X}_{\text{cryst}}$ is shown in the right above inset. **(B)** Crystals of $\text{AmP2X}_{\text{cryst}}$ obtained under the 1 mM ATP existence. **(C)** X-ray diffraction image of $\text{AmP2X}_{\text{cryst}}$. **(D)** Data collection and refinement statistics of $\text{AmP2X}_{\text{cryst}}$. The asterisks in parentheses (*) indicate highest resolution shells. 3.8% of the reflections were excluded from the refinement for R_{free} calculation.

3.3.2 Results

3.3.2.1 Overall structure of the $\text{AmP2X}_{\text{cryst}}$

The X-ray diffraction data of Amp2X_{cryst} crystal were collected to 2.9 Å resolution, successfully led to determine the structure (**Fig. 3-4**). Amp2X_{cryst} adopts a chalice-like trimeric architecture, and each subunit of Amp2X_{cryst} consists of a large extracellular domain and two transmembrane helices resembling the shape of a dolphin, as observed in the zfp2X4 structure (**Fig. 3-5A-D**)^{27,28}. We observed strong electron density peaks corresponding to ATP molecules at each subunit interface of the extracellular domain (**Fig. 3-5C**), consistent with the crystallization conditions containing 1 mM ATP and the ATP binding activity of the Amp2X_{cryst} construct (**Fig. 3-2E**). The ATP molecules adopt a bent conformation and form tight interactions with the receptor (**Fig. 3-5C**). The phosphate groups are recognized by the side chains of Lys66, Lys68, and Lys210 from one subunit and Asn311, Arg313, and Lys327 from the neighboring subunit, whereas the adenine ring of ATP forms hydrogen bonds with the side chain of Thr206 and the main chain carbonyl atoms of Lys66 and Thr206 (**Fig. 3-5C**). All of these hydrophilic residues are highly conserved among P2X receptors (**Fig. 3-3**) and are important for their ATP-dependent gating activities^{51,68–73}.



ATP binding site in the ATP-bound Amp2X_{cryst}. The amino acid residues and ATP are depicted by stick models. The molecule is colored according to the dolphin-like model. Dotted black lines in (C) indicate hydrogen bonds (<3.3 Å). (D) A subunit of the ATP-bound Amp2X_{cryst}, colored according to the previously proposed dolphin-like model. The sequence comparison with zfp2X4 defined the domains of Amp2X_{cryst} as Fluke (Leu30-Lys51, and Ser345-Leu372), Lower body (Gly52-Val70, Val101-Phe111, Phe205-Asn224, Gly271-Arg298, and Thr332-Leu344), Upper body (Val71-Ile100, Val112-Ser121, Pro184-Pro191, and Trp310-Ile331), Head (Gln122-Cys183), Right flipper (Leu192-Asn204, and Ile252-Gly270), Left flipper (Leu299-Gly309), and Dorsal fin (Leu225-Arg251) respectively.

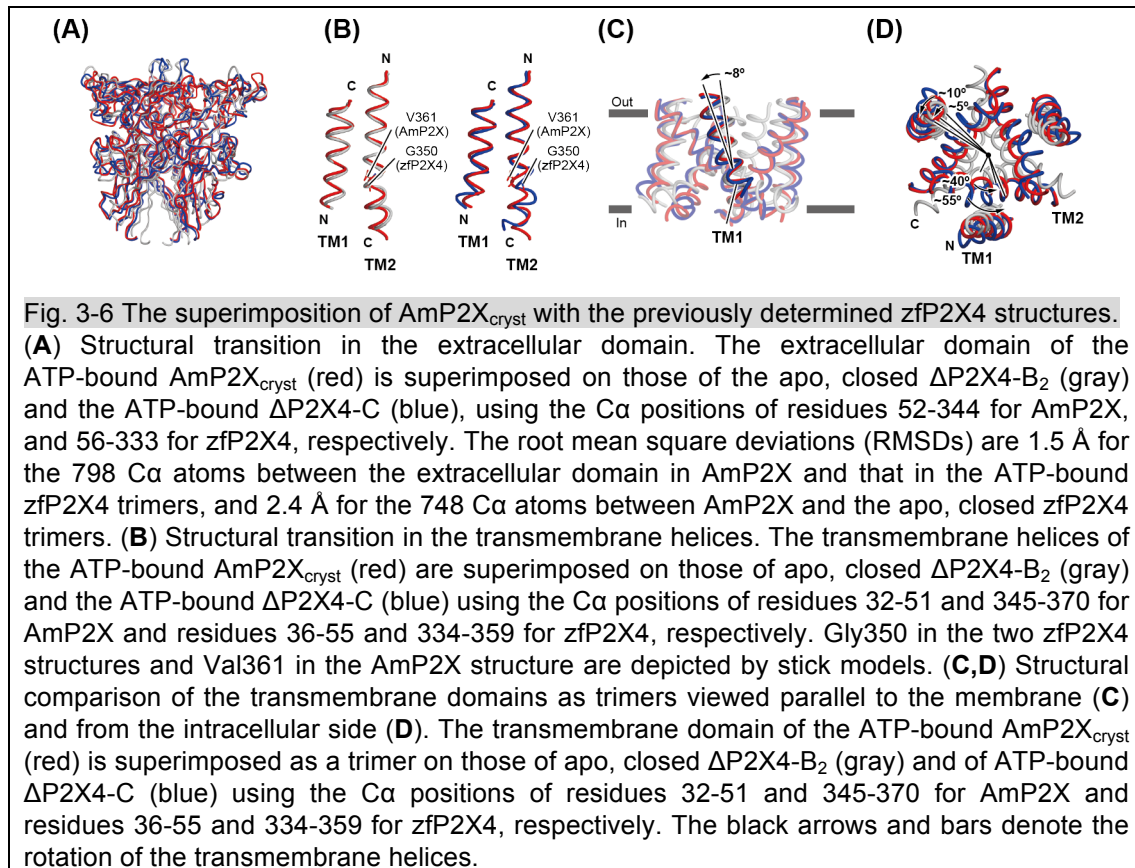
3.3.2.2 Comparison with the apo, closed and ATP-bound open zfp2X4 receptors

While the extracellular domain structure of Amp2X_{cryst} resembles that of the ATP-bound, open zfp2X4, rather than that of apo, closed zfp2X4 (**Fig. 3-6A**), the transmembrane domain of Amp2X_{cryst} exhibits a unique feature. The root-mean-square deviations (RMSDs) for the 138 Cα atoms from the transmembrane domain of the trimer are 2.2 Å between Amp2X and ATP-bound zfp2X4 and 4.9 Å between Amp2X and apo, closed zfp2X4 (**Figs. 3-6C,D and 3-7A-C**). Thus, the structure of the transmembrane domain of the Amp2X trimer is closer to that of ATP-bound, open zfp2X4 (**Figs. 3-6C,D and 3-7A-C**). In contrast, the transmembrane domain of each Amp2X monomer resembles that of the apo, closed state of zfp2X4 (**Figs. 3-6B and 3-7J-L**). The RMSDs for the 46 Cα atoms from the transmembrane domain of each monomer are 2.1 Å between Amp2X and ATP-bound zfp2X4 and 1.7 Å between Amp2X and apo, closed zfp2X4.

The superimposition of the transmembrane architecture of Amp2X_{cryst} with those of the previously determined zfp2X4 structures revealed further details about their structural differences. Consistent with the ATP-dependent expansion of the extracellular domain, the TM1 and TM2 helices in the Amp2X_{cryst} structure are rotated by ~5 and ~40 degrees counterclockwise around the pore-center axis, relative to the closed state, whereas those in the ATP-bound zfp2X4 are rotated by ~10 and ~55 degrees counterclockwise around the pore-center axis, respectively (**Fig. 3-6D**). These movements induce an iris-like expansion of the transmembrane helices by ~3Å to form a pore (**Fig. 3-7A-C**). Consistent with the smaller rotation angles, the pore size at the constriction region is smaller in the Amp2X_{cryst} structure (**Fig. 3-7D-I**). The TM2 helices are totally straight in the Amp2X_{cryst} structure, which restricts the wide pore formation (**Fig. 3-7B,E,H,K**), while the kink of transmembrane helix 2

(TM2) at the highly conserved Gly350 residue in zfP2X4 enables the TM2 helices to form the larger pore (**Fig. 3-7C,F,I,L**). In AmP2X, the residue corresponding to Gly350 in zfP2X4 is replaced by valine as V361 (**Fig. 3-3A**). Overall, the ion-conducting pore is partially opened in the AmP2X_{cryst} structure with the straight TM2 helices.

Because the ion-conducting pore is partially opened, the present structure of AmP2X_{cryst} might reflect either a pre-open state before channel opening or an inactivated state after channel opening. Considering the loss of the channel gating activity and the structural features, including the activated extracellular domain (**Figs. 3-2E and 3-6A**), the structure more likely represents the pre-open state, in which an ATP-induced conformational change in the extracellular cellular domain is partially propagated to the transmembrane domain.



Furthermore, it was proposed that the transmembrane architecture of the previously determined ATP-bound structure of the zfP2X4 trimer, including the large inter-subunit gaps, is partially distorted from that in the membrane-embedded native state³¹. Because the trimeric architecture of

AmP2X_{cryst} resembles that of the ATP-bound structure of zfP2X4 (Fig. 3-7E,F), similar inter-subunit gaps are observed in the transmembrane region of the trimeric AmP2X_{cryst} structure (Fig. 3-7E). Accordingly, we do not exclude the possibility that the trimer formation of the transmembrane domain in the AmP2X_{cryst} structure is also partially distorted, possibly because of detergents or truncations employed for crystallization.

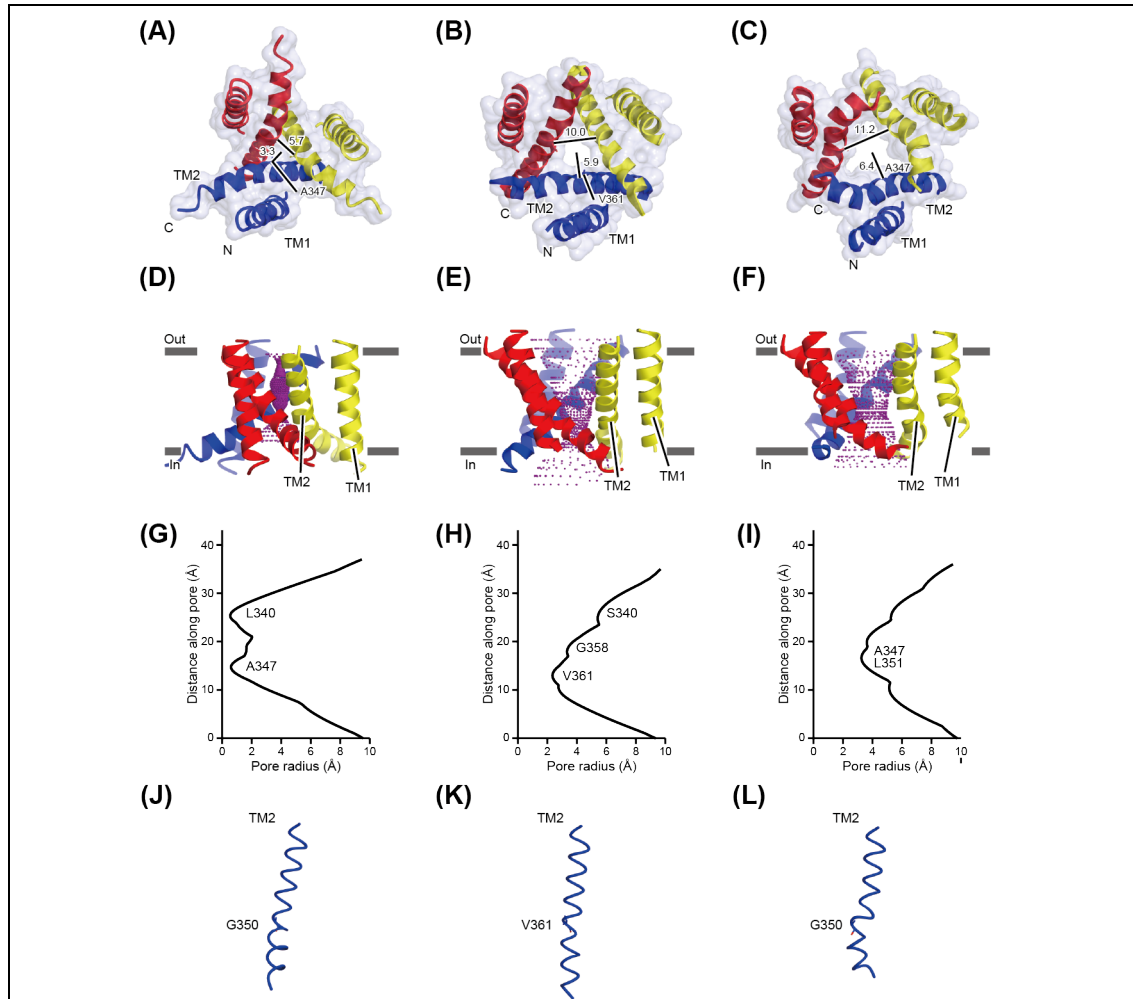


Fig. 3-7 Structural Comparisons of the Transmembrane Domains.

(A-C) The transmembrane domains of apo, closed Δ P2X4-B₂ (A); ATP-bound AmP2X_{cryst} (B); and ATP-bound Δ P2X4-C (C) viewed from the intracellular side. A surface model with a cartoon representation is shown for each structure. Amino acid residues involved in the pore constriction region are depicted by stick models. In (A) and (C), the distances between the C α position of Ala347 and the center of the pore are shown by black lines and numbers (angstroms). In (B), the distances between the C α position of Val361 and the center of the pore are shown by black lines and numbers (angstroms). (D-F) Close-up views of the pore domain in apo, closed Δ P2X4-B₂ (D); ATP-bound AmP2X_{cryst} (E); and ATP-bound Δ P2X4-C (F) viewed parallel to the membrane. (G-I) Pore radii for apo, closed Δ P2X4-B₂ (G); ATP-bound AmP2X_{cryst} (H); and ATP-bound Δ P2X4-C (I) along the pore center axis. (J-L) Close-up views of the TM2 helices in apo, closed Δ P2X4-B₂ (J); ATP-bound AmP2X_{cryst} (K);

and ATP-bound $\Delta P2X4$ -C (L). Amino acid residues involved in the pore constriction region are depicted by stick models.

3.3.2.3 Zn^{2+} binding site

In the ATP-bound $AmP2X_{cryst}$ structure crystallized in the presence of Zn^{2+} ion, strong residual electron densities at two distant sites in the extracellular domain were observed (**Fig. 3-8A**). The anomalous difference Fourier map clearly showed that these densities correspond to Zn^{2+} ions (**Fig. 3-8B-D**). Accordingly, two distinct metal binding sites (termed M1 and M2 sites) in the extracellular domain of $AmP2X_{cryst}$ were identified. The M1 site is located at the trimer interface at the top part of the upper body domain of the dolphin model, in other words, the central chamber region (**Fig. 3-8A**), and is coordinated by the side chains of Glu105 in one subunit and Glu106 in the neighboring subunit (**Fig. 3-8C-D**). Among the P2X4 receptors, the corresponding residues at the M1 site are strictly conserved as Gln and Glu residues, respectively (**Fig. 3-3A**). The M2 site is coupled with the ATP binding site, and is surrounded by the side chain of Asp188 and the γ -phosphate group of ATP, to bridge the receptor and ATP molecules (**Fig. 3-8B**). Asp188 is strictly conserved among the P2X1 and P2X3 receptors (**Fig. 3-3A**).

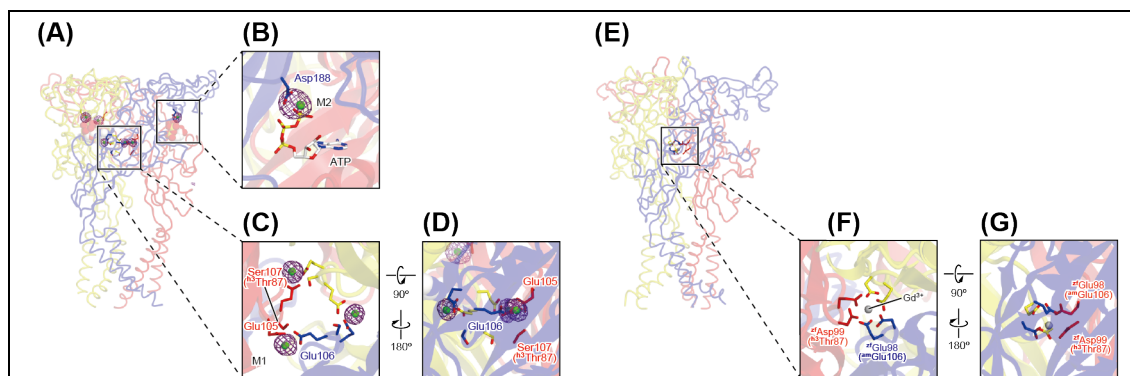


Fig. 3-8 Metal Binding Sites of AmP2X and of apo, Closed zfP2X4.

(A) Overall view of the zinc binding sites in the AmP2X structure. The omit $F_o - F_c$ map contoured at 6σ , showing the electron densities of the zinc ions. (B-D) Close-up views of the zinc binding sites. The anomalous difference Fourier maps contoured at 4σ , showing the electron densities of the zinc ions. (E) Overall view of the gadolinium binding site in the apo, closed zfP2X4 structure (PDB ID: 3H9V). (F,G) Close-up view of the gadolinium binding site. The superscripts “zf,” “am,” and “h3” refer to zfP2X4, AmP2X, and human P2X3, respectively. The amino acid residues ^{zf}Glu98 and ^{zf}Asp99 correspond to ^{am}Glu106 and ^{am}Ser107 (^{h3}Thr87), respectively.

3.4 Mutation assay of the metal binding sites by electrophysiology

To further investigate the functional roles of these metal binding sites, the electrophysiological analysis of Zn^{2+} potentiation was performed using *Xenopus* oocytes. Because a huge current decline occurred in the Amp2X-current amplitudes, in response to the second and subsequent ATP applications (**Fig. 3-2B**), Amp2X would not be suitable to analyze the Zn^{2+} potentiation by repetitive ATP applications. Therefore, rat P2X4, which has well-established electrophysiological properties, including Zn^{2+} potentiation, was employed^{39,42}.

3.4.1 Material and methods

3.4.1.1 Plasmid construction, RNA preparation and expression of rP2X4 receptor

The RNAs from rat P2X4 (rP2X4) WT and mutants, which are subcloned into pGEMHE vector, were synthesized in a similar manner of zfP2X4 as described in the section 2.4.1.1. The RNA injected oocytes were incubated at 18°C in ND96 Barth's solution supplemented with 50 µg/ml gentamicin, and were used for recording after 2–3 days.

3.4.1.2 Electrophysiological recordings of rP2X4 receptor

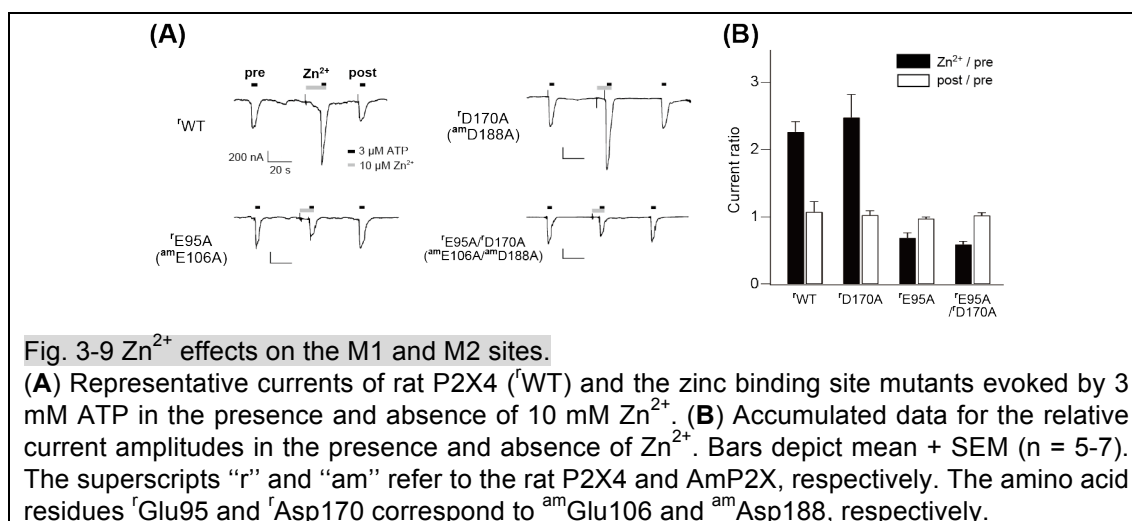
Electrophysiological recordings of rP2X4 WT and mutants were performed using a similar method as described in the section 2.4.1.2. In the recordings analyzing Zn^{2+} effect, the ratios of the current amplitudes in the presence or absence of ZnCl_2 to the amplitude before Zn^{2+} application were analyzed. In the recordings analyzing Gd^{3+} effect, a dataset from an identical oocyte was used for the analysis of the half-maximal inhibitory concentration value for GdCl_3 .

3.4.2 Results

3.4.2.1 Mutation effects of metal binding site residues on Zn^{2+} ion

To assess the functional role of M1 and M2 sites, the mutants (^rE95A, ^rD170A, and ^rE95A/^rD170A) of ^rGlu95 and ^rAsp170 for the equivalent residues in rat P2X4, corresponding to Glu106 in the M1 site and Asp188 in the M2 site of Amp2X were created (the superscript ‘r’ refers to rat P2X4). The mutation at the M1 site (^rE95A) abolished the potentiation effect of Zn^{2+} ion (**Fig. 3-9**), whereas the

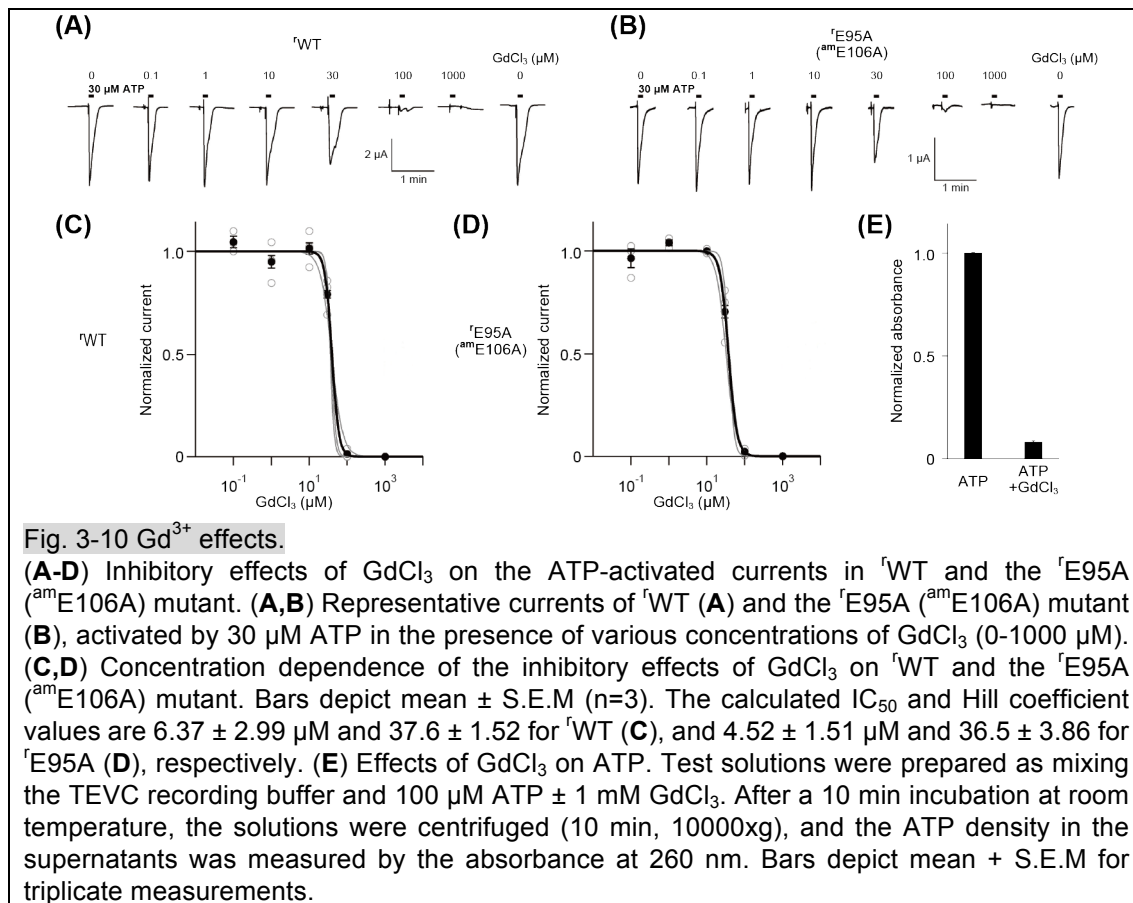
mutation at the M2 site (^rD170A) did not affect the Zn²⁺ potentiation of the ATP-dependent currents (**Fig. 3-9**). Glu105 and Glu106 at the M1 site in AmP2X are conserved as similar residues, Gln and Glu, respectively, among P2X4 receptors and some invertebrate P2X receptors (**Fig. 3-3A**). The Gln and Glu pair in the M1 site of these receptors would also provide chemically favorable conditions for Zn²⁺ binding, as observed in the AmP2X structure (**Fig. 3-8C,D**). Consistently, our electrophysiological analysis revealed that the M1 site is responsible for the Zn²⁺ potentiation of the rat P2X4 receptor (**Fig. 3-9**). Furthermore, an invertebrate P2X receptor, LsP2X from the great pond snail, *Lymnaea stagnalis*, which possesses the M1 site (**Fig. 3-3A**), is also reportedly potentiated by Zn²⁺ ion¹⁷. Overall, these results suggest the functional role of the M1 site in zinc potentiation for the P2X4 receptors and the invertebrate P2X receptors possessing the M1 site.



3.4.2.2 Mutation effects of metal binding site residues on Gd³⁺ ion

The M1 site is overlapped with or neighboring the previously identified metal binding sites for Gd³⁺ and Mg²⁺ in the central chamber region, which are implicated in the inhibition of P2X receptors (**Fig. 3-8E-G**)^{41,74}. The M1 site shares some residues (^rGlu95 in rat P2X4) with the Gd³⁺ binding site (^{zf}Glu98 in zfP2X4) identified in the previously determined zfP2X4 structure in the apo, closed state (**Fig. 3-8E-G**)²⁷. The application of Gd³⁺ inhibited the ATP-dependent activation of zfP2X4. Accordingly, the Gd³⁺ binding site seemed to play an important role in Gd³⁺ modulation²⁷. However, we found that the mutation of ^rGlu95 did not abolish the Gd³⁺-dependent inhibition (**Fig. 3-10A-D**).

The addition of 1 mM Gd^{3+} ion to a 100 mM ATP solution totally depleted the ATP because of precipitation (**Fig. 3-8E**). Furthermore, the values of the Hill coefficients were out of order (about <35), suggesting that GdCl_3 does not affect the specific binding reaction between the ATP and the P2X receptor. Therefore, the depletion of ATP by Gd^{3+} addition, rather than the Gd^{3+} binding to the receptors, could be mainly responsible for the inhibitory effect of Gd^{3+} on the ATP-dependent activation of P2X receptors.



More importantly, the Thr87 residue in the human P2X3 receptor, corresponding to Ser107 in AmP2X and Asp99 in zfP2X4 (**Fig. 3-8F,G**), is implicated in the Mg^{2+} -dependent inhibition⁴¹. The Thr87 residue is located within the central chamber region and neighbors the M1 site and the Gd^{3+} binding site (**Fig. 3-8A,C-G**). Accordingly, the central chamber region in the extracellular domain may provide multiple cation binding sites for both potentiation and inhibition in P2X receptors.

3.5 Zn²⁺ modulation mechanism revealed by molecular dynamics simulations

To investigate how Zn²⁺ ion at the M1 site modulates channel gating, all-atom molecular dynamics (MD) simulations of the ATP-bound Amp2X_{cryst} in the presence and absence of Zn²⁺ at the M1 site was performed.

3.5.1 Material and methods

3.5.1.1 System construction of molecular dynamics simulation

The simulation system included the Amp2X_{cryst} trimer, 1-palmitoyl-2-oleoyl-phosphatidylcholine (POPC), ATP, Zn²⁺ ions, water molecules, and 150 mM NaCl. The missing atoms, including hydrogens in the protein, were added with the program VMD⁷⁵. The periodic boundary system, including the explicit solvent and the POPC lipid bilayer, was prepared. The size of the simulation box was 128 × 128 × 148 Å. The net charge of the system was neutralized by adding chloride and sodium ions. The topologies and force field parameters from CHARMM36 were used⁷⁶. MD simulations were performed with the program NAMD 2.9 (ref. 77). The system was first energy minimized for 1000 steps with fixed positions for the non-hydrogen atoms and then for another 1000 steps with 10 kcal/mol restraints for the non-hydrogen atoms. Next, we performed an equilibration run for 0.5 ns in the NVT ensemble (310 K, 128 × 128 × 148 Å volume) with 10 kcal/mol restraints for protein non-hydrogen atoms, ATP, and Zn²⁺, followed by an equilibration run for 1.0 ns in the NPT ensemble (310 K, 1 atm), with the same restraints. Finally, equilibration runs were performed for 1.0 ns in the NPT ensemble, with the bond length restraints between Zn²⁺ ions or ATP and the protein side chain: (1) ATP N1 and Thr206 OG1, (2) M2 and ATP OG1, (3) M1 and Glu105, (4) M1 and Glu106, and (5) M2 and Asp188 of the adjacent chain. These restrained bond lengths are based on those observed in the crystal structure of Amp2X_{cryst}. The production process was performed for 150 ns, with the same bond length restraints. Constant temperature was maintained by using Langevin dynamics. Constant pressure was maintained by using the Langevin piston Nose-Hoover

method⁷⁸. Long-range electrostatic interactions were calculated using the particle mesh Ewald method⁷⁹.

3.5.2 Results

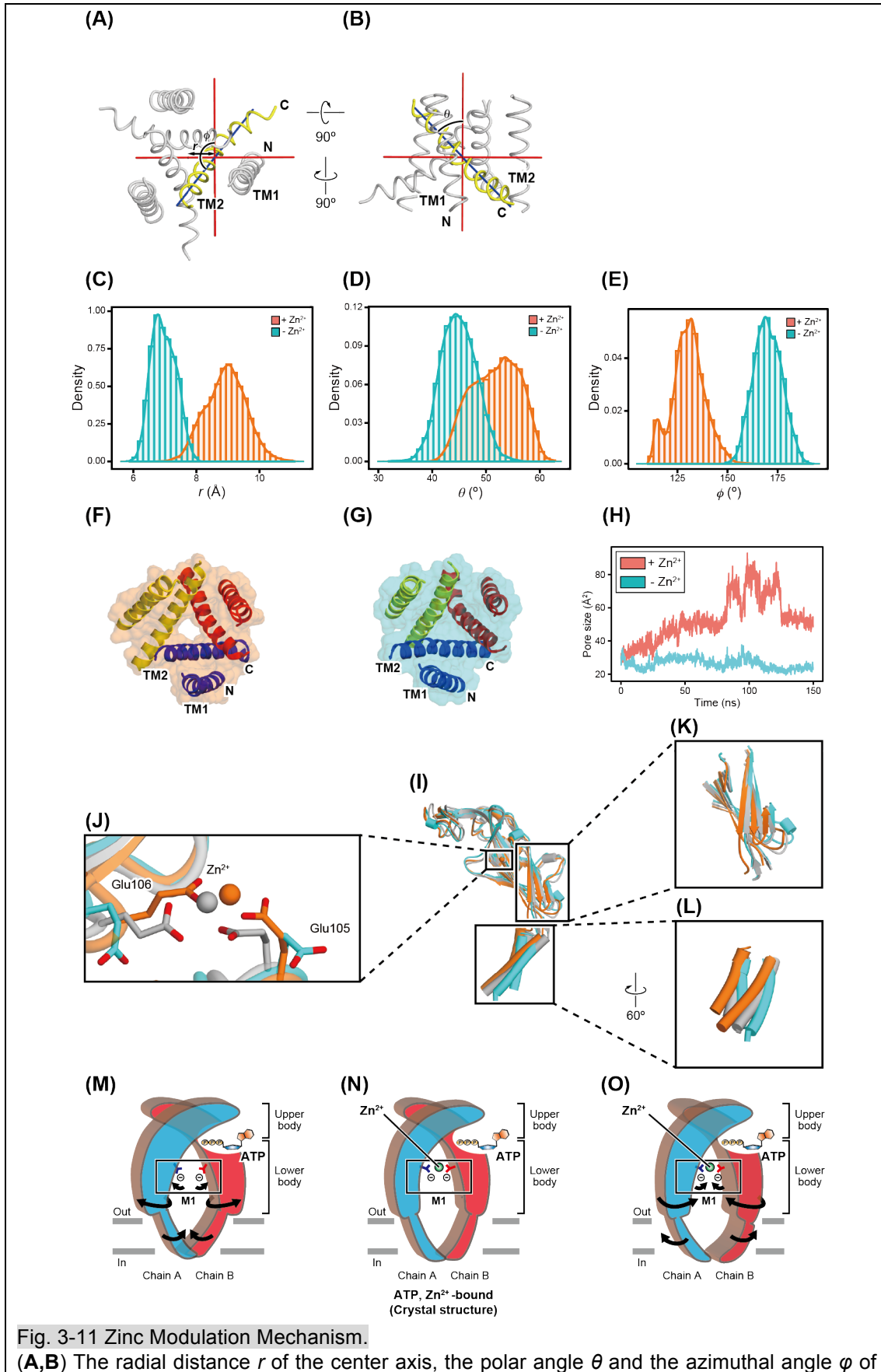
3.5.2.1 Zn^{2+} effect on the M1 site

To analyze the initial early events upon zinc binding in the zinc potentiation of P2X receptors, the MD simulations were performed for 150 ns. The radial distance r of the center axis, and the polar angle θ and the azimuthal angle φ of the helical axis were calculated to quantitatively estimate the structural change in the transmembrane region (**Fig. 3-11A,B**)⁸⁰. The results of the MD simulations revealed higher radial distance r and greater polar angle θ in the presence of Zn^{2+} ion (**Fig. 3-11C-E**), indicating that Zn^{2+} binding at the M1 site promotes channel opening (**Fig. 3-11F-H**). A further structural comparison of the extracellular domain revealed how Zn^{2+} binding to the extracellular domain facilitates channel opening in the transmembrane domain. First, Zn^{2+} binding to the M1 site brings two glutamate residues, Glu105 from one subunit and Glu106 from the neighboring subunit, toward each other by electrostatic attraction (**Fig. 3-11I,J,O**). This attraction induces the small counterclockwise rotation of the lower body domain by ~ 2 degrees (**Fig. 3-11K**), whereas the side chains of the residues are turned away from each other in the absence of Zn^{2+} (**Fig. 3-13I,J,M**). The Zn^{2+} -dependent small structural change within the upper lower body is magnified into the larger movement in the lower part of the body domain, which is directly connected to the transmembrane domain. Accordingly, the transmembrane domain is rotated counterclockwise by ~ 10 degrees to open the pore (**Fig. 3-13L,O**).

Zn^{2+} potentiation has also been reported for the P2X2 receptors⁸¹. Two histidine residues, His120 and His213, in the rat P2X2 receptor are involved in the zinc potentiation^{82,83} and are located at the head and dorsal fin domains forming the ATP binding cleft (**Figs. 3-3A and 3-5B,D**), whereas these histidine residues are not conserved among the P2X4 receptors (**Fig. 3-3A**). The ATP binding causes the cleft closure motion in the ATP binding pocket, which in turn induces the structural change of

the body domain for pore opening^{28,84}. Accordingly, Zn^{2+} binding to these histidine residues bridges the inter-subunit cleft within the ATP binding pocket to facilitate channel activation⁸⁴. In contrast, the M1 site is located far from the ATP binding pocket (**Fig. 3-8A,C,D**), and Zn^{2+} binding to the M1 site would be directly coupled to the structural change of the body domain for pore opening (**Fig. 3-11**). Therefore, the molecular mechanism of Zn^{2+} potentiation in P2X2 receptors is distinct from that in P2X4 receptors.

Taken together, these results from molecular dynamics simulations show that allosteric Zn^{2+} binding to the M1 site facilitates the ATP-dependent structural change of the body domain in the extracellular region for pore opening.



the helical axis are shown in the transmembrane domains of the apo, closed zfp2X4 structure. One TM2 helix from a subunit is colored yellow, and the other helices are colored gray. (C-E) Distributions of r (C), θ (D), and φ (E) are displayed. Orange distributions indicate the results of the MD simulations in the presence of Zn^{2+} at the M1 site, and cyan distributions indicate the results of the MD simulations in the absence of Zn^{2+} at the M1 site. (F,G) The transmembrane domain of ATP-bound Amp2X_{cryst} after the 150 ns MD simulations in the presence of Zn^{2+} at the M1 site (F) and in the absence of Zn^{2+} at the M1 site (G). Each structure is viewed from the extracellular side. A surface model containing the cartoon representation is shown for each structure. (H) The time course of the pore sizes of ATP-bound Amp2X_{cryst} through the 150 ns MD simulations. The orange graph shows the results of the simulations in the presence of Zn^{2+} at the M1 site, and the cyan graph shows the results of the simulations in the absence of Zn^{2+} at the M1 site. The pore sizes are defined by the triangular dimensions formed by the three Ca positions of Val362 from each subunit. (I-L) Subunit comparisons of ATP-bound Amp2X_{cryst} before the MD simulation (gray) and after the 150 ns MD simulations in the presence of Zn^{2+} at the M1 sites (orange) and in the absence of Zn^{2+} at the M1 sites (cyan). Close-up views of the M1 site (J), the lower body (K), and the fluke (L) are shown in each box. (M-O) Cartoon models of the Zn^{2+} -dependent stabilization mechanism of the ATP-bound Amp2X_{cryst} open state. (M) The model after the 150 ns MD simulation in the absence of Zn^{2+} at the M1 site. (N) The crystal structure model of ATP, Zn^{2+} -bound Amp2X_{cryst}. (O) The model after the 150 ns MD simulation in the presence of Zn^{2+} at the M1 site. In cartoon models (M) and (O), the black arrows denote the movement from the crystal structure model (N).

3.6 Putative Mg^{2+} modulation mechanism gained by electrophysiology

While electrophysiological and computational analyses revealed the mechanism of the M1 site on the Zn^{2+} modulation. The M2 site function was still elusive. Then, the possible function of the M2 site in the modulations of P2X receptors by other divalent cations was further investigated. While ATP exists predominantly as the MgATP^{2-} complex in vivo, a recent electrophysiological analysis demonstrated that distinct subtypes of P2X receptors exhibit differential sensitivities to MgATP^{2-} , leading to modulation by Mg^{2+} (ref. 41). The fast-desensitizing P2X receptors, such as P2X1 and P2X3, can be activated by both MgATP^{2-} and Mg^{2+} -free ATP with similar efficacies⁴¹. In contrast, the slowly desensitizing P2X receptors, such as P2X2, P2X4, and P2X7, can be activated by Mg^{2+} -free ATP, but MgATP^{2-} exhibits only low efficacy with these receptors⁴¹. The M2 site in the Amp2X structure is coupled with the ATP binding site and bridges the receptor and the phosphate groups of ATP (Fig. 3-8B). The coordination of the divalent cation to the β - and γ -phosphate groups of the ATP in the M2 site is reminiscent of the MgATP^{2-} complex. Furthermore, Asp188 in the M2 site is strictly conserved among the fast-desensitizing P2X1 and P2X3 receptors that exhibit similar

sensitivities to both MgATP^{2-} and Mg^{2+} -free ATP (**Fig. 3-3**). These reports led one hypothesis that the M2 site contributes to the accommodation of the MgATP^{2-} complex at the ATP binding site for the MgATP^{2-} sensitivity of these receptors.

To test the hypothesis on the functional role of the M2 site, an electrophysiological analysis with the human P2X1 receptor (hP2X1), which exhibits similar sensitivities to both MgATP^{2-} and Mg^{2+} -free ATP, was performed⁴¹.

3.6.1 Material and methods

3.6.1.1 Plasmid construction, RNA preparation and expression of human P2X1 receptor

The human P2X1 (hP2X1) gene codes 399 amino acid length protein (NCBI accession number: NP_002549.1). The full-length gene of the hP2X1 WT and its mutants generated by the QuickChange method were subcloned into pGEMHE vector, and the RNAs from them were synthesized in a similar manner of zfP2X4 and rP2X4 as described in the section 2.2.1.1 and 3.4.1.1. The oocytes injected each RNA were incubated at 18 °C in ND96 Barth's solution supplemented with 50 µg/ml gentamicin, and were used for recording.

3.6.1.2 Electrophysiological recordings of human P2X1 receptor

Electrophysiological recordings of hP2X1 WT and its mutants were performed using a similar method for zfP2X4 and rP2X4 described in the section 2.2.1.3 and 3.4.1.2. In the recordings analyzing the sensitivity to MgATP^{2-} , two recording solutions, containing 100 mM NaCl, 5 mM HEPES, pH 7.3, and either 5 mM or 0.5 mM MgCl_2 , were used. Under these conditions, $[\text{MgATP}^{2-}]$ and $[\text{Mg}^{2+}$ -free ATP] increase linearly with increasing [ATP] applied. $[\text{Mg}^{2+}$ -free ATP] in the high (5 mM) Mg^{2+} solution is about eight or nine times lower than that in the low (0.5 mM) Mg^{2+} solution, while $[\text{MgATP}^{2-}]$ is exactly the same between the two solutions. Hence, the difference in the ATP dose response is considered to be derived from the reduction of the MgATP^{2-} binding to the mutant channel (**Fig. 3-12E**). A small amount of divalent cation was needed to suppress the endogenous currents of the oocytes, and 0.5 mM MgCl_2 was sufficient in this experiment.

3.6.2 Results

3.6.2.1 Mg^{2+} effect on the M1 site

Because lacking the structure of the P2X1 receptor and the Asp188 at the M2 site in AmP2X, corresponding to Asp170 in P2X1, is located on the loop region (**Fig. 3-3A**), the possibilities that the neighboring Asp171 in P2X1 might be involved in Mg^{2+} recognition or complement the mutation of Asp170 could not be excluded. Therefore, the mutations of both Asp170 and neighboring Asp171 to create the mutant of human P2X1 ($^h\text{D170A}/^h\text{D171A}$) (the superscript “h” refers to human P2X1) for the analysis of the M2 site were introduced. Then, the dose-response relationships to ATP by the ^hWT and the $^h\text{D170A}/^h\text{D171A}$ mutant in the presence of high (5 mM) and low (0.5 mM) extracellular Mg^{2+} concentrations were analyzed (**Fig. 3-12**). The ^hWT receptor exhibited similar half-maximal effective concentration (EC_{50}) values for ATP at the high and low extracellular Mg^{2+} concentrations, consistent with the previous electrophysiological report (**Fig. 3-12A,B**)⁴¹. In contrast, the $^h\text{D170A}/^h\text{D171A}$ mutant exhibited a 5-fold reduction in ATP affinity at the high extracellular Mg^{2+} concentration ($\text{EC}_{50} = 6.55 \pm 1.44 \mu\text{M}$) compared to that at the low extracellular Mg^{2+} concentration ($\text{EC}_{50} = 1.34 \pm 0.27 \mu\text{M}$) (**Fig. 3-12C,D**). The rat P2X2 receptor, which lacks the M2 site (**Fig. 3-3A**), also showed a Mg^{2+} -dependent shift in the ATP concentration-current amplitude relationship⁴¹. In addition, the estimated $\log(K_d)$ value of the P2X2 receptor for Mg^{2+} calculated from the shift was consistent with the known stability constant of Mg^{2+} binding to ATP, indicating the strong preference for Mg^{2+} -free ATP over MgATP^{2-} . Overall, these results suggest that the M2 site, which is coupled with the ATP binding site, may contribute to the differential sensitivities to MgATP^{2-} among subtypes of P2X receptors.

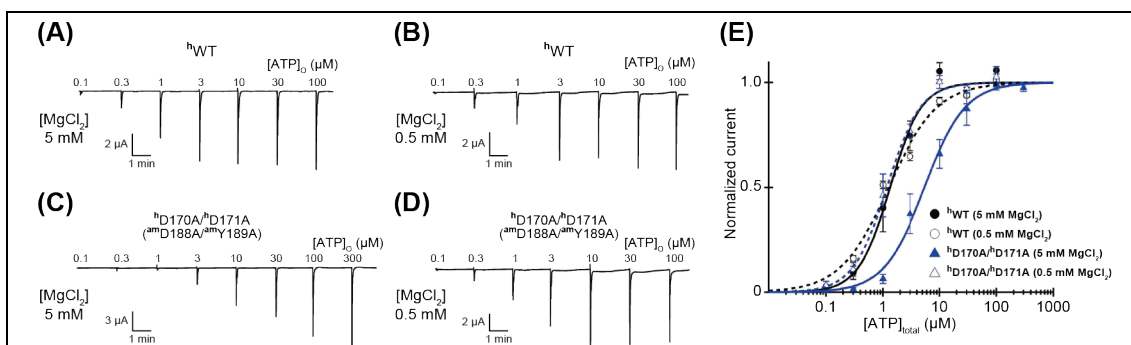


Fig. 3-12 Mg²⁺ effects on the M2 site.

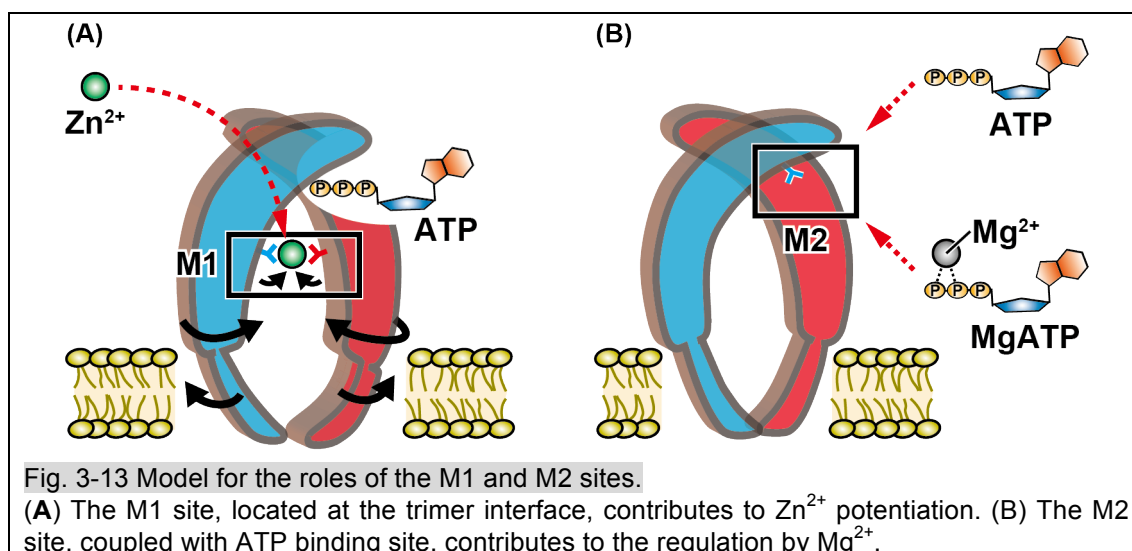
(A-D) Effects of MgCl₂ on the ATP-activated currents in human P2X1 WT (^hWT) and the ^hD170A/^hD171A (^{am}D188A/^{am}Y189A) mutant. (A,B) Representative currents of ^hWT under the 5 mM MgCl₂ conditions (A) and under the 0.5 mM MgCl₂ conditions (B). (C,D) Representative currents of ^hD170A/^hD171A (^{am}D188A/^{am}Y189A) mutant under the 5 mM MgCl₂ conditions (C) and under the 0.5 mM MgCl₂ conditions (D). The numbers above the currents indicate the ATP concentrations. (E) Concentration-response relationships of ATP-evoked currents of ^hWT under the 5 mM MgCl₂ conditions (EC₅₀ = 1.65 ± 0.40 μM, n = 6) and under the 0.5 mM MgCl₂ conditions (EC₅₀ = 1.14 ± 0.09 μM, n = 6) and of the ^hD170A/^hD171A (^{am}D188A/^{am}Y189A) mutant under the 5 mM MgCl₂ conditions (EC₅₀ = 6.55 ± 1.44 μM, n = 7) and under the 0.5 mM MgCl₂ conditions (EC₅₀ = 1.34 ± 0.27 μM, n = 6). Error bars depict mean ± S.E.M. The superscripts “h” and “am” refer to the human P2X1 and AmP2X, respectively. The amino acid residues ^hAsp170 and ^hAsp171 correspond to ^{am}Asp188 (M1 site) and ^{am}Tyr189, respectively.

3.7 Discussion in this chapter

In this chapter, the crystal structure of the invertebrate P2X receptor from the Gulf Coast tick, *Amblyomma maculatum*, was determined in the presence of ATP and Zn²⁺ ion. This structure identified two metal binding sites in the extracellular domain of AmP2X to examine the divalent cation modulation of P2X receptors. Based on the structural information, as well as structural comparison with the previously determined apo, closed and ATP-bound open zfp2X4 receptors, the electrophysiological and computational analyses were further conducted. These results demonstrated that the M1 site, located at the trimer interface, is responsible for Zn²⁺ potentiation by allosterically facilitating the structural change of the body domain in the extracellular region for pore opening (Figs. 3-8A-D and 3-11). Zn²⁺ is an essential ion that modulates numerous ion channels, such as NMDA receptors, and is implicated in controlling their physiological functions⁸⁵. The M1 site is highly conserved among the P2X4 receptors, and consistently, the Zn²⁺ modulation of the P2X4 receptors may be involved in long-term potentiation⁸⁶, implying the physiological significance of the

M1 site among the P2X₄ receptors. In the phylogenetic tree, the invertebrate P2X receptors possessing the M1 site are evolutionarily closer to each other than to the invertebrate P2X receptors lacking the M1 site (**Fig. 3-3B**). The invertebrate P2X receptors lacking the M1 site include those from unicellular organisms, such as the marine green alga *Ostreococcus tauri* and the soil amoeba *Dictyostelium discoideum* (**Fig. 3-3B**). Furthermore, the invertebrate P2X receptor, LsP2X from the great pond snail, with the M1 site (**Fig. 3-3A**) is also reportedly potentiated by Zn²⁺ ion⁸⁷. These findings provide possible insights into how P2X receptors evolutionally acquired the M1 site-mediated Zn²⁺ potentiation (**Fig. 3-13A**).

In contrast, the other divalent cation binding site, the M2 site, is coupled with the ATP binding site and may contribute to MgATP²⁻ sensitivity among some P2X receptors (**Fig. 3-12**). Because ATP predominantly exists as MgATP²⁻ in vivo, it is reasonable that Mg²⁺ ion modulates the ATP-dependent receptor activation in a manner that is directly coupled with ATP binding, rather than through allosteric modulation (**Fig. 3-13B**). Overall, this work provides structural insights into the divalent cation modulations of the P2X receptors, which form the basis for the diverse physiological functions of this ion channel superfamily.



Chapter 4 : Structural insight into the competitive inhibition of P2X receptors

4.1 Introduction

4.1.1 Inhibitory mechanism of P2X receptor

The recent crystallographic and NMR analyses of P2X receptors revealed an unexpected discrepancy regarding the antagonistic mechanism by 2',3'-O-(2,4,6-trinitrophenyl)-ATP (TNP-ATP), one of the subtype non-selective competitive P2X antagonist (**Fig. 1-9**)^{34,43}. The crystal structure of the hP2X3 receptor in complex with TNP-ATP adopted the same conformation as that in the apo, closed state³⁴. In contrast, the NMR analysis of the zfP2X4 receptor reconstituted in nanodiscs showed that TNP-ATP binding induces the expansion of the extracellular domain, in a similar manner to that observed with ATP-dependent activation⁴³. Therefore, the mechanism by which the competitive antagonist works at P2X receptors remains controversial.

Moreover, the P2X7 receptors, the largest subtype among P2X receptor family harboring a unique, long intracellular C-terminus with protein binding, phosphorylation, and lipid recognition sites^{88,89}, stimulate the release of proinflammatory cytokines, such as interleukins and tumor necrosis factor-alpha (TNF- α). Therefore, P2X7 receptors play a crucial role in inflammation, immunity, neurological function, and apoptosis^{90,91}. In addition, the human P2X7R gene is located at chromosome position 12q24, and is highly polymorphic. To date, more than 600 single-nucleotide polymorphisms (SNPs) have been detected, and some of them cause amino-acid substitutions, leading to induce losses or gains of functions in P2X7 receptors⁹²⁻⁹⁴. Accordingly, P2X7 are potential therapeutic candidates for rheumatoid arthritis, hypertension, and atherosclerosis^{95,96}, and clinical trials of chemical compounds targeting P2X7 have been conducted for P2X7-associated diseases²³. Although, the crystal structures of the panda P2X7 (pdP2X7; the “pd” refers to panda) receptor in complex with various subtype-specific non-competitive antagonists were determined quite recently, and these structures provided structural insights clarifying the actions of them to

P2X7 receptors³⁵, the molecular mechanism of competitive antagonist action for P2X7 receptor is still enigmatic.

4.1.2 Study purpose

In this study, the crystal structure of chicken P2X7 receptor in complex with a nonselective competitive antagonist, TNP-ATP, was determined. Furthermore structure-based computational analysis was conducted to clarify the mechanism of competitive antagonist action for P2X receptors, especially for P2X7 receptors, which attracts great interest as potential drug target.

4.2 Functional Characterization of chicken P2X7 (ckP2X7) receptor

First, to find out the good candidate of P2X7 receptors from various species for structural determination, screenings based on the Fluorescence-detection size-exclusion chromatography (FSEC)⁶¹ and FSEC-based thermostability assay (FSEC-TS)²⁵, as well as electrophysiological analyses were performed in a similar manner of AmP2X elucidation as described in the section 3.2.

4.2.1 Material and methods

4.2.1.1 Fluorescence-detection size-exclusion chromatography (FSEC)

The various genes of P2X7 receptor homologues were artificially synthesized (Genscript Co.), and subcloned into pEG BacMam vector, as an N-terminal or C-terminal EGFP fusion, and was expressed in HEK293S GnTI⁻ as described in the section 3.2.1.1. The cells expressing each P2X7 receptor homologue was further collected, solubilized and screened by FSEC (**Fig. 3-1**). The effects of various antagonists to detergent-solubilized P2X7 receptor stabilization were also tested by FSEC-TS.

4.2.1.2 Electrophysiological recordings of ckP2X7 receptor

The chicken P2X7 (ckP2X7) WT and its crystallization construct (ckP2X7_{cryst}; described in the latter section 4.3) were subcloned into pCDNA3.1 vector, and transfections of these plasmids were performed using Hilymax (Dojindo Laboratories, Co.). Both constructs were expressed in HEK293

cells, cultured in DMEM medium at 37°C in a humidified atmosphere of 5% CO₂ and 95% air. Electrophysiological measurements were performed on HEK293 cells, 24-48 h after transfection. The conventional whole-cell configuration under the voltage clamp at room temperature (23± 2°C) was used to obtain the electrophysiological recordings^{33,97}. Patch pipettes were pulled from glass capillaries, using the two-stage puller PP-830 (Narishige Co., Ltd.), and the resistance between the recording electrode filled with pipette solution and the reference electrode in bath solution ranged from 3-5 MΩ. Membrane currents were filtered at 2 kHz using a low-pass Bessel Filter, and measured with an Axon 200B patch clamp amplifier (Molecular Devices). All currents were sampled and analyzed in the Digidata 1440 interface, using Clampex and the Clamp-fit 10.0 software (Molecular Devices). Cells were incubated in a bath solution (150 mM NaCl, 5 mM KCl, 10 mM glucose, 10 mM HEPES, 2 mM CaCl₂, and 1 mM MgCl₂, at the conditional neutral pH of 7.35-7.40). Patch electrodes were filled with a standard internal solution (30 mM NaCl, 120 mM KCl, 1 mM MgCl₂, 0.1 mM CaCl₂, and 5 mM EGTA, at the conditional neutral pH of 7.35-7.40). During electrophysiological recordings, 80-90% of the series resistance was compensated and the membrane potential was held at -60 mV throughout the experiment. ATP and TNP-ATP purchased from Sigma (St. Louis, MO, USA), were prepared in the bath buffer within 2 h of use, and applied using a fast pressure-driven, computer-controlled microperfusion system, OctaFlow08P (ALA Scientific Instruments)⁹⁷. ATP currents were normalized to the cell membrane capacitance. Dose-response curve data were collected from recordings of a range of TNP-ATP concentrations. The corresponding currents were normalized to the maximal current amplitude of ATP (50 μM in Ca²⁺-free solution containing 5 mM EGTA), and ATP-gated currents were recorded after the regular 40–50 s ATP application every 8 min.

4.2.1.3 Fluorescence measurement

The purified ckP2X7_{cryst} protein and the SEC buffer (20 mM HEPES, pH 7.0, 100 mM NaCl, 10% glycerol, 0.05% DDM) mixed with each concentration of TNP-ATP were incubated at 4 C for over 1

h, respectively. The mixed solutions were dispensed in a 96-well, flat-bottom plate, in a 50 μ l sample volume. Fluorescence measurement was performed using a 2030 ARVO X3 Multilabel Reader (PerkinElmer), equipped with 405 nm emission and 535 nm excitation filters⁹⁸.

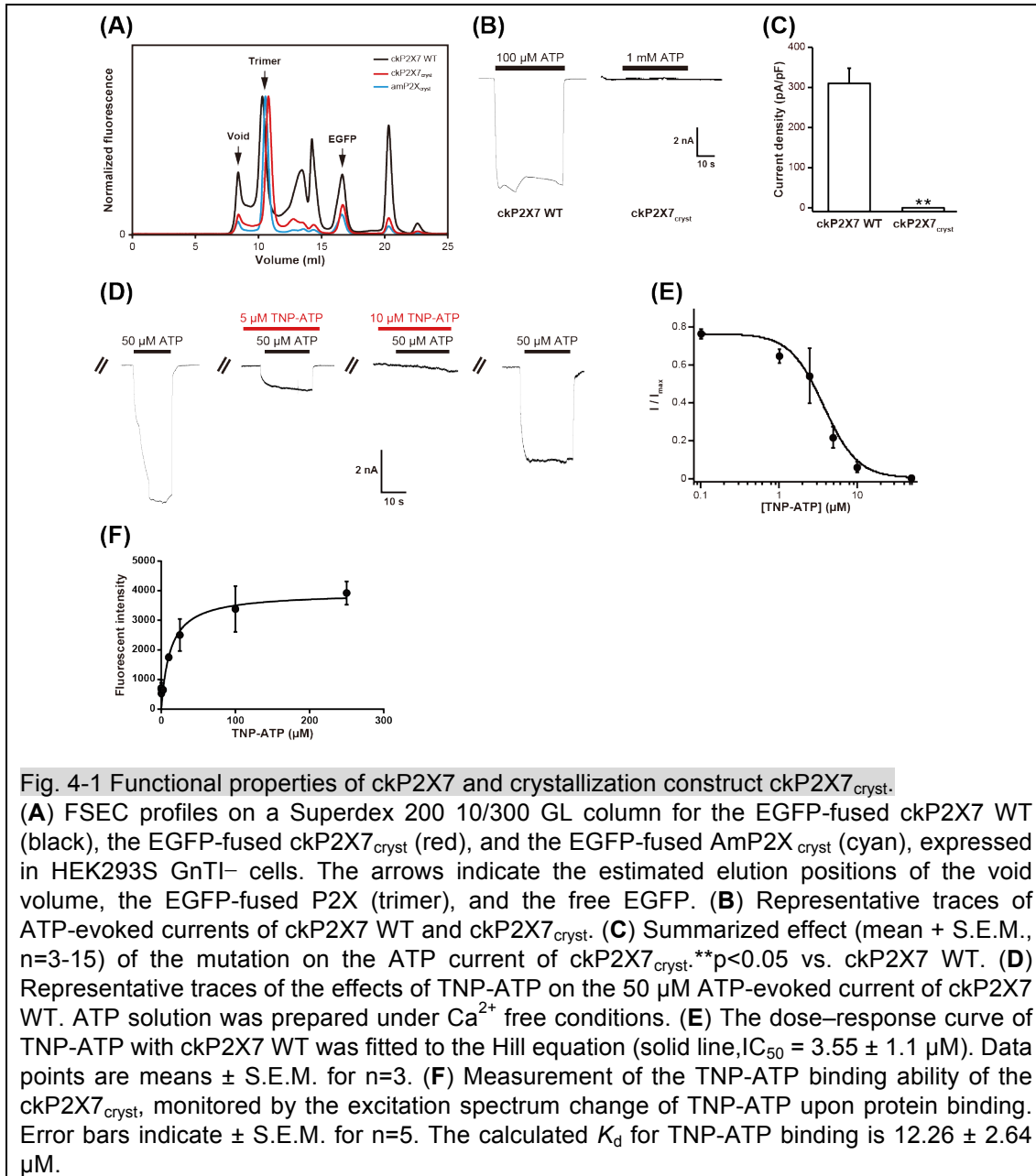
4.2.2 Results

4.2.2.1 Screening ckP2X7 receptor as a suitable candidate for structural study by FSEC

Following the methods in 4.2.1.1, the FSEC screening of various P2X7 homologues were performed. As a result, one of the truncation construct of N-terminally GFP-tagged chicken P2X7 receptor (ckP2X7; NCBI accession number: XP_001235163), showed a sharp, symmetrical profile, comparable to that of the AmP2X receptor, indicating that ckP2X7 is a promising target for structural analysis (**Fig. 4-1A**). The chicken P2X7 receptor shares 45.0% identity and 61.9% similarity to the human P2X7 receptor (**Fig. 4-2**). The crystallization construct termed ckP2X7_{cryst} was further designed by using FSEC method together with previous Δ P2X4-C and AmP2X constructs²⁸. The ckP2X7_{cryst} construct (Δ N27/ Δ C214/N190Q) lacks the regions encoding 27 N-terminal and 214 C-terminal residues to remove disordered regions, and includes the mutation of Asn190 to exclude putative glycosylation site (**Fig. 4-1A**).

4.2.2.2 Electrophysiological and biochemical analyses of ckP2X7 receptor

Following the methods in 4.2.1.2, the patch clamp recordings using HEK293 cells expressing ckP2X7 WT and ckP2X7_{cryst} were performed. ATP activated biphasic currents and TNP-ATP blocked ATP-dependent currents (**Fig. 4-1B-E**), in similar manners to other P2X7 receptors^{14,23}. Although any ATP-dependent ckP2X7_{cryst} associated current was not detected (**Fig. 4-1B,C**), the ckP2X7_{cryst} construct still had TNP-ATP binding activity (**Fig. 4-1F**). Taken together, these results from the electrophysiological and fluorescent binding analyses demonstrated that the ckP2X7 receptor-associated current has similar properties to those of other P2X7 receptors and is inhibited by TNP-ATP.



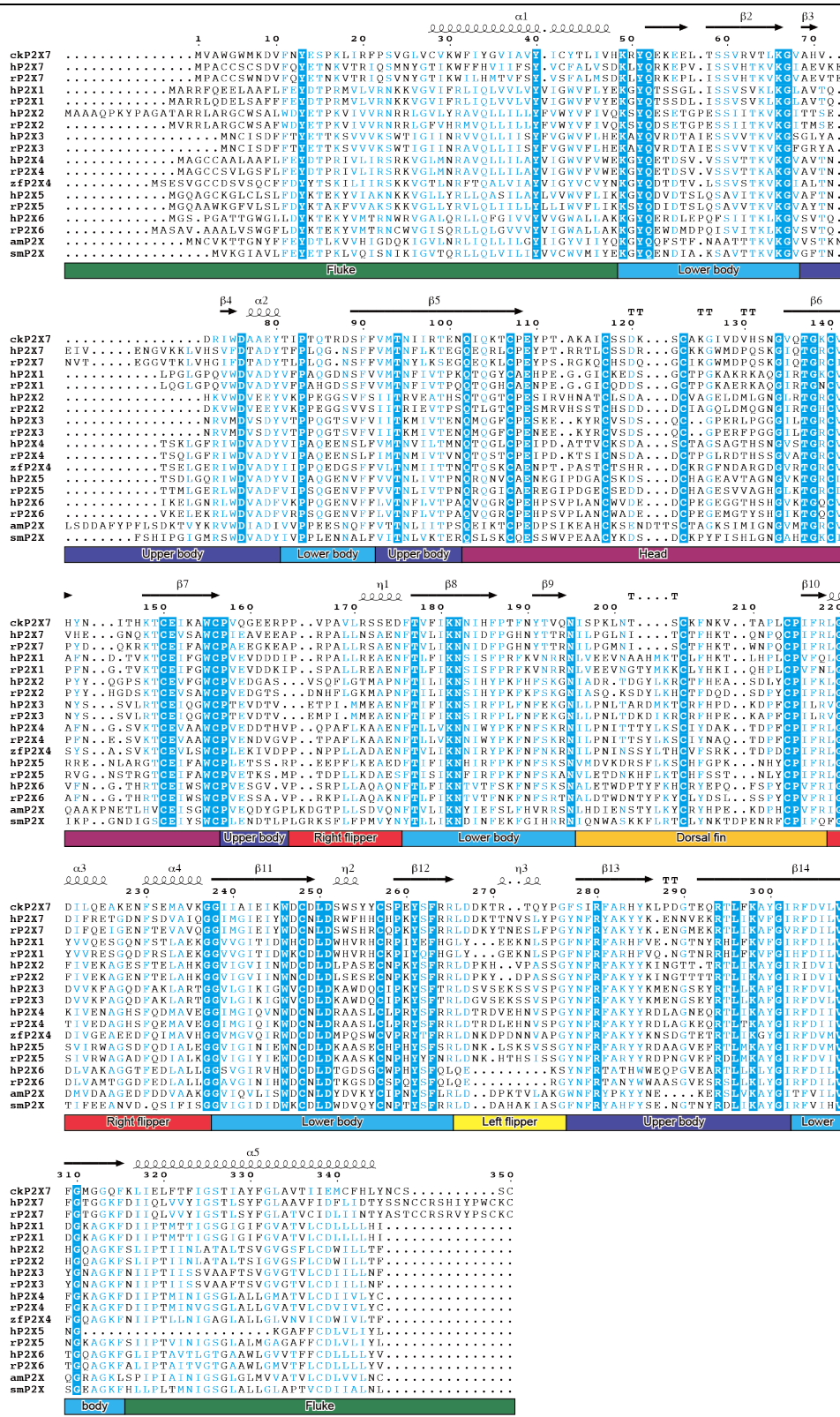


Fig. 4-2 Sequence alignment of P2X receptors. The amino acid sequences of P2X receptors were aligned using Clustal Omega, and are shown using ESPrpt3. Secondary structure elements from the ckP2X7_{cryst} are depicted in cartoon representations and are labeled above the alignments, and the colors of the domains based on the dolphin-like model are presented below the alignments. For the sequence

alignment, the following vertebrate and invertebrate P2X receptors were used: chicken (ckP2X7, NCBI accession number: XP_001235163), human (hP2X1, NP_002549; hP2X2, NP_733782; hP2X3, NP_002550; hP2X4, Q99571; hP2X5, Q93086; hP2X6, AAF13303; and hP2X7, AAH11913), rat (rP2X1, P47824; rP2X2, NP_446108; rP2X3, CAA62594; rP2X4, AAC52380; rP2X5, CAA63052; rP2X6, CAA63053; and rP2X7, CAA65131), zebrafish (zfP2X4, AAK00945), Gulf Coast tick (amP2X, AEO34575), and blood fluke (smP2X, CAH04147) μ M.

4.3 Structure determination of the ckP2X7 receptor in the presence of TNP-ATP

Based on the functional characterization of the ckP2X7 receptor, which indeed function as ATP-gated cation channel and inhibited by TNP-ATP, which was similar to other known P2X7 receptors. The crystallization of the ckP2X7_{cryst} in the presence of TNP-ATP was performed.

4.3.1 Material and methods

4.3.1.1 Plasmid construction of ckP2X7 receptor for structural determination

As described in the section 4.2.2.1, the ckP2X7_{cryst} construct, was subcloned into pEG BacMam vector with an N-terminal EGFP fusion with an octa-histidine affinity (8xHis-EGFP) tag, and following a tobacco etch virus (TEV) cleavage site.

4.3.1.2 Baculovirus preparation of the crystallization construct ckP2X7_{cryst}

The baculovirus was prepared following the Bac-to-Bac system protocol (Invitrogen), in a similar manner of AmpP2X_{cryst} as described in the section 3.3.1.2.

4.3.1.3 Expression and purification of the ckP2X7_{cryst}

The ckP2X7_{cryst} construct was expressed by adding 10% P2 virus stock and 10 mM sodium butyrate to HEK293S GnTI⁻ cells (3.0×10^6 cells/ml, 1L), and by incubating at 37°C in 16-18 hr and following at 30°C in 1 day. Cell collection and disruption, as well as membrane isolation were performed in a similar manner of zfP2X4 as described of in the section 2.3.1.3. The membrane fraction was solubilized for 1 h at 4°C in a buffer (50 mM Tris, pH 8.0, 150 mM NaCl, 10% glycerol, 40 mM DDM, 0.2 Unit/L Apyrase (New England Biolabs)). The detergent-soluble fraction was incubated with Talon metal affinity resin (Clontech), washed with 20 mM imidazole and eluted with

250 mM imidazole. After TEV protease digestion and Endo H treatment, to remove the 8xHis-EGFP tag and part of the N glycans, the protein was isolated by size-exclusion chromatography on a Superdex 200 10/300 GL column (GE Healthcare) in size-exclusion chromatography buffer (20 mM HEPES, pH 7.0, 100 mM NaCl, 10% Glycerol, 1 mM DDM (Nacalai tesque)) (**Fig. 4-3A**). The peak fractions of the protein were collected and concentrated to 3 mg/ml using a centrifugal filter device (Millipore, 30 kDa molecular weight cut off)

4.3.1.4 Crystallization of the ckP2X7_{cryst}

Before crystallization, 0.1 mM TNP-ATP (TOCRIS) was added to the protein solutions and incubated at 4°C, 1 hr. The crystals were grown at 4°C by the sitting drop vapor diffusion method in a 96-well plate. The crystals of ckP2X7_{cryst} appeared within 3 days under the following conditions (32% PEG400, 0.5 M sodium sulfate, 0.05 M lithium chloride, 0.05 M Tris, pH 8.0) (**Fig. 4-3B**). The crystals were harvested and cryoprotected, in a reservoir solution supplemented with 25% glycerol, 1 mM DDM and 0.1 mM TNP-ATP. Crystals were flash-frozen in liquid nitrogen for X-ray diffraction experiments.

4.3.1.5 Data collection and structure determination

The X-ray diffraction data were collected at the Swiss Light Source (SLS) beamline X06SA-PXI. Diffraction data were processed using DIALS⁹⁹, and scaled using AIMLESS¹⁰⁰ (**Fig. 4-3C**). The structure of ckP2X7_{cryst} was obtained by molecular replacement with MOLREP¹⁰¹, using one subunit of the ATP-bound Amp2X structure (PDB ID: 5F1C) as the template. The structure thus obtained was further refined by using REFMAC5 (ref. 102), PHENIX⁵³, and COOT⁵⁴, with three-fold non-crystallographic symmetry and secondary structure restraints. Crystallographic data and refinement statistics are presented in the figure (**Fig. 4-3D**). The coordinate of the TNP-ATP bound ckP2X7_{cryst} structure was deposited on Protein Data Bank (PDB) under the accession code 5XW6.

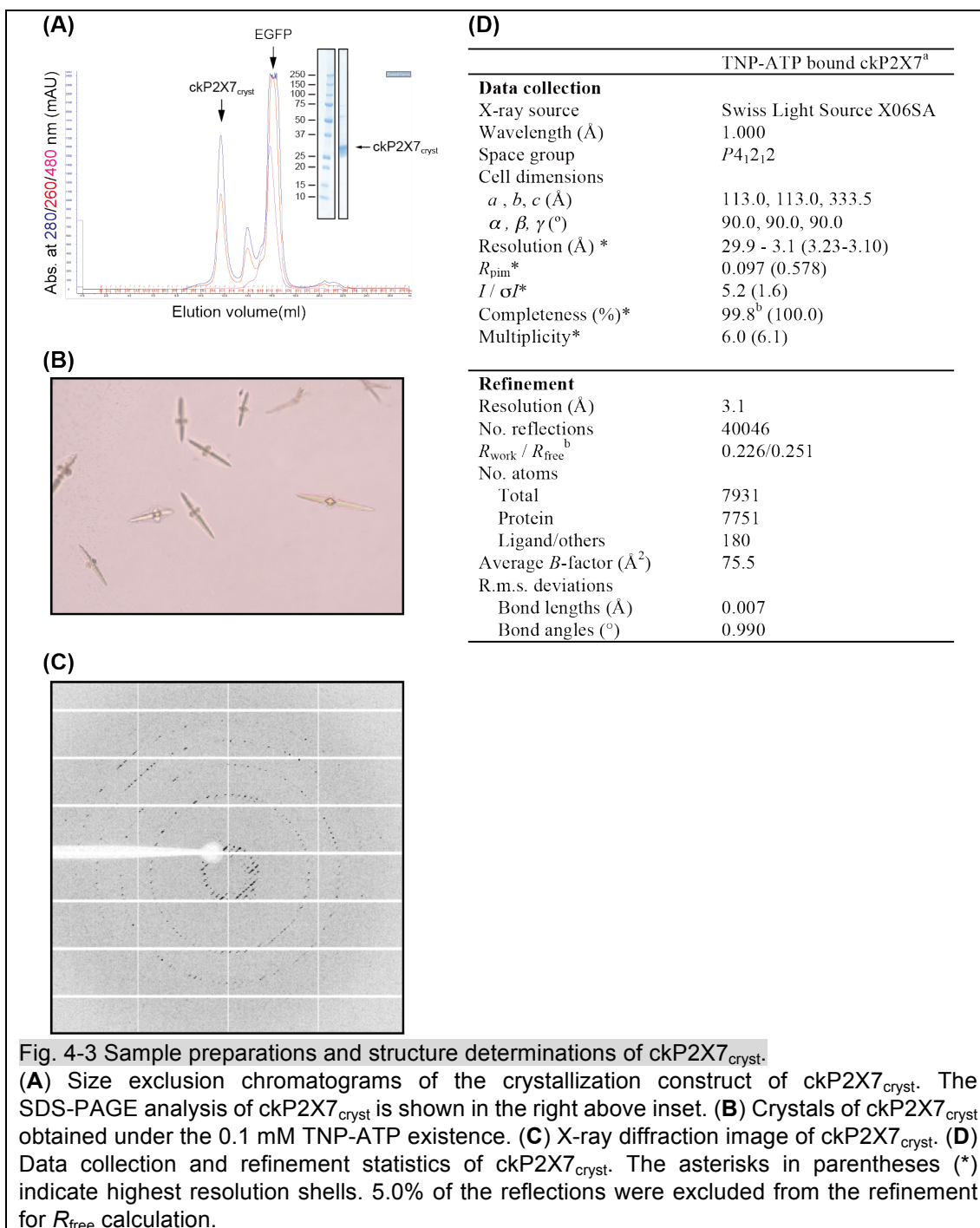


Fig. 4-3 Sample preparations and structure determinations of ckP2X7_{cryst}.

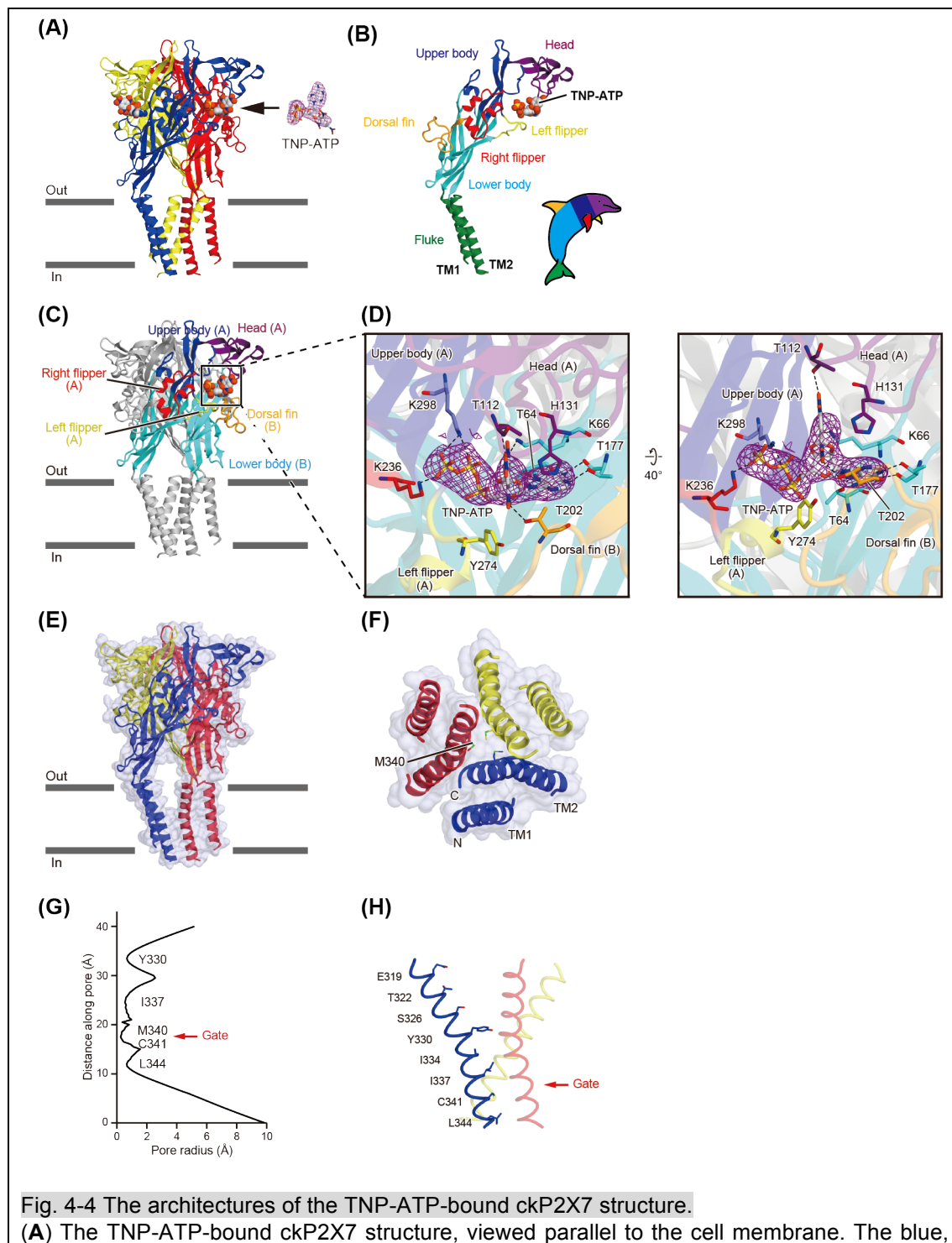
(A) Size exclusion chromatograms of the crystallization construct of ckP2X7_{cryst}. The SDS-PAGE analysis of ckP2X7_{cryst} is shown in the right above inset. **(B)** Crystals of ckP2X7_{cryst} obtained under the 0.1 mM TNP-ATP existence. **(C)** X-ray diffraction image of ckP2X7_{cryst}. **(D)** Data collection and refinement statistics of ckP2X7_{cryst}. The asterisks in parentheses (*) indicate highest resolution shells. 5.0% of the reflections were excluded from the refinement for *R*_{free} calculation.

4.3.2 Results

4.3.2.1 Overall structure of the ckP2X7_{cryst}

The X-ray diffraction data of ckP2X7_{cryst} crystal were collected to 3.1 Å resolution, successfully led to determine the structure (**Fig. 4-3**). The overall assembly and subunit folding of ckP2X7_{cryst} are consistent with those of the previously determined P2X structures^{27,28,34,35}, sharing the

chalice-like trimeric architecture with a large hydrophilic extracellular domain, two trans- membrane helices, and intracellular termini, resembling the shape of a dolphin (Fig. 4-4A,B)²⁷. In the extracellular domain, the electron density for the TNP-ATP molecule was detected at the inter-subunit ATP binding pocket (Fig. 4-4C,D).



red, and yellow colors correspond to each subunit. The omit $F_o - F_c$ density map contoured at 2.5σ is presented for the TNP-ATP molecular density. **(B)** A subunit of the TNP-ATP-bound ckP2X7_{cryst}, colored according to the previously proposed dolphin-like model. The sequence comparison with previously determined P2X receptor structures defined the domains of ckP2X7_{cryst} as Fluke (Cys28-Lys49, and Ser316-Asn346), Lower body (Arg50-Val68, Thr81-Phe91, Phe176-Asn195, Gly238-Arg265, and Arg303-Phe315), Upper body (Ala69-Tyr80, Val92-Asn101, Pro157-Pro164, and Phe277-Ile302), Head (Gln102-Cys156), Right flipper (Pro165-Asp175, and Leu219-Gly237), Left flipper (Leu266-Gly276), and Dorsal fin (Ile196-Arg218). **(C,D)** The overall **(C)** and close-up **(D)** view of TNP-ATP recognition manner. In **(D)**, the omit $F_o - F_c$ map contoured at 2.5σ , showing the electron density of TNP-ATP. The amino acid residues and TNP-ATP are depicted by stick models. The molecule is colored according to the dolphin-like model. Dotted black lines indicate hydrogen bonds ($<3.3 \text{ \AA}$). **(E)** The surface model with a cartoon representation of the TNP-ATP-bound ckP2X7 structure. **(F)** The surface model with a cartoon representation of the transmembrane domain in the TNP-ATP-bound ckP2X7 structure, viewed from the intracellular side. Amino-acid residues involved in the pore constriction region are depicted by stick models. **(G)** The pore radius for the TNP-ATP-bound ckP2X7 structure along the pore center axis. The pore size was calculated with the program HOLE. **(H)** Pore-lining residues of the TNP-ATP-bound ckP2X7 structure are shown in stick representations

4.3.2.2 Comparison with the previously determined P2X receptor structures

While TNP-ATP acts as an antagonist of P2X7 receptors, the extracellular domain structure of ckP2X7_{cryst} is similar to those of the ATP-bound, activated hP2X3 and zfP2X4 structures (**Fig. 4-5A,D**), rather than those of the apo, closed hP2X3, zfP2X4, and pdP2X7 structures or the antagonist bound, closed hP2X3 and pdP2X7 structures (**Fig. 4-5C,E,F,H**), consistent with the previous NMR analysis of the zfP2X4 receptor⁴³.

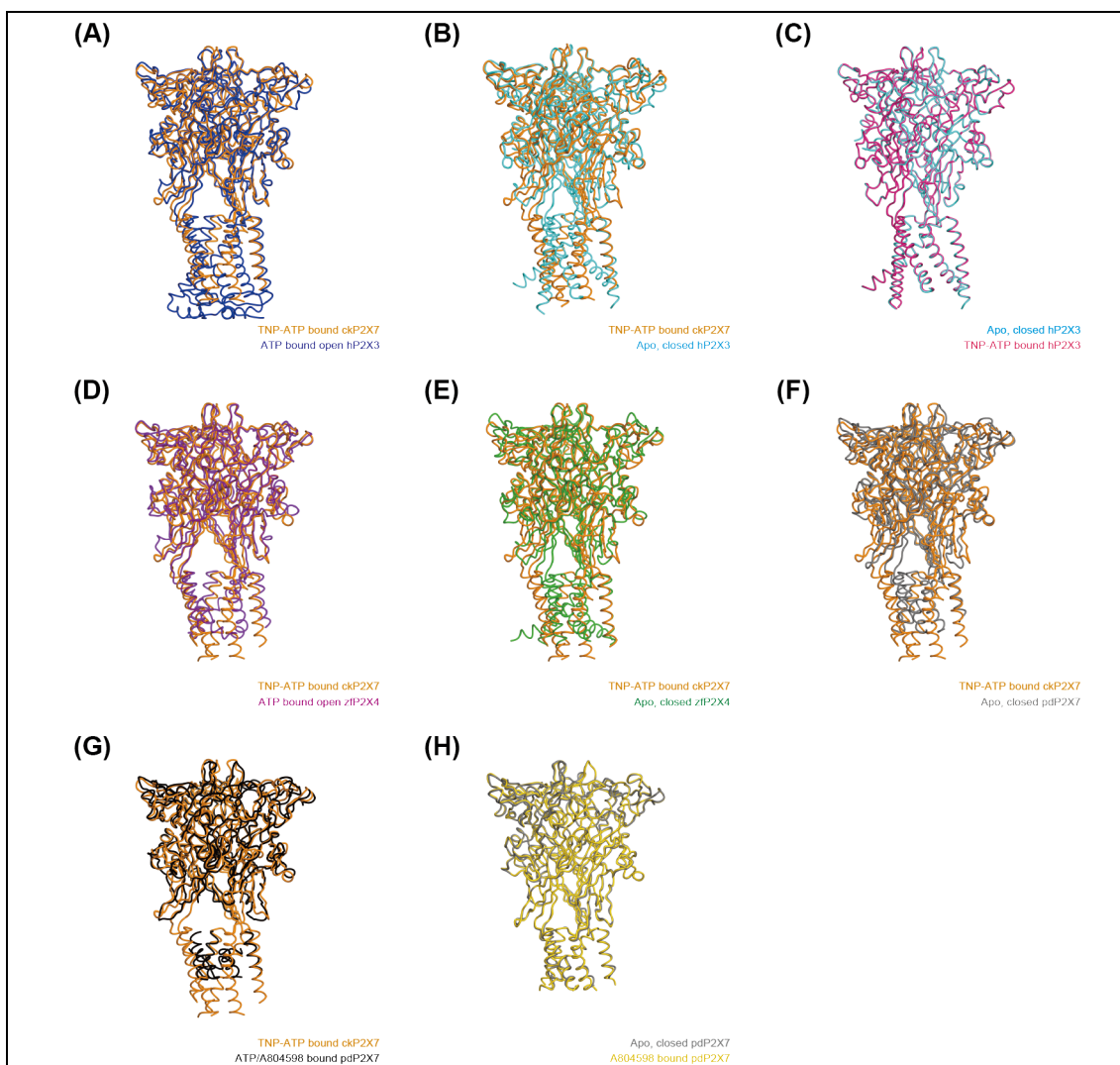
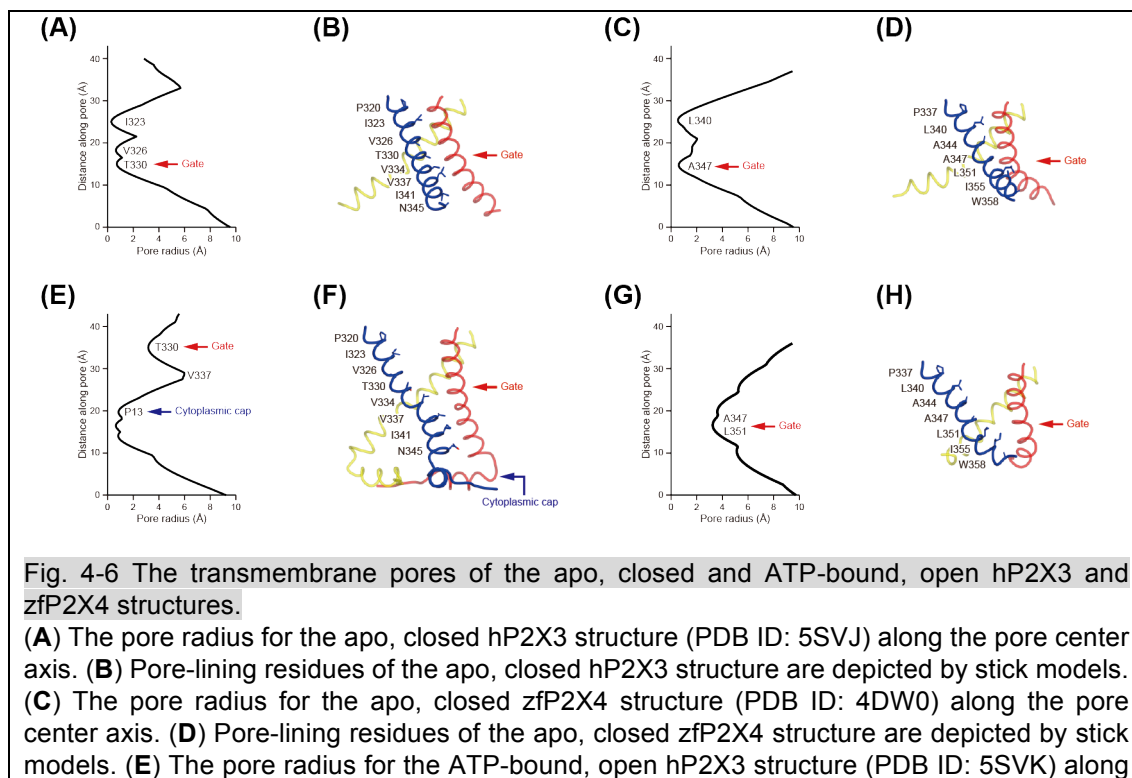


Fig. 4-5 Comparison of the overall structures for ckP2X7, hP2X3, zfP2X4 and pdP2X7.
(A) The superimposition of the TNP-ATP-bound ckP2X7 (orange) and ATP-bound, open hP2X3 (blue, PDB ID: 5SVK) structures. The RMSD value is 1.87 Å for 856 Cα atoms between trimers. **(B)** The superimposition of the TNP-ATP-bound ckP2X7 (orange) and apo, closed hP2X3 (cyan, PDB ID: 5SVJ) structures. The RMSD value is 2.31 Å for 758 Cα atoms between trimers. **(C)** The superimposition of the apo, closed hP2X3 (cyan) and TNP-ATP-bound hP2X3 (pink, PDB ID: 5SVQ) structures. The RMSD value is 0.22 Å for 954 Cα atoms between trimers. **(D)** The superimposition of the TNP-ATP-bound ckP2X7 (orange) and ATP-bound, open zfP2X4 (purple, PDB ID: 4DW1) structures. The RMSD value is 1.95 Å for 836 Cα atoms between trimers. **(E)** The superimposition of the TNP-ATP-bound ckP2X7 (orange) and apo, closed zfP2X4 (green, PDB ID: 4DW0) structures. The RMSD value is 2.35 Å for 814 Cα atoms between trimers. **(F)** The superimposition of the TNP-ATP-bound ckP2X7 (orange) and ATP/antagonist (A804598) bound pdP2X7 (black, PDB ID: 5U2H) structures. The RMSD value is 1.73 Å for 790 Cα atoms between trimers. **(G)** The superimposition of the TNP-ATP-bound ckP2X7 (orange) and apo, closed pdP2X7 (gray, PDB ID: 5U1L) structures. The RMSD value is 2.18 Å for 787 Cα atoms between trimers. **(H)** The superimposition of the apo, closed pdP2X7 (gray) and A804598-bound pdP2X7 (gold, PDB ID: 5U1V) structures. The RMSD value is 0.45 Å for 949 Cα atoms between trimers.

The transmembrane pore is formed by the TM2 helices with the residues from Asp319 to Leu344

lining the pore, consistent with the previous electrophysiological analysis (**Fig. 4-4E-H**)^{32,103}. In the

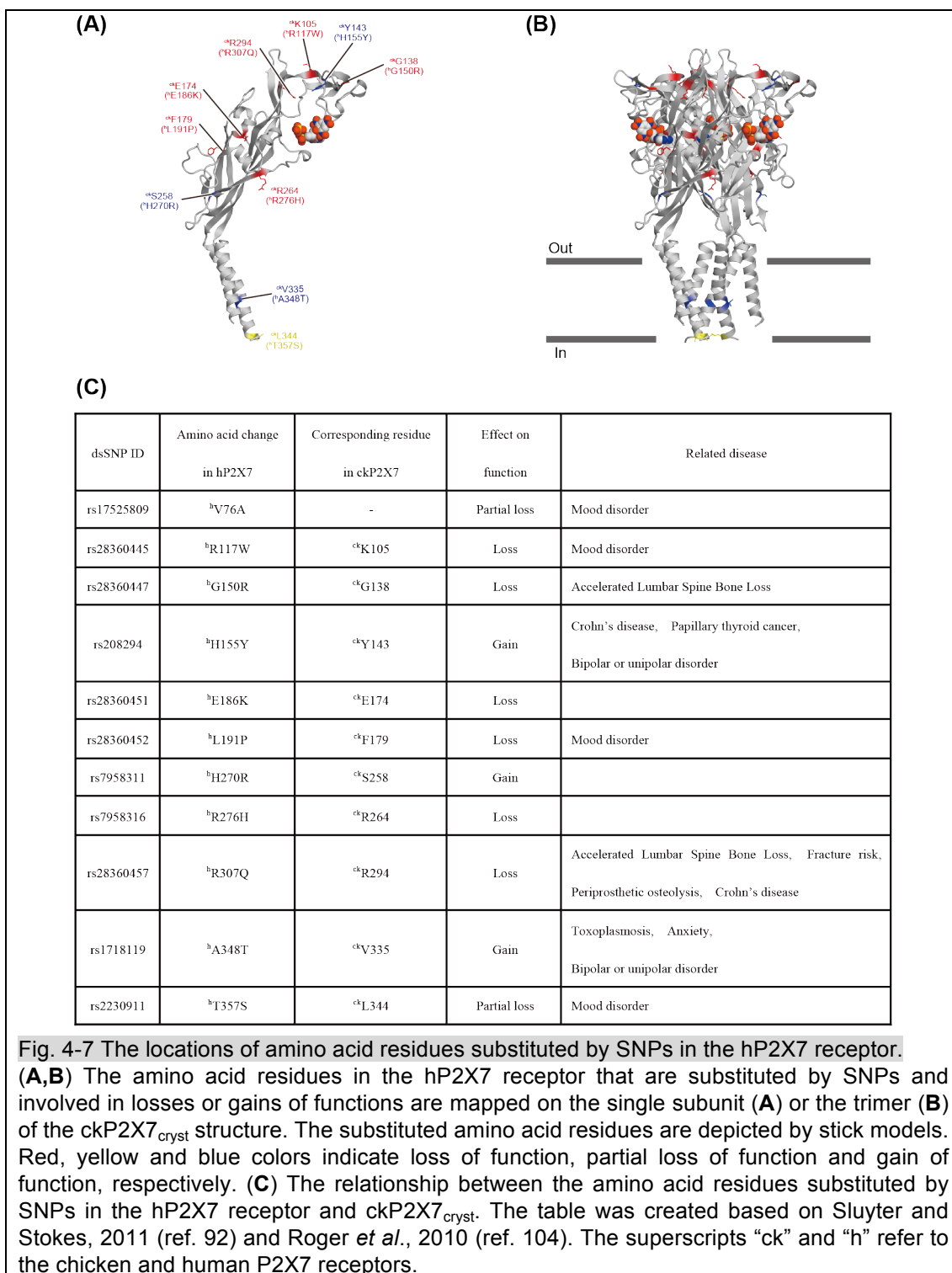
most constricted region, the pore radius is smaller than 0.3 Å, which is too narrow for ion conduction. The constricted region is formed by the Met340 and Cys341 residues near the cytoplasmic side (**Fig. 4-4F-H**). In contrast, in the zfP2X4 and hP2X3 structures in the apo, closed state, the most constricted region is located near the extracellular side, rather than the cytoplasmic side (**Fig. 4-6**)^{27,28,34}. In those structures, the residues corresponding to Thr322 and Ser326 in ckP2X7 define the constricted channel gate (**Figs. 4-2 and 4-6**). This partial pore opening on the extracellular side in the ckP2X7cryst structure is apparently due to the extracellular domain architecture, which is similar to those of the ATP-bound, activated P2X structures (**Fig. 4-5A,D**). Notably, the transmembrane domain architectures of the previously determined ATP-bound structures of zfP2X4 and amP2X, including the large inter-subunit gaps, are partially distorted from those in the native lipid environment, potentially due to detergents or truncations utilized for crystallization^{28,31}. However, such abnormal inter-subunit gaps are not observed in the transmembrane region of the ckP2X7cryst structure (**Fig. 4-4G,H**). Overall, this structure represents a TNP-bound, inactivated state of the P2X7 receptor.



the pore center axis. **(F)** Pore-lining residues of the ATP-bound, open hP2X3 structure are depicted by stick models. **(G)** The pore radius for the ATP-bound, open zfP2X4 structure (PDB ID: 4DW1) along the pore center axis. **(H)** Pore-lining residues of the ATP-bound, open zfP2X4 structure are depicted by stick models. The pore size was calculated by the program HOLE.

4.3.2.3 Mapping of functionally important mutations

Numerous SNPs of P2X7 have been identified, and some are associated with amino-acid substitutions implicated in several diseases, such as cancer, chronic pain, osteoporosis, and depression^{92–94}. To gain insight these important mutations, the amino-acid residues in the hP2X7 receptor that are substituted by SNPs and involved in losses or gains of functions^{23,92,104} onto the ckP2X7_{cryst} structure were mapped (**Fig. 4-7**). While the gain-of-function substitutions are observed in both the extracellular and transmembrane domains, the loss-of-function substitutions are observed only in the extracellular domain. The mutations observed in the extracellular domain are not directly involved in trimer formation. One amino-acid residue, ^{ck}Phe179 (^hLeu196Pro), which is associated with affective mood disorder¹⁰⁴, is involved in ligand recognition but does not form a direct hydrogen bond interaction (the superscripts “ck” and “h” refer to the chicken and human P2X7 receptors, respectively). These results indicate that the amino-acid substitutions observed in the extracellular domain are not involved in the direct trimer formation and ATP binding by the hP2X7 receptor, but they affect the conformational change of the extracellular domain required for channel activation. Intriguingly, in our inactivated ckP2X7_{cryst} structure, all of the loss-of-function substitutions are located in the secondary structure (α -helix and β -sheet) regions, suggesting that the loss-of-function substitutions may affect the structural integrity in the inactivated state. In the transmembrane domain, two substitutions, ^{ck}Val335 (^hAla348Thr) and ^{ck}Leu344 (^hThr357Ser), which are associated with toxoplasmosis and bipolar disorder⁹², are observed close to the pore constriction site, suggesting that these substitutions may affect the pore size of the hP2X7 receptor.



4.3.2.4 TNP-ATP recognition

In the TNP-ATP-bound ckP2X7 structure, the TNP-ATP molecule is located in the ATP binding pocket, and thus interacts with the head, upper body, right flipper, and left flipper domains from one subunit, and the lower body and dorsal fin domains from the neighboring subunit (**Fig. 4-4C**).

Unexpectedly, the structure revealed that the binding mode of TNP-ATP is quite different from that in the recently reported TNP-ATP-bound hP2X3 structure (**Fig. 4-8**)³⁴.

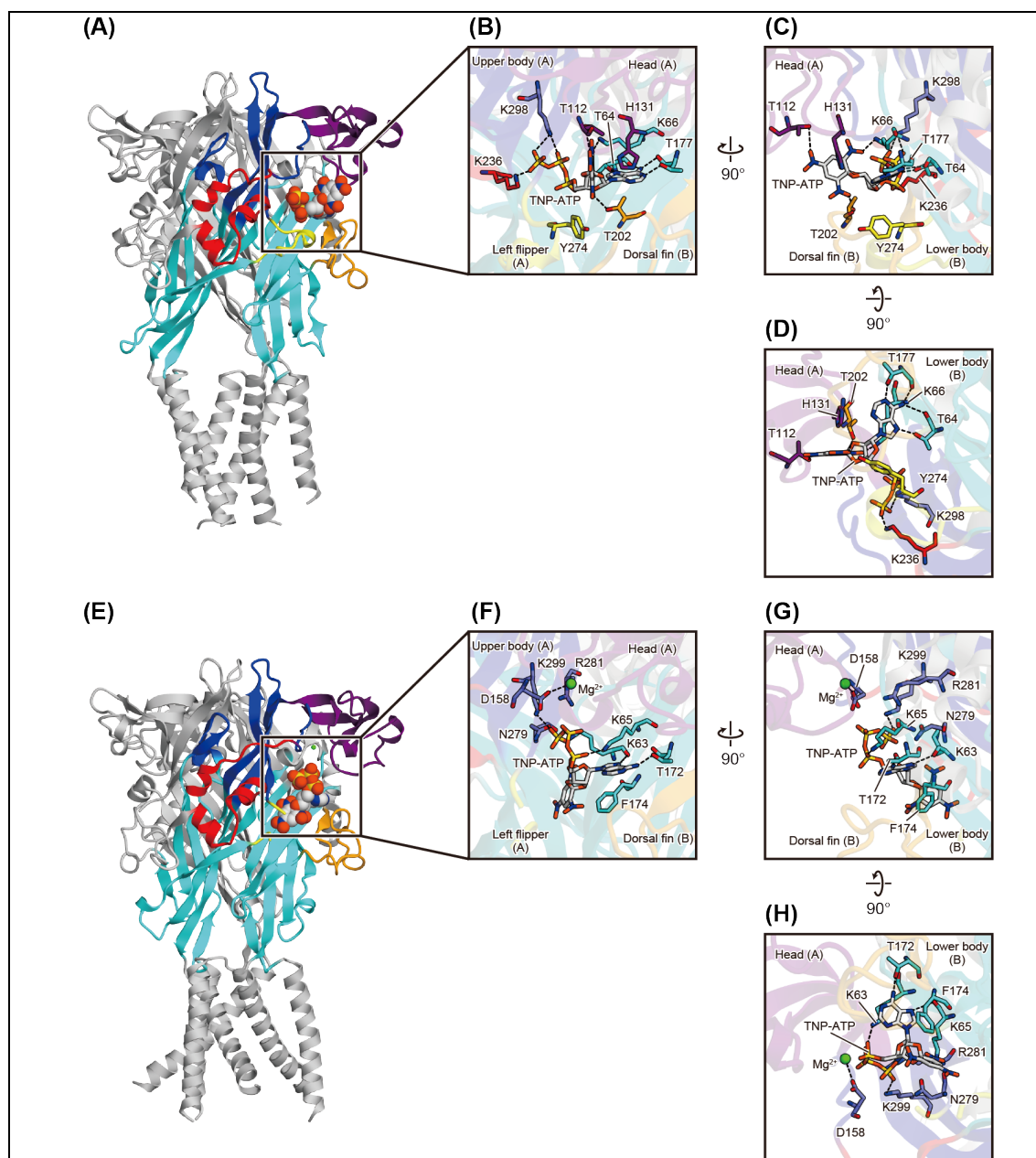


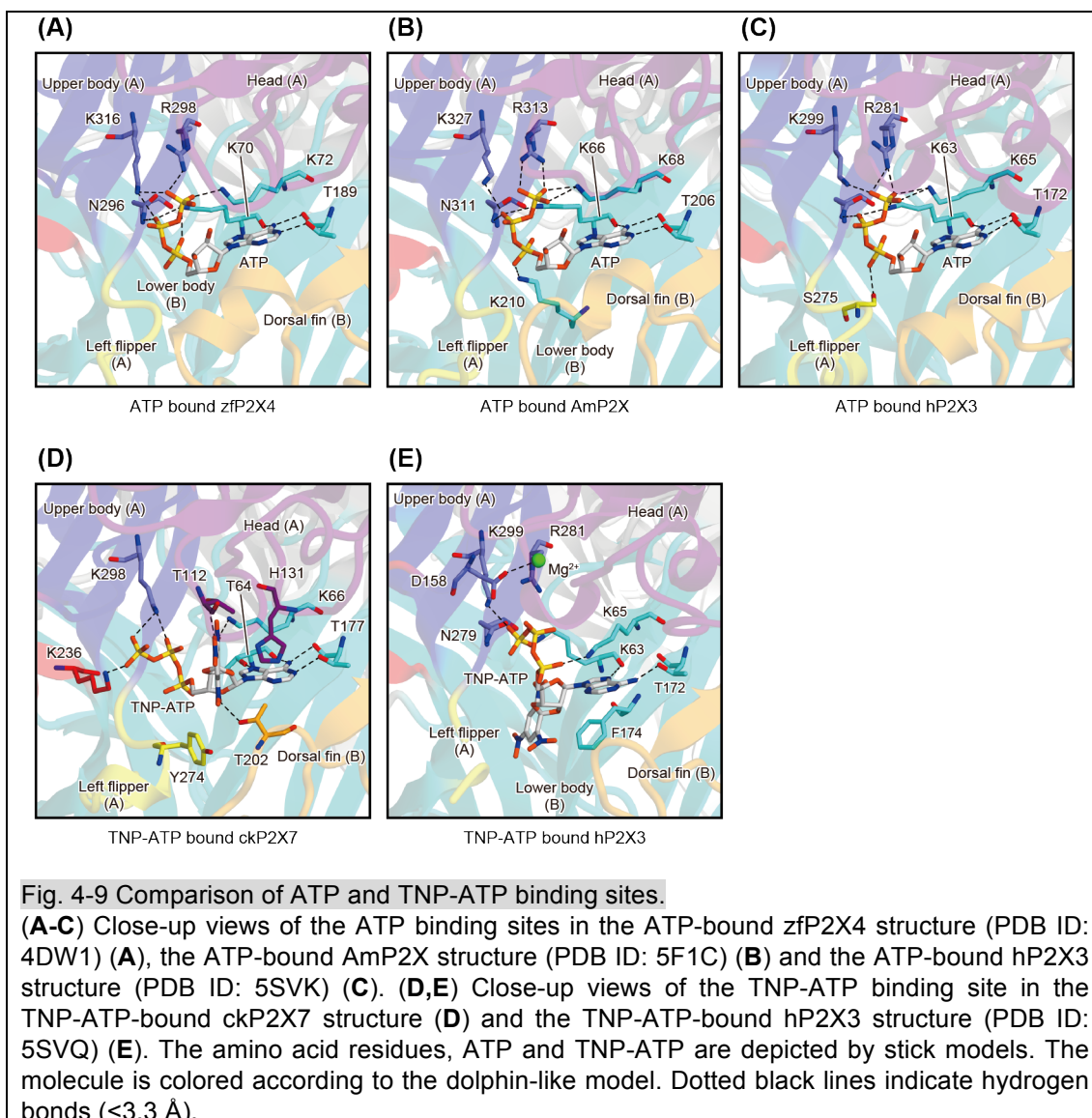
Fig. 4-8 Comparison of TNP-ATP binding sites in the TNP-ATP-bound structures of ckP2X7 and hP2X3.

(**A-D**) Overall (**A**) and close-up (**B-D**) views of the TNP-ATP binding sites in the TNP-ATP-bound ckP2X7 structure. (**E-H**) Overall (**E**) and close-up (**F-H**) views of the TNP-ATP binding sites in the TNP-ATP-bound hP2X3 structure (PDB ID: 5SVQ) (b). The molecules are colored according to the dolphin-like model. The TNP-ATP and amino-acid residues are depicted by stick models. The Mg²⁺ ion is depicted by a green sphere. Dotted black lines indicate hydrogen bonds (<3.3 Å)

First, the adenine ring of TNP-ATP adopts a similar orientation to that observed in the previously

reported ATP-bound P2X structures^{28,34}, and thus forms hydrogen bonds with the side chains of the highly conserved ^{ck}Thr177 and the main chain carbonyl groups of ^{ck}Thr64 and ^{ck}Thr177 (**Figs. 4-2, 4-8A-D and 4-9**). Additional hydrogen bonds are formed with the side chain of ^{ck}Thr64 (**Figs. 4-2, 4-8A-D and 4-9**). In contrast, in the TNP-ATP-bound hP2X3 structure, the adenine ring of TNP-ATP adopts a distinct orientation from those observed in the ATP-bound structures (**Figs. 4-2, 4-8E-H and 4-9**). It interacts with the side chain of ^hThr172 (^{ck}Thr177) and the main chain carbonyl group of ^hLys63 (^{ck}Thr64), but not with the main chain carbonyl group of ^hThr172 (^{ck}Thr177) (**Figs. 4-2, 4-8E-H and 4-9**), due to the different orientation of the adenine ring.

Next, in the TNP-ATP-bound ckP2X7 structure, the phosphate groups of TNP-ATP adopt a totally extended conformation, whereas the phosphate groups of ATP in the previous structures form a bent, “U-shaped” conformation (**Figs. 4-8A-D and 4-9**). This extended conformation of the phosphate groups in the TNP-ATP-bound ckP2X7 structure enables the formation of two hydrogen bonding interactions with the side chains of ^{ck}Lys236 from the right flipper domain and ^{ck}Lys298 from the upper body domain. The interactions between the right flipper domain and the phosphate groups are not visible in the previously determined ATP-bound P2X structures (**Fig. 4-9A-C**). In contrast, the phosphate groups of TNP-ATP in the TNP-ATP-bound hP2X3 structure are partially bent in a “Y-shaped” conformation (**Figs. 4-8E-H and 4-9**).



Finally, the ribose group of TNP-ATP in the TNP-ATP-bound ckP2X7 structure adopts a similar orientation to that in the ATP-bound structures, with the C2' and C3' atoms of the ribose group facing toward the head domain. This orientation of the ribose group and the following α -phosphate is stabilized by weak interactions with the left flipper domain at the ^{ck}Tyr274 residue, in a similar manner to that observed in the ATP-bound hP2X3 structure (**Figs. 4-8A-D and 4-9C,D**). However, the ribose group of TNP-ATP in the TNP-ATP-bound hP2X3 structure is rotated by $\sim 180^\circ$, and thus the C2' and C3' atoms of the ribose group face toward the left flipper region (**Figs. 4-8E-H and 4-9**). The different orientation of the ribose group also changes that of the trinitrophenyl group: the trinitrophenyl group in the TNP-ATP-bound ckP2X7 structure contacts the head and dorsal fin

domains, forming three hydrogen bonds with the side chains of ^{ck}Lys66, ^{ck}Thr112, and ^{ck}Thr202 (**Fig. 4-8A-D**). Consistently, previous electrophysiological analyses of the P2X1 and P2X4 receptors indicated that the head and dorsal fin domains are associated with the TNP-ATP binding^{31,105}. In contrast, the trinitrophenyl group in the TNP-ATP-bound hP2X3 structure is buried in the hydrophobic region between the lower body domain and the mostly disordered left flipper region, and thus there is no hydrophilic interaction between the receptor and the trinitrophenyl group, despite its high hydrophilicity (**Figs. 4-8E-H and 4-9**).

4.3.2.5 Comparison with the apo, closed and ATP-bound open P2X receptor structures

To further gain insights into how TNP-ATP works at the receptor, the TNP-ATP-bound ckP2X7 structure with the apo, closed, and ATP-bound, open states of previously solved P2X receptor structures were compared (**Fig. 4-10**).

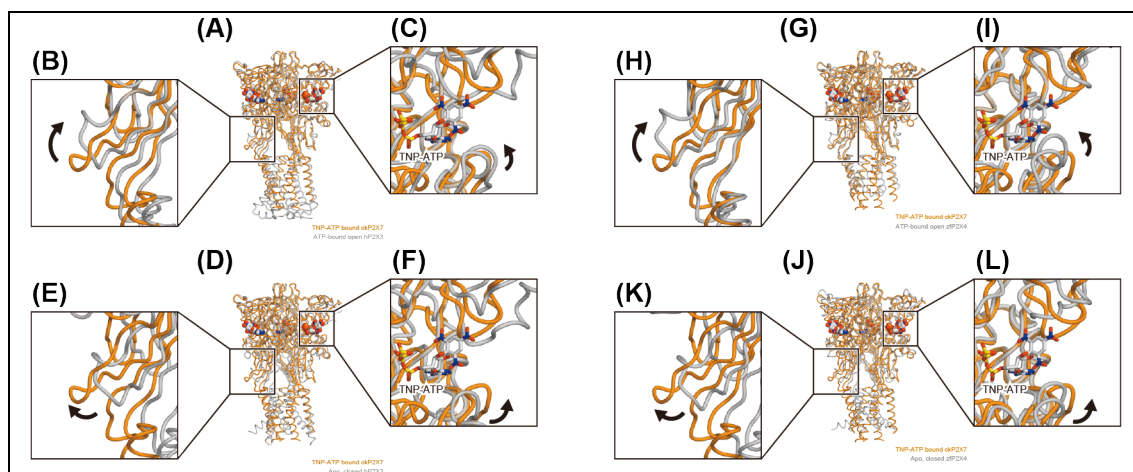


Fig. 4-10 Overall comparison of the TNP-ATP-bound state for ckP2X7 with the apo closed, and ATP-bound, open states for hP2X3 and zfp2X4.

(**A-C**) Subunit comparisons of the TNP-ATP-bound ckP2X7 (orange) and ATP-bound, open hP2X3 (gray, PDB ID: 5SVK) structures. Close-up views of the lower body domain (**B**) and the TNP-ATP binding site in the TNP-ATP-bound ckP2X7 structure (**C**) are shown in each box. The black arrows denote the movement from the TNP-ATP-bound state to the ATP-bound, open state. (**D-F**) Subunit comparisons of the TNP-ATP-bound ckP2X7 (orange) and apo, closed hP2X3 (gray, PDB ID: 5SVJ) structures. Close-up views of the lower body domain (**E**) and the TNP-ATP binding site in the TNP-ATP-bound ckP2X7 structure (**F**) are shown in each box. The black arrows denote the movement from the apo, closed state to the TNP-ATP-bound state. (**G-I**) Subunit comparisons of the TNP-ATP bound ckP2X7 (orange) and ATP-bound, open zfp2X4 (gray, PDB ID: 4DW1) structures. Close-up views of the lower body domain (**H**) and the TNP-ATP binding site in ckP2X7 (**I**) are shown in each box. The black arrows denote the movement from the TNP-ATP-bound state to the ATP-bound open state. (**J-L**) Subunit comparisons of the TNP-ATP-bound ckP2X7 (orange) and apo, closed zfp2X4 (gray, PDB ID: 4DW0) structures. Close-up views of the lower body domain (**K**) and

the TNP-ATP binding site in ckP2X7 (L) are shown in each box. The black arrows denote the movement from the apo, closed state to the TNP-ATP-bound state.

The structural comparisons between the apo, closed, and ATP-bound, open states of hP2X3 revealed that ATP binding induces the closure of the cleft between the head domain and the dorsal fin in the ATP binding pocket, and the following movement of the lower body domain to open the pore (**Fig. 4-10**). Since the extracellular domain architecture of the TNP-ATP-bound ckP2X7 structure is closer to that of the ATP-bound, open hP2X3 structure, rather than that of the apo, closed state (**Fig. 4-10**), there are similarities between the cleft closure of the ATP binding pocket and the expanded lower body domain in the TNP-ATP-bound ckP2X7 structure (**Fig. 4-10A-C**). However, these structural motifs, including the head, dorsal fin, and lower body domains in the TNP-ATP-bound ckP2X7 structure, adopt positions in between those in the apo, closed, and ATP-bound, open states of hP2X3 structures. Thus, the cleft closure of the ATP binding pocket and the expansion of the lower body domain are not completed in the TNP-ATP-bound ckP2X7 structure. Consistently, the ion-conducting pore is still closed in the TNP-ATP-bound ckP2X7 structure (**Fig. 4-10D-F**). This “incompletely activated” conformation of the TNP-ATP-bound ckP2X7 structure is apparently due to the insertion of the trinitrophenyl group between the head and dorsal fin domains, which prevents the complete cleft closure motion in the ATP binding pocket (**Fig. 4-10**). The structural comparisons between ckP2X7 and zfP2X4 are also consistent with those between ckP2X7 and hP2X3 (**Fig. 4-10G-L**).

4.4 Putative antagonistic mechanism highlighted by molecular dynamics simulations

To further investigate the functional role of the trinitrophenyl group upon the cleft closure motion, all-atom molecular dynamics (MD) simulations of the ckP2X7_{cryst} structure were performed³³. By removing the trinitrophenyl group of TNP-ATP and all-atoms of TNP-ATP, we created the “ATP-bound form” and “Apo form” ckP2X7 structures, respectively.

4.4.1 Material and methods

4.4.1.1 System construction of molecular dynamics simulation

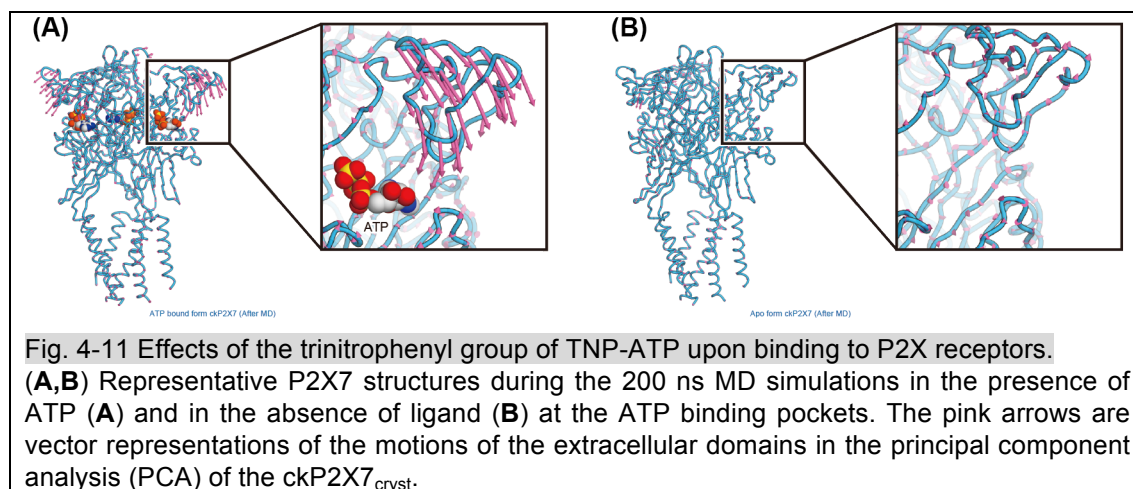
The simulation system was constructed in a similar manner of Amp2X_{cryst} simulation described in the section 3.5.1.1. The ckP2X7_{cryst} trimer, 1-palmitoyl-2-oleoyl-phosphatidylcholine (POPC), ATP, water molecules, and 150 mM NaCl were included in the system. The missing atoms, such as hydrogens in the protein, were added with the programs GROMACS 5.1.4 (ref. 106) and VMD 1.9.3 (ref. 75). The disordered side chains in the protein were modeled by COOT⁵⁴. The periodic boundary system, including the explicit solvent and the POPC lipid bilayer, was prepared. The protein was embedded into the POPC lipid bilayer using the MemProtMD pipeline¹⁰⁷. The final size of the simulation box was $119 \times 119 \times 144$ Å. The net charge of the system was neutralized by adding chloride and sodium ions. The topologies and force field parameters from CHARMM3650 were used. MD simulations were performed with the program GROMACS 5.1.447. The system was first minimized using the steepest descent with a cutoff of $100.0 \text{ kJ mol}^{-1} \text{ nm}^{-1}$, with $1000.0 \text{ kJ mol}^{-1} \text{ nm}^{-2}$ harmonic position restraints for non-hydrogen atoms of the protein and ATP. Next, we performed an equilibration for 100 ps in the NVT ensemble (310 K, $119 \times 119 \times 144$ Å volume), followed by an equilibration for 6 ns in the NPT ensemble (310 K, 1 atm), with the same restraints. Finally, we performed the production runs in the NPT ensemble for 200 ns, with the following bond length restraints between the atoms of ATP and the protein side chains: (1) ATP N1 and Thr177 OG1, (2) ATP N6 and Thr177 OG1, (3) ATP N6 and Thr64 O, and (4) ATP N7 and Thr64 OG1. These restrained bond lengths were based on those observed in the ckP2X7_{cryst} crystal structure. The simulation was repeated five times, and we obtained similar results. Constant temperature was maintained by the Nose-Hoover thermostat^{108,109}. Constant pressure was maintained by the Parrinello-Rahman barostat¹¹⁰. Long-range electrostatic interactions were calculated using the particle mesh Ewald method⁷⁹. The LINCS algorithm was used for bond constraint¹¹¹. Principle

component analysis was conducted by in-house scripts using Python 2.7.9 and MDAnalysis 0.15.0 (ref. 112).

4.4.2 Results

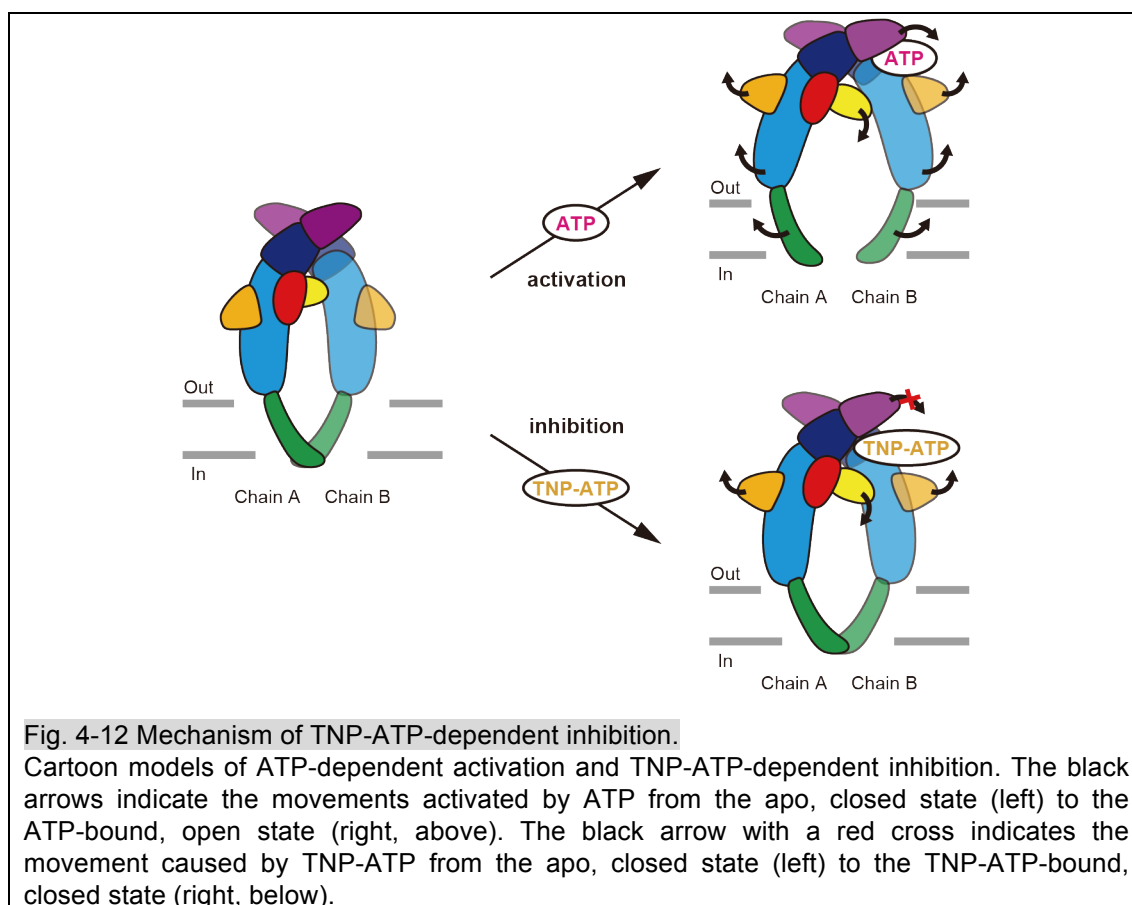
4.4.2.1 Putative antagonistic mechanism

The two model structures representing “ATP-bound form” and “Apo form” of ckP2X7 were embedded into the lipid bilayer. After performing 200 ns MD simulations, in the ATP-bound form ckP2X7 structure, the head domain underwent a significant downward movement toward the ATP binding pocket, while the other domains, including the dorsal fin domain involved in the adenine ring and ribose ring recognitions through hydrophobic interactions upon ATP binding, did not undergo any movements (Figs. 4-10A-C and 4-11A). In contrast, in the apo form ckP2X7 structure, no specific structural rearrangement was observed (Fig. 4-11B).



These results indicate that the trinitrophenyl group prevents the proper cleft closure motion for channel opening, especially by inhibiting the proper downward movement of the head domain. Consistently, the previous electrophysiological analyses showed that ATP binding and the following downward movement of the head domain toward the ATP binding pocket are crucial for the channel activation^{29,105}. Taken together, we propose that TNP-ATP binding may induce structural changes that are similar to those associated with ATP binding, and that the trinitrophenyl group of TNP-ATP

may act as a wedge to inhibit the channel activation, by preventing the downward movement of the head domain upon the cleft closure motion of the ATP binding pocket (**Fig. 4-12**).



4.5 Discussion in this chapter

In this chapter, the crystal structure of the chicken P2X7 was determined in the presence of TNP-ATP, providing clarification of the TNP-ATP recognition by the P2X7 receptor, as well as precise structural interpretations of P2X7 mutations and SNPs (**Figs. 4-4, 4-7 and 4-8**). The comparison with the previously determined P2X structures revealed that the ckP2X7 structure represents the “incompletely activated” conformation (**Fig. 4-10**). The recently determined pdP2X7 structures showed that P2X7 receptors have the subtype-specific inter-subunit cavity formed by the upper body domains between two neighboring subunits, and that ATP binding to P2X7 receptors induces the closure of this inter-subunit cavity and the following downward movement of the head

domain toward the ATP binding pocket³⁵. In the ckP2X7 structure, this cavity is partially closed, as compared to that in the pdP2X7 structures (**Fig. 4-5F-H**). These results also strengthen the proposal that the ckP2X7 structure represents the “incompletely activated” conformation. Intriguingly, the TNP-ATP-bound ckP2X7 structure exhibits a completely distinct overall conformation and TNP-ATP recognition mode from those of the recently reported TNP-ATP-bound hP2X3 structure (**Fig. 4-8**)³⁴. In the structure of ckP2X7 co-crystallized with TNP-ATP, the extracellular domain architecture is similar to that in the ATP-bound, open state structures of P2X receptors^{28,34}, and the trinitrophenyl group of TNP-ATP faces toward the head and dorsal fin domains (**Figs. 4-8A-D and 4-9**). These structural features are quite consistent with the previous electrophysiological analyses of the P2X1 and P2X4 receptors, in which the head domain is involved in the TNP-ATP recognition^{56,105}, and the NMR analysis of the P2X4 receptor, in which TNP-ATP binding induces the expansion of the extracellular domain, in a similar manner to that observed with ATP- dependent activation⁴³. In contrast, in the structure of hP2X3 soaked with TNP-ATP, the overall conformation is essentially identical to the apo, closed state of hP2X3 (**Fig. 4-8E-H**)³⁴, and the trinitrophenyl group of TNP-ATP rotates by ~180° and faces toward the lower body and left flipper domains (**Figs. 4-8E-H and 4-9**). Intriguingly, although the left flipper domain in hP2X3 faces toward the trinitrophenyl group of TNP-ATP and is close enough to interact with it, this domain is mostly disordered in the TNP-ATP-bound structure of hP2X3. Overall, these striking structural differences between the P2X7 and P2X3 receptors might arise from the differences in the subtypes or potentially from the ligand soaking employed for the determination of the TNP-ATP-bound hP2X3 structure, whereas a co-crystallization method was employed for the structure determination of the TNP-ATP-bound ckP2X7. Further functional and structural investigations will be required to fully understand these structural differences.

In summary, the TNP-ATP-bound ckP2X7 structure not only provides insights into the antagonistic mechanism of the P2X7 receptor by the competitive antagonist (**Fig. 4-12**), but also will facilitate

structure-based drug design targeting this important ion channel family associated with various immune system diseases.

References

1. CAMPBELL, G. The inhibitory nerve fibres in the vagal supply to the guinea-pig stomach. *J. Physiol.* **185**, 600–612 (1966).
2. BURNSTOCK, G., CAMPBELL, G., SATCHELL, D. & SMYTHE, A. Evidence that adenosine triphosphate or a related nucleotide is the transmitter substance released by non-adrenergic inhibitory nerves in the gut. *Br. J. Pharmacol.* **40**, 668–688 (1970).
3. Burnstock, G. Purinergic nerves. *Pharmacol. Rev.* **3**, 509–581 (1972).
4. Burnstock, G. Purinergic signalling: Its unpopular beginning, its acceptance and its exciting future. *Bioessays* **34**, 218–25 (2012).
5. Ralevic, V. & Burnstock, G. Receptors for purines and pyrimidines. *Pharmacol. Rev.* **50**, 413–492 (1998).
6. Brake, A., Wagenbach, M. & Julius, D. New structural motif for ligand-gated ion channels defined by an ionotropic ATP receptor. *Nature* **371**, 519–523 (1994).
7. Valera, S. *et al.* A new class of ligand-gated ion channel defined by P2x receptor for extracellular ATP. *Nature* **371**, 516–519 (1994).
8. Chen, C., Akopian, A. & Sivilotti, L. A P2X purinoceptor expressed by a subset of sensory neurons. *Nature* **377**, 428–31 (1995).
9. Webb, T. E. *et al.* Cloning and functional expression of a brain G-protein-coupled ATP receptor. *FEBS Lett.* **324**, 219–25 (1993).
10. Jarvis, M. F. & Khakh, B. S. ATP-gated P2X cation-channels. *Neuropharmacology* **56**, 208–15 (2009).
11. Miller, P. S. & Smart, T. G. Binding, activation and modulation of Cys-loop receptors. *Trends Pharmacol. Sci.* **31**, 161–174 (2010).
12. Traynelis, S. F. *et al.* Glutamate Receptor Ion Channels: Structure, Regulation, and Function Stephen. *Pharmacol. Rev.* **62**, 405–496 (2010).

13. North, R. A. & Jarvis, M. F. P2X receptors as drug targets. *Mol. Pharmacol.* **83**, 759–69 (2013).
14. Khakh, B. S. & North, R. A. Neuromodulation by extracellular ATP and P2X receptors in the CNS. *Neuron* **76**, 51–69 (2012).
15. Surprenant, A. & North, R. A. Signaling at purinergic P2X receptors. *Annu. Rev. Physiol.* **71**, 333–59 (2009).
16. Agboh, K. C., Webb, T. E., Evans, R. J. & Ennion, S. J. Functional characterization of a P2X receptor from *Schistosoma mansoni*. *J. Biol. Chem.* **279**, 41650–41657 (2004).
17. Bavan, S., Straub, V. a, Blaxter, M. L. & Ennion, S. J. A P2X receptor from the tardigrade species *Hypsibius dujardini* with fast kinetics and sensitivity to zinc and copper. *BMC Evol. Biol.* **9**, 17 (2009).
18. Fountain, S. J. Primitive ATP-activated P2X receptors: discovery, function and pharmacology. *Front. Cell. Neurosci.* **7**, 247 (2013).
19. North, R. A. Molecular physiology of P2X receptors. *Physiol. Rev.* **82**, 1013–67 (2002).
20. Burnstock, G. Pathophysiology and therapeutic potential of purinergic signaling. *Pharmacol. Rev.* **58**, 58–86 (2006).
21. Gever, J. R., Cockayne, D. a, Dillon, M. P., Burnstock, G. & Ford, A. P. D. W. Pharmacology of P2X channels. *Pflugers Arch.* **452**, 513–37 (2006).
22. Burnstock, G. & Ralevic, V. Purinergic signaling and blood vessels in health and disease. *Pharmacol. Rev.* **66**, 102–92 (2014).
23. Bartlett, R., Stokes, L. & Sluyter, R. The P2X7 Receptor Channel: Recent Developments and the Use of P2X7 Antagonists in Models of Disease. *Pharmacol. Rev.* **66**, 638–675 (2014).
24. Backmark, a E. *et al.* Fluorescent probe for high-throughput screening of membrane protein expression. *Protein Sci.* **22**, 1124–32 (2013).
25. Hattori, M., Hibbs, R. E. & Gouaux, E. A fluorescence-detection size-exclusion chromatography-based thermostability assay for membrane protein precrystallization screening.

- Structure* **20**, 1293–1299 (2012).
26. Pardon, E. *et al.* A general protocol for the generation of Nanobodies for structural biology. *Nat. Protoc.* **9**, 674–693 (2014).
 27. Kawate, T., Michel, J. C., Birdsong, W. T. & Gouaux, E. Crystal structure of the ATP-gated P2X(4) ion channel in the closed state. *Nature* **460**, 592–598 (2009).
 28. Hattori, M. & Gouaux, E. Molecular mechanism of ATP binding and ion channel activation in P2X receptors. *Nature* **485**, 207–12 (2012).
 29. Roberts, J. a. *et al.* Agonist binding evokes extensive conformational changes in the extracellular domain of the ATP-gated human P2X1 receptor ion channel. *Proc. Natl. Acad. Sci.* **109**, 4663–67 (2012).
 30. Jiang, R., Taly, A. & Grutter, T. Moving through the gate in ATP-activated P2X receptors. *Trends Biochem. Sci.* **38**, 20–9 (2013).
 31. Heymann, G. *et al.* Inter- and intrasubunit interactions between transmembrane helices in the open state of P2X receptor channels. *Proc. Natl. Acad. Sci. U. S. A.* **110**, E4045–54 (2013).
 32. Samways, D. S. K., Li, Z. & Egan, T. M. Principles and properties of ion flow in P2X receptors. *Front. Cell. Neurosci.* **8**, 6 (2014).
 33. Zhao, W.-S. *et al.* Relative motions between left flipper and dorsal fin domains favour P2X4 receptor activation. *Nat. Commun.* **5**, 4189 (2014).
 34. Mansoor, S. E. *et al.* X-ray structures define human P2X3 receptor gating cycle and antagonist action. *Nature* **538**, 66–71 (2016).
 35. Karasawa, A. & Kawate, T. Structural basis for subtype-specific inhibition of the P2X7 receptor. *Elife* 1–17 (2016). doi:10.7554/eLife.22153
 36. Haines, W. R., Torres, G. E., Voigt, M. M. & Egan, T. M. Properties of the novel ATP-gated ionotropic receptor composed of the P2X(1) and P2X(5) isoforms. *Mol. Pharmacol.* **56**, 720–7 (1999).

37. King, B. & Wildman, S. Effects of extracellular pH on agonism and antagonism at a recombinant P2X₂ receptor. *Br. J. Pharmacol.* **121**, 1445–1453 (1997).
38. Garcia-Guzman, M., Stühmer, W. & Soto, F. Molecular characterization and pharmacological properties of the human P2X₃ purinoceptor. *Mol. Brain Res.* **47**, 59–66 (1997).
39. Soto, F. *et al.* P2X₄: an ATP-activated ionotropic receptor cloned from rat brain. *Proc. Natl. Acad. Sci. U. S. A.* **93**, 3684–8 (1996).
40. Nakazawa, K. & Ohno, Y. Effects of neuroamines and divalent cations on cloned and mutated ATP-gated channels. *Eur. J. Pharmacol.* **325**, 101–108 (1997).
41. Li, M., Silberberg, S. D. & Swartz, K. J. Subtype-specific control of P2X receptor channel signaling by ATP and Mg²⁺. *Proc. Natl. Acad. Sci. U. S. A.* 3455–3463 (2013).
doi:10.1073/pnas.1308088110
42. Garcia-Guzman, M., Soto, F., Gomez-Hernandez, J. M., Lund, P. E. & Stühmer, W. Characterization of recombinant human P2X₄ receptor reveals pharmacological differences to the rat homologue. *Mol. Pharmacol.* **51**, 109–18 (1997).
43. Minato, Y. *et al.* Conductance of P2X₄ purinergic receptor is determined by conformational equilibrium in the transmembrane region. *Proc. Natl. Acad. Sci.* **113**, 4741–4746 (2016).
44. Williams, M. & Jarvis, M. F. Purinergic and pyrimidinergic receptors as potential drug targets. *Biochem. Pharmacol.* **59**, 1173–85 (2000).
45. Liman, E., Tytgat, J. & Hess, P. Subunit stoichiometry of a mammalian K⁺ channel determined by construction of multimeric cDNAs. *Neuron* **9**, 861–871 (1992).
46. Fujiwara, Y., Keceli, B., Nakajo, K. & Kubo, Y. Voltage- and [ATP]-dependent gating of the P2X₂ ATP receptor channel. *J. Gen. Physiol.* **133**, 93–109 (2009).
47. Hopf, T. a. *et al.* Amino acid coevolution reveals three-dimensional structure and functional domains of insect odorant receptors. *Nat. Commun.* **6**, 6077 (2015).
48. Browne, L. E. & North, R. A. P2X receptor intermediate activation states have altered nucleotide

- selectivity. *J. Neurosci.* **33**, 14801–8 (2013).
49. Lewis, C. J. & Evans, R. J. Lack of run-down of smooth muscle P2X receptor currents recorded with the amphotericin permeabilized patch technique, physiological and pharmacological characterization of the properties of mesenteric artery P2X receptor ion channels. *Br. J. Pharmacol.* **131**, 1659–66 (2000).
 50. Ohta, T., Kubota, A., Murakami, M., Otsuguro, K. & Ito, S. P2X₂ receptors are essential for [Ca²⁺]_i increases in response to ATP in cultured rat myenteric neurons. *Am. J. Physiol. Gastrointest. Liver Physiol.* **289**, G935–48 (2005).
 51. Roberts, J. a & Evans, R. J. ATP binding at human P2X₁ receptors. Contribution of aromatic and basic amino acids revealed using mutagenesis and partial agonists. *J. Biol. Chem.* **279**, 9043–55 (2004).
 52. McCoy, A. J. *et al.* Phaser crystallographic software. *J. Appl. Crystallogr.* **40**, 658–674 (2007).
 53. Adams, P. D. *et al.* PHENIX: a comprehensive Python-based system for macromolecular structure solution. *Acta Crystallogr. D. Biol. Crystallogr.* **66**, 213–21 (2010).
 54. Emsley, P., Lohkamp, B., Scott, W. G. & Cowtan, K. Features and development of Coot. *Acta Crystallogr. D. Biol. Crystallogr.* **66**, 486–501 (2010).
 55. Xiong, K., Stewart, R. R., Weight, F. F. & Li, C. Role of extracellular histidines in antagonist sensitivity of the rat P2X₄ receptor. *Neurosci. Lett.* **367**, 197–200 (2004).
 56. Zhang, L. *et al.* Involvement of Ectodomain Leu 214 in ATP Binding and Channel Desensitization of the P2X₄ Receptor. *Biochemistry* **53**, 3012–3019 (2014).
 57. Tvrdonova, V., Rokic, M. B., Stojilkovic, S. S. & Zemkova, H. Identification of Functionally Important Residues of the Rat P2X₄ Receptor by Alanine Scanning Mutagenesis of the Dorsal Fin and Left Flipper Domains. *PLoS One* **9**, e112902 (2014).
 58. Furutani, Y., Murata, T. & Kandori, H. Sodium or lithium ion-binding-induced structural changes in the K-ring of V-ATPase from enterococcus hirae revealed by ATR-FTIR spectroscopy. *J. Am.*

- Chem. Soc.* **133**, 2860–2863 (2011).
59. Yuji, F., Hirofumi, S., Yusuke, A., Shigetoshi, O. & Hideki, K. Specific interactions between alkali metal cations and the KcsA channel studied using ATR-FTIR spectroscopy. *Biophys. Physicobiology* **12**, (2015).
 60. Xia, F., Rudack, T., Kötting, C., Schlitter, J. & Gerwert, K. The specific vibrational modes of GTP in solution and bound to Ras: a detailed theoretical analysis by QM/MM simulations. *Phys. Chem. Chem. Phys.* **13**, 21451 (2011).
 61. Kawate, T. & Gouaux, E. Fluorescence-Detection Size-Exclusion Chromatography for Precrystallization Screening of Integral Membrane Proteins. *Structure* **14**, 673–681 (2006).
 62. Goehring, A. *et al.* Screening and large-scale expression of membrane proteins in mammalian cells for structural studies. *Nat. Protoc.* **9**, 2574–2585 (2014).
 63. Bo, X., Schoepfer, R. & Burnstock, G. Molecular cloning and characterization of a novel ATP P2X receptor subtype from embryonic chick skeletal muscle. *J. Biol. Chem.* **275**, 14401–7 (2000).
 64. Jensik, P. & Cox, T. ATP-induced internalization of amphibian epithelial P2X receptors is linked to channel opening. *Pflugers Arch. Eur. J. Physiol.* **444**, 795–800 (2002).
 65. Fujiwara, Y. & Kubo, Y. Regulation of the desensitization and ion selectivity of ATP-gated P2X₂ channels by phosphoinositides. *J. Physiol.* **576**, 135–149 (2006).
 66. Mo, G. *et al.* Subtype-Specific Regulation of P2X₃ and P2X_{2/3} Receptors by Phosphoinositides in Peripheral Nociceptors. *Mol. Pain* **5**, 1744-8069-5–47 (2009).
 67. Bernier, L. P., Ase, A. R., Boué-Grabot, É. & Séguéla, P. P2X₄ receptor channels form large noncytolytic pores in resting and activated microglia. *Glia* **60**, 728–737 (2012).
 68. Ennion, S., Hagan, S. & Evans, R. J. The role of positively charged amino acids in ATP recognition by human P2X₁ receptors. *J. Biol. Chem.* **275**, 29361–29367 (2000).
 69. Jiang, L. H., Rassendren, F., Surprenant, A. & North, R. A. Identification of amino acid residues contributing to the ATP-binding site of a purinergic P2X receptor. *J. Biol. Chem.* **275**, 34190–

- 34196 (2000).
70. Marquez-Klaka, B., Rettinger, J., Bhargava, Y., Eisele, T. & Nicke, A. Identification of an intersubunit cross-link between substituted cysteine residues located in the putative ATP binding site of the P2X1 receptor. *J. Neurosci.* **27**, 1456–66 (2007).
 71. Roberts, J. a. *et al.* Cysteine substitution mutagenesis and the effects of methanethiosulfonate reagents at P2X2 and P2X4 receptors support a core common mode of ATP action at P2X receptors. *J. Biol. Chem.* **283**, 20126–20136 (2008).
 72. Roberts, J. a & Evans, R. J. Contribution of conserved polar glutamine, asparagine and threonine residues and glycosylation to agonist action at human P2X1 receptors for ATP. *J. Neurochem.* **96**, 843–52 (2006).
 73. Roberts, J. a & Evans, R. J. Cysteine substitution mutants give structural insight and identify ATP binding and activation sites at P2X receptors. *J. Neurosci.* **27**, 4072–82 (2007).
 74. Gonzales, E. B., Kawate, T. & Gouaux, E. Pore architecture and ion sites in acid-sensing ion channels and P2X receptors. *Nature* **460**, 599–604 (2009).
 75. Humphrey, W., Dalke, A. & Schulten, K. VMD: Visual molecular dynamics. *J. Mol. Graph.* **14**, 33–38 (1996).
 76. Klauda, J. B. *et al.* Update of the CHARMM All-Atom Additive Force Field for Lipids: Validation on Six Lipid Types. *J. Phys. Chem. B* **114**, 7830–7843 (2010).
 77. Phillips, J. C. *et al.* Scalable molecular dynamics with NAMD. *J. Comput. Chem.* **26**, 1781–1802 (2005).
 78. Feller, S. E., Zhang, Y., Pastor, R. W. & Brooks, B. R. Constant pressure molecular dynamics simulation: The Langevin piston method. *J. Chem. Phys.* **103**, 4613 (1995).
 79. Darden, T., York, D. & Pedersen, L. Particle mesh Ewald: An N log(N) method for Ewald sums in large systems. *J. Chem. Phys.* **98**, 10089 (1993).
 80. Dai, J. & Zhou, H.-X. General rules for the arrangements and gating motions of pore-lining

- helices in homomeric ion channels. *Nat. Commun.* **5**, 4614 (2014).
81. Wildman, S. S., King, B. F. & Burnstock, G. Zn²⁺ modulation of ATP-responses at recombinant P2X₂ receptors and its dependence on extracellular pH. *Br. J. Pharmacol.* 1214–1220 (1998).
 82. Clyne, J. D., LaPointe, L. D. & Hume, R. I. The role of histidine residues in modulation of the rat P2X₂ purinoceptor by zinc and pH. *J. Physiol.* **539**, 347–359 (2002).
 83. Nagaya, N. An Intersubunit Zinc Binding Site in Rat P2X₂ Receptors. *J. Biol. Chem.* **280**, 25982–25993 (2005).
 84. Jiang, R. *et al.* Tightening of the ATP-binding sites induces the opening of P2X receptor channels. *EMBO J.* **31**, 2134–43 (2012).
 85. Morris, D. R. & Levenson, C. W. Ion channels and zinc: Mechanisms of neurotoxicity and neurodegeneration. *J. Toxicol.* **2012**, (2012).
 86. Lorca, R. a. *et al.* Zinc enhances long-term potentiation through P2X receptor modulation in the hippocampal CA1 region. *Eur. J. Neurosci.* **33**, 1175–1185 (2011).
 87. Bavan, S., Straub, V. A., Webb, T. E. & Ennion, S. J. Cloning and Characterization of a P2X Receptor Expressed in the Central Nervous System of *Lymnaea stagnalis*. *PLoS One* **7**, (2012).
 88. Surprenant A, Rassendren F, Kawashima E, North RA, B. G. The Cytolytic P2z Receptor for Extracellular ATP Identified as a P2X Receptor (P2X₇). *Science (80-.).* **272**, 735–738 (1996).
 89. Volonté, C., Apolloni, S., Skaper, S. D. & Burnstock, G. P2X₇ Receptors : Channels , Pores and More. *CNS Neurol. Disord. - Drug Targets* **11**, 705–721 (2012).
 90. Sperlágh, B., Vizi, E. S., Wirkner, K. & Illes, P. P2X₇ receptors in the nervous system. *Prog. Neurobiol.* **78**, 327–46 (2006).
 91. Agrawal, A. & Gartland, A. P2X₇ receptors: role in bone cell formation and function. *J. Mol. Endocrinol.* **54**, R75–R88 (2015).
 92. Sluyter, R. & Stokes, L. Significance of P2X₇ receptor variants to human health and disease. *Recent Pat. DNA Gene Seq.* **5**, 41–54 (2011).

93. Dardano, A. *et al.* 1513A>C polymorphism in the P2X7 receptor gene in patients with papillary thyroid cancer: Correlation with histological variants and clinical parameters. *J. Clin. Endocrinol. Metab.* **94**, 695–698 (2009).
94. McQuillin, A. *et al.* Case-control studies show that a non-conservative amino-acid change from a glutamine to arginine in the P2RX7 purinergic receptor protein is associated with both bipolar- and unipolar-affective disorders. *Mol. Psychiatry* **14**, 614–20 (2009).
95. Mehta, N. *et al.* Purinergic receptor P2X7: A novel target for anti-inflammatory therapy. *Bioorg. Med. Chem.* **22**, 54–88 (2014).
96. Skaper, S. D., Debetto, P. & Giusti, P. P2X7 Receptors in Neurological and Cardiovascular Disorders. *Cardiovasc. Psychiatry Neurol.* **2009**, 861324 (2009).
97. Zhao, W. S. *et al.* A highly conserved salt bridge stabilizes the kinked conformation of β 2,3-sheet essential for channel function of P2X4 receptors. *J. Biol. Chem.* **291**, 7990–8003 (2016).
98. Guarnieri, M. T., Blagg, B. S. J. & Zhao, R. A high-throughput TNP-ATP displacement assay for screening inhibitors of ATP-binding in bacterial histidine kinases. *Assay Drug Dev. Technol.* **9**, 174–183 (2011).
99. Waterman, D. G. *et al.* The DIALS framework for integration software. *Ccp4 Newsl. Protein Crystallogr.* 16–19 (2013).
100. Evans, P. R. & Murshudov, G. N. How good are my data and what is the resolution? *Acta Crystallogr. Sect. D Biol. Crystallogr.* **69**, 1204–1214 (2013).
101. Vagin, A. & Teplyakov, A. Molecular replacement with MOLREP. *Acta Crystallogr. Sect. D Biol. Crystallogr.* **66**, 22–25 (2010).
102. Murshudov, G. N. *et al.* REFMAC5 for the refinement of macromolecular crystal structures. *Acta Crystallogr. Sect. D Biol. Crystallogr.* **67**, 355–367 (2011).
103. Jindrichova, M. *et al.* Functional characterization of mutants in the transmembrane domains of the rat P2X7 receptor that regulate pore conductivity and agonist sensitivity. *J. Neurochem.* **133**,

- 815–827 (2015).
104. Roger, S. *et al.* Single nucleotide polymorphisms that were identified in affective mood disorders affect ATP-activated P2X7 receptor functions. *J. Psychiatr. Res.* **44**, 347–355 (2010).
 105. Lorinczi, E. *et al.* Involvement of the cysteine-rich head domain in activation and desensitization of the P2X1 receptor. *Proc. Natl. Acad. Sci.* **109**, 11396–11401 (2012).
 106. Abraham, M. J. *et al.* Gromacs: High performance molecular simulations through multi-level parallelism from laptops to supercomputers. *SoftwareX* **1–2**, 19–25 (2015).
 107. Stansfeld, P. J. *et al.* MemProtMD: Automated Insertion of Membrane Protein Structures into Explicit Lipid Membranes. *Structure* **23**, 1–12 (2015).
 108. Nosé, S. A unified formulation of the constant temperature molecular dynamics methods. *Jchem* **81**, 511–519 (1984).
 109. Hoover, W. G. Canonical Dynamics: Equilibrium Phase-Space Distributions. *Phys. Rev. A* **31**, 1695–1697 (1985).
 110. Parrinello, M. & Rahman, A. Polymorphic transitions in single crystals: A new molecular dynamics method. *J. Appl. Phys.* **52**, 7182–7190 (1981).
 111. Hess, B. P-LINCS: A Parallel Linear Constraint Solver for Molecular Simulation. *J. Chem. Theory Comput.* **4**, 116–122 (2007).
 112. Michaud-Agrawal, N., Denning, E. J., Woolf, T. B. & Oliver, B. MDAAnalysis: A Toolkit for the Analysis of Molecular Dynamics Simulations. *J. Comput. Chem.* **32**, 2319–2327 (2011).
 113. Dong, H., Sharma, M., Zhou, H. X. & Cross, T. A. Glycines: Role in α -helical membrane protein structures and a potential indicator of native conformation. *Biochemistry* **51**, 4779–4789 (2012).
 114. Yazawa, M. *et al.* TRIC channels are essential for Ca²⁺ handling in intracellular stores. *Nature* **448**, 78–82 (2007).
 115. Egan, T. M., Samways, D. S. K. & Li, Z. Biophysics of P2X receptors. *Pflugers Arch. Eur. J. Physiol.* **452**, 501–512 (2006).

116. Li, M., Toombes, G. E. S., Silberberg, S. D. & Swartz, K. J. Physical basis of apparent pore dilation of ATP-activated P2X receptor channels. *Nat. Neurosci.* **18**, (2015).
117. Zhao, Y., Chen, S., Yoshioka, C., Baconguis, I. & Gouaux, E. Architecture of fully occupied GluA2 AMPA receptor-TARP complex elucidated by cryo-EM. *Nature* 1–18 (2016). doi:10.1038/nature18961
118. Twomey, E. C., Yelshanskaya, M. V, Grassucci, R. A., Frank, J. & Sobolevsky, A. I. Elucidation of AMPA receptor-stargazin complexes by cryo-electron microscopy. *Science (80-.).* **353**, 83–86 (2016).
119. Chen, S. *et al.* Activation and Desensitization Mechanism of AMPA Receptor-TARP Complex by Cryo-EM. *Cell* **170**, 1234–1246.e14 (2017).
120. Lü, W., Du, J., Goehring, A. & Gouaux, E. Cryo-EM structures of the triheteromeric NMDA receptor and its allosteric modulation. **3729**, (2017).
121. Zhu, S. *et al.* Mechanism of NMDA Receptor Inhibition and Activation. *Cell* **165**, 1–11 (2016).
122. Meyerson, J. R. *et al.* Structural basis of kainate subtype glutamate receptor desensitization. *Nature* 1–16 (2016). doi:10.1038/nature19352
123. Du, J., Wu, S., Cheng, Y. & Gouaux, E. Glycine receptor mechanism elucidated by electron cryo-microscopy. *Nature* (2015). doi:10.1038/nature14853
124. Bai, X., McMullan, G. & Scheres, S. H. . How cryo-EM is revolutionizing structural biology. *Trends Biochem. Sci.* **40**, 49–57 (2014).
125. Wang, H.-W., Lei, J. & Shi, Y. Biological cryo-electron microscopy in China. *Protein Sci.* **0**, 1–16 (2016).
126. Danev, R., Tegunov, D. & Baumeister, W. Using the volta phase plate with defocus for cryo-em single particle analysis. *Elife* **6**, 1–9 (2017).
127. Voss, F. K. *et al.* Identification of LRRC8 Heteromers as an Essential Component of the Volume-Regulated Anion Channel VRAC. *Science (80-.).* **344**, 634–638 (2014).

128. Qiu, Z. *et al.* SWELL1, a plasma membrane protein, is an essential component of volume-regulated anion channel. *Cell* **157**, 447–458 (2014).
129. Syeda, R. *et al.* LRRC8 Proteins Form Volume-Regulated Anion Channels that Sense Ionic Strength. *Cell* **164**, 499–511 (2016).
130. Jentsch, T. J., Lutter, D., Planells-Cases, R., Ullrich, F. & Voss, F. K. VRAC: molecular identification as LRRC8 heteromers with differential functions. *Pflügers Arch. Eur. J. Physiol.* **468**, 385–393 (2016).

Original papers related to this thesis

1. **Kasuya, G.**, Fujiwara, Y., Takemoto, M., Dohmae, N., Nakada-Nakura, Y., Ishitani, R., Hattori, M., Nureki, O. Structural Insights into Divalent Cation Modulations of ATP-Gated P2X Receptor Channels. *Cell Rep.* **14**, 932–944 (2016).
2. Minato, Y., Suzuki, S., Hara, T., Kofuku, Y., **Kasuya, G.**, Fujiwara, Y., Igarashi, S., Suzuki, E., Nureki, O., Hattori, M., Ueda, T., Shimada, I. et al. Conductance of P2X4 purinergic receptor is determined by conformational equilibrium in the transmembrane region. *Proc. Natl. Acad. Sci.* **113**, 4741–4746 (2016).
3. **Kasuya, G.**, Fujiwara, Y., Tsukamoto, H., Morinaga, S., Ryu, S., Touhara, K., Ishitani, R., Furutani, Y., Hattori, M., Nureki, O. Structural insights into the nucleotide base specificity of P2X receptors. *Sci. Rep.* **7**, 45208 (2017).
4. **Kasuya, G.**, Yamaura, T., Ma, X.-B., Nakamura, R., Takemoto, M., Nagumo, H., Tanaka, E., Dohmae, N., Nakane, T., Yu, Y., Ishitani, R., Matsuzaki, O., Hattori, M., Nureki, O. Structural insights into the competitive inhibition of the ATP-gated P2X receptor channel. *Nat. Commun.* **8**, 876 (2017).

Supplemental papers related to this thesis

1. Nishizawa, T., Kita, S., Maturana, A.D., Furuya, N., Hirata, K., **Kasuya, G.**, Ogasawara, S., Dohmae, N., Iwamoto, T., Ishitani, R., Nureki, O. Structural basis for the counter-transport mechanism of a H^+/Ca^{2+} exchanger. *Science* **341**, 168–72 (2013).
2. **Kasuya, G.**, Hiraizumi, M., Maturana, A.D., Kumazaki, K., Fujiwara, Y., Liu, K., Nakada-Nakura, Y., Iwata, S., Tsukada, K., Komori, T., Uemura, S., Goto, Y., Nakane, T., Takemoto, M., Kato, H.E., Yamashita, K., Wada, M., Ito, K., Ishitani, R., Hattori, M., Nureki, O. Crystal structures of the TRIC trimeric intracellular cation channel orthologues. *Cell Res.* **26**, 1288–1301 (2016).

Acknowledgement

This work is supported mainly by my supervisor, Professor Osamu Nureki, and following Associated Professor Ryuichiro Ishitani and Professor Motoyuki Hattori (Fudan University, China). They always gave me a precise supervision and warmful encouragement. Particularly, I would like to emphasize the contribution of Professor Motoyuki Hattori to my works. If I did not meet him when he had come back to Nureki lab in 2012, I would not complete my PhD course and produce works like this. After moving to Shanghai as a professor, he kindly continued his supervision. I would also thank the other Nureki lab members for critical advice and support on both experimental and daily issues, especially for Dr. Takanori Nakane (MRC Laboratory of Molecular Biology, United Kingdom), Dr. Tomohiro Nishizawa and Ms. Rieko Yakazaki.

I would also thank to the beamline staff members at BL41XU of SPring-8 (Hyogo, Japan), and X06SA of Swiss Light Source (Villigen, Switzerland) for the assistance of The X-ray scattering experiment and data collection. This thesis was completed in collaboration with many scientists. Notably, I would like to express appreciation to the following persons.

1. For teaching techniques and performing TEVC recordings using *Xenopus laevis* oocytes

Associated Prof. Yuichiro Fujiwara (Osaka University).

2. For providing *Xenopus laevis* oocytes

Prof. Kazushige Touhara, Mr. Satoshi Morinaga, and Mr. Satoshi Ryu (University of Tokyo).

3. For the collaboration and providing important results through P2X project

Prof. Ichio Shimada, Assistant prof. Takumi Ueda, Mr. Tomoaki Hara (University of Tokyo), Dr. Yuichi Minato (Kyowa Hakko Kirin Co.), and Ms. Shiho Suzuki (Chugai pharmaceutical Co.).

4. For performing Patch-clamp recordings using HEK cells

Prof. Ye Yu, and Mr. Xiao-Bo Ma (Shanghai Jiao Tong University, China)

Finally, I would like to thank my family for continuous support, and all species living in the earth.

Go Kasuya